



The Ni-YSZ interface

Structure, composition and electrochemical properties at 1000°C

Hansen, Karin Vels; Chorkendorff, Ib; Mogensen, Mogens Bjerg; Bilde-Sørensen, Jørgen

Publication date:
2002

Document Version
Publisher's PDF, also known as Version of record

[Link back to DTU Orbit](#)

Citation (APA):

Jensen, K. V., Chorkendorff, I., Mogensen, M. B., & Bilde-Sørensen, J. (2002). The Ni-YSZ interface: Structure, composition and electrochemical properties at 1000°C. Roskilde: Forskningscenter Risø. (Denmark. Forskningscenter Risøe. Risøe-R; No. 1335(EN)).

DTU Library

Technical Information Center of Denmark

General rights

Copyright and moral rights for the publications made accessible in the public portal are retained by the authors and/or other copyright owners and it is a condition of accessing publications that users recognise and abide by the legal requirements associated with these rights.

- Users may download and print one copy of any publication from the public portal for the purpose of private study or research.
- You may not further distribute the material or use it for any profit-making activity or commercial gain
- You may freely distribute the URL identifying the publication in the public portal

If you believe that this document breaches copyright please contact us providing details, and we will remove access to the work immediately and investigate your claim.

The Ni-YSZ interface

Structure, composition and
electrochemical properties at 1000°C

Karin Vels Jensen

Risø National Laboratory, Roskilde, Denmark
June 2002

Risø-R-1335(EN)

ISBN 87-550-3042-4, ISBN 87-550-3043-2(Internet)

ISSN 0106-2840

Abstract

The anode/electrolyte interface in solid oxide fuel cells (SOFC) is known to cause electrical losses. Geometrically simple Ni/yttria-stabilised zirconia (YSZ) interfaces were examined to gain information on the structural and chemical changes occurring during experiments at 1000°C in an atmosphere of 97% H₂/3% H₂O. Electrochemical impedance spectroscopy at open circuit voltage (OCV) and at anodic and cathodic polarisations (100 mV) was performed. A correlation of the electrical data with the structure development and the chemical composition was attempted. Nickel wires with different impurity content (99.8% Ni and 99.995% Ni) were used to examine the impact of impurities on the polarisation resistance and contact area morphology. The electropolished nickel wires were pressed against a polished 8 mol% YSZ surface.

Extensive structural changes from a flat interface to a hill and valley structure were found to occur in the contact area with the impure nickel wire, and a ridge of impurities was built along the rim of the contact area. Impurity particles in the interfacial region were also observed. The impurity phase was described as an alkali silicate glassy phase. No differences were found between polarised and non-polarised samples. With pure nickel wires, however, the microstructures depended on the polarisation/non-polarisation conditions. At non-polarised conditions a hill and valley type structure was found. Anodic polarisation produced an up to 1 µm thick interface layer consisting of nano-sized YSZ particles with some Ni present. At cathodic polarisation both a granulated structure and a hill and valley structure resembling the structure of non-polarised samples were found. Small impurity ridges were surrounding the contact areas on non-polarised and cathodically polarised samples. TOF-SIMS and XPS analyses showed the presence of impurities in both the impure and pure contact areas.

The impedance spectroscopy revealed that depending on the impurity content of the nickel, different developments of the polarisation resistance with time took place. At open circuit voltage the samples with impure nickel electrodes showed an initial increase toward a high constant polarisation resistance, whereas the samples with pure nickel electrodes showed a considerable decrease to a low constant polarisation resistance with time. For both types of nickel the polarisation resistance dropped upon polarisation. The area specific polarisation resistances for the samples with pure electrodes were approximately 10 times lower than for samples with impure electrodes. This was mainly ascribed to the impurity content and distribution, both in the three phase boundary zone and as a more or less continuous film covering the interfacial region. The drop in the R_p upon polarisation may be ascribed to changes in the distribution of the impurity phase in the interfacial region.

Dansk resumé

Det er et kendt fænomen, at elektrode/elektrolyt-grænsefladerne i fastoxid-brændselsceller forårsager elektriske tab. For at undersøge strukturelle og kemiske ændringer i Ni/yttria-stabiliseret zirkonia (YSZ) grænsefladen efter forsøg ved 1000°C i en atmosfære af 97% H_2 /3% H_2O , blev geometrisk forsimplede grænseflader fremstillet. Elektrokemisk impedansspektroskopi blev udført både ved OCV og under anodisk og katodisk polarisation (100 mV). De elektriske data blev forsøgt korreleret med de udviklede strukturer og kemiske ændringer, der blev observeret i grænsefladen. Der blev brugt nikkeltråd af to forskellige renhedsgrader (99.8% Ni og 99.995% Ni) for at undersøge urenhedernes indflydelse på polarisationsmodstand og strukturudvikling. De elektropolerede nikkeltråde blev presset mod en poleret 8 mol% YSZ overflade.

Omfattende ændringer i morfologien af zirkonia-overfladen i form af en såkaldt hill and valley struktur blev sammen med en kant af urenheder (rim ridge) langs kontaktområdegrænsen fundet på prøver med urene nikkelelektroder. Partikler af en urenhedsfase blev også fundet i grænsefladen. Urenhedsfasen kunne karakteriseres som en alkali-silikat glas-fase. Der observeredes ingen forskel mellem polariserede og ikke-polariserede prøver med urene nikkelelektroder. Det gjorde der derimod på prøver med rene nikkelelektroder. Ikke-polariserede prøver viste en form for hill and valley struktur. Ved anodisk polarisation dannedes et op til 1 μ m tykt grænsefladelag bestående af nano-størrelse partikler af YSZ. Nikkel blev detekteret i dette lag. Katodisk polariserede prøver udviste to typer af strukturer. Dels en struktur med en granuleret overflade og dels en hill and valley type struktur. Små urenhedskanter langs trefasegrænsen blev fundet både på ikke-polariserede og katodisk polariserede prøver. TOF-SIMS og XPS analyser bekræftede tilstedeværelsen af urenheder i kontaktområdet.

Impedansspektroskopi viste, at polarisationsmodstanden udviklede sig forskelligt med tiden afhængigt af, om nikkeltråden havde et stort eller lille indhold af urenheder. For prøver med uren nikkel sås R_p at stige brat og derefter flade ud ved en høj modstand. For prøver med ren nikkel faldt R_p brat i begyndelsen og fladede derefter ud ved en lav modstand. For begge typer af nikkel faldt polarisationsmodstanden ved polarisation, men prøver med rene nikkelelektroder nåede arealspecifikke modstande, der var 10 gange mindre end for prøver med urene nikkelelektroder. Forskellen tilskrives indholdet af urenheder og disses fordeling både i trefasegrænse-zonen og som en mere eller mindre kontinuert film i grænsefladen. Faldet i R_p ved polarisation kan formentlig forklares ved en dertil relateret ændring i fordelingen af urenhederne i grænsefladen.

Contents

1	Introduction.....	1
1.1	SOFC principle of operation.....	1
1.2	SOFC Materials.....	2
1.2.1	Anode.....	2
1.2.2	Electrolyte.....	2
1.2.3	Cathode.....	3
1.2.4	Interconnect.....	3
1.3	Anode-electrolyte interface.....	3
1.3.1	Three phase boundary.....	3
1.4	Electrical losses/electrochemical efficiency.....	3
1.5	Previous studies on Ni point electrodes.....	4
1.6	Objective of the thesis.....	5
1.7	Thesis layout.....	5
2	Experimental.....	6
2.1	Sample preparation.....	6
2.1.1	YSZ three-electrode pellets.....	6
2.1.2	Nickel wires.....	6
2.2	Experimental set-up for electrochemical testing.....	7
2.2.1	Geometry of the set-up.....	7
2.2.2	Electrochemical measurements.....	8
2.2.3	Samples for electrochemical measurements.....	10
2.3	Other experiments/analyses.....	10
2.4	Methods of analysis.....	11
2.4.1	SEM/EDS.....	11
2.4.2	XPS.....	12
2.4.3	AFM.....	12
2.4.4	TOF-SIMS.....	12
3	Morphology of contact areas.....	13
3.1	Samples with impure nickel wires as electrodes.....	13
3.1.1	Contact areas on the YSZ pellets.....	14
3.1.2	Description of structure types.....	15
3.1.3	The rim ridge.....	18
3.1.4	Other features concerning the YSZ contact area.....	19
3.1.5	The nickel wires.....	21
3.2	Pure nickel wires as electrodes.....	22
3.2.1	Contact areas on the YSZ pellet.....	22
3.2.2	Descriptions of structures.....	23
3.3	Thermally annealed sample.....	29
3.4	Discussion on morphology.....	32
3.4.1	Thermal annealing of YSZ.....	32
3.4.2	Impurity influence on the formation of hill and valley structures.....	32
3.4.3	The rim ridge.....	33
3.4.4	Bonding between Ni and YSZ.....	34
3.4.5	Influence of current.....	34
3.5	Conclusion on morphology.....	35
4	Impurities.....	36
4.1	Impurities in YSZ.....	36
4.2	Results of XPS analysis of YSZ.....	36
4.3	Impure nickel electrodes.....	38

4.3.1	Contact areas on YSZ pellets.....	39
4.4	Pure nickel electrodes.....	41
4.4.1	Contact areas on YSZ pellets.....	42
4.5	TOF-SIMS and XPS analyses.....	43
4.5.1	Overview scans.....	43
4.5.2	The contact area interior.....	44
4.5.3	The contact area border.....	47
4.5.4	XPS analyses.....	48
4.6	Discussion on impurities.....	50
4.6.1	Impurity segregation in YSZ.....	50
4.6.2	Impurity segregation from the Ni to the interface.....	50
4.6.3	Summary on the origin of impurities.....	52
4.6.4	Rim ridge formation.....	52
4.7	Conclusion on impurities.....	55
5	Impedance Spectroscopy.....	56
5.1	Series resistance.....	56
5.1.1	Impure nickel wires as electrodes.....	57
5.1.2	Pure nickel wires as electrodes.....	58
5.1.3	Electrical contact areas.....	59
5.2	Polarisation resistance.....	61
5.2.1	Impure nickel wires as electrodes.....	61
5.2.2	Pure nickel wires as electrodes.....	64
5.3	Impedance spectra.....	65
5.3.1	Spectra from samples with impure electrodes.....	65
5.3.2	Spectra from samples with pure electrodes.....	66
5.4	Capacitance.....	71
5.5	Chronoamperometry.....	73
5.6	Potential sweeps.....	75
5.7	Discussion on electrical measurements.....	76
5.7.1	Series resistance.....	76
5.7.2	Polarisation resistance trends.....	76
5.7.3	Polarisation resistance values.....	77
5.7.4	Capacitance.....	78
5.8	Conclusion on electrical measurements.....	78
6	Overall summary and discussion.....	79
6.1	Impurities and structures.....	79
6.2	Impurities and resistance.....	79
6.3	Structures and polarisation.....	82
7	Final Conclusions.....	83
8	Outlook.....	84
	References.....	85
	List of publications.....	89
	Appendices.....	90
A	List of experiments.....	91
B	The user interface of EasyPlot.....	95
C	Additional impedance spectra.....	96
D	Potential sweep curves.....	100
E	Publications.....	102

Preface

This thesis is submitted to the Technical University of Denmark as a partial fulfilment of the requirements for the degree of Ph.D. The work presented in this thesis is the product of three years of work carried out mainly at the Materials Research Department, Risø National Laboratory, but with visits for four months at the University of Oslo, Norway and for five months at Lund University, Sweden. The Ph.D.-scholarship was granted by the Nordic Energy Research Program. The formal responsibility for the work was undertaken by the Department of Chemical Engineering at the Technical University of Denmark.

I would like to thank my supervisors:

- Professor Ib Chorkendorff, Department of Chemical Engineering, Technical University of Denmark, for valuable suggestions and discussions.
- Senior Scientist Mogens Mogensen, Materials Research Department, Risø National Laboratory, for the daily supervision and inspiring discussions, and last but not least for accepting a geologist with no prior knowledge on electrochemistry as a Ph.D.-student.
- Senior Scientist Jørgen Bilde-Sørensen, Materials Research Department, Risø National Laboratory, for assistance and explanations when the microscopes did not want to cooperate with me.
- Senior Scientist Carsten Bagger who is no longer in this world and is greatly missed.

I gratefully acknowledge the SOFC-group at Risø National Laboratory and the help they have provided for me in many different areas. Also, John Larsen at the Department of Physics, Technical University of Denmark and Lene Hubert at the Danish Polymer Centre, Risø National Laboratory are thanked for technical guidance with analysis equipment.

I wish to thank Professor Truls Norby and his colleagues at the Centre for Materials Science at the University of Oslo and Professor Reine Wallenberg and the staff at the Department of Materials Chemistry at Lund University for making my stays possible and fruitful.

Karin Vels Jensen
Roskilde, June 4th 2002

1 Introduction

The solid oxide fuel cell (SOFC) technology has many advantages compared to the conventional fossil fuel power generation. Burning of coal and oil contribute to air pollution by releasing large amounts of CO_2 , NO_x and SO_2 . With SOFC the pollution is minimised as the amount of nitrous gases and SO_2 is almost non-existent and as less CO_2 per kWh is released. The transition through thermal and mechanical energy to make electrical energy is practically lowered by the Carnot cycle whereas the conversion directly from chemical to electrical energy by electrochemical combustion in SOFC's results in a higher efficiency. SOFC's are silent and contain no moving parts. They can be produced from kW to MW scale. Another major advantage is that fuel cells may work as electrolyzers producing hydrogen and oxygen from e.g. excess wind energy. In the following the main reference is Minh & Takahashi [1].

1.1 SOFC principle of operation

A fuel cell consists of an anode, an electrolyte and a cathode (fig. 1.1). It is provided with separate gas flows to the anode and cathode. The cathode gas is air or oxygen whereas fuel (e.g. hydrogen or natural gas) must be supplied at the anode. At the cathode, oxygen is converted to oxide ions by acceptance of two electrons from the external circuit. The oxide ions are then conducted through the electrolyte. Upon arrival at the anode the oxide ions react with the fuel and form H_2O and CO_2 and electrons are released to the external circuit. In the case where hydrogen is used as fuel only H_2O is formed.

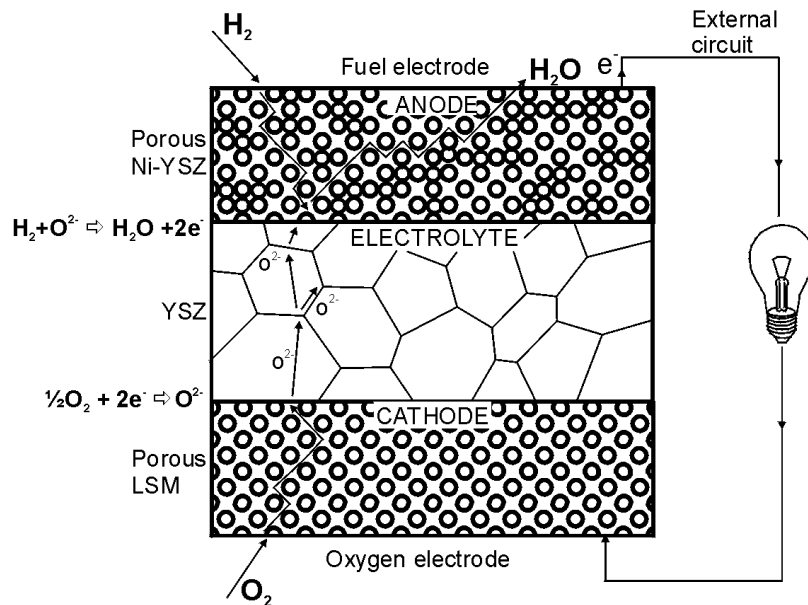


Fig. 1.1. The solid oxide fuel cell. The drawing illustrates the diffusion of reactants and products to and from the reaction sites, the oxide ion diffusion in the electrolyte and the electron path in external circuit. The signatures in the anode and cathode represent the porosity of the materials. The anode and cathode reactions are indicated.

The important electrochemical reactions taking place in a solid oxide fuel cell are the reduction of oxygen at the cathode and oxidation of fuel at the anode.

A single cell produces approximately 1 V when the cell is not loaded. By stacking the cells in series any size of power outcome can be achieved. Stacking requires the introduction of an interconnect between the anode of one cell and the cathode of the next to separate the hydrogen and oxygen and to provide a path for current collection.

1.2 SOFC Materials

The choice of materials for solid oxide fuel cells is restricted in many ways as the working conditions are very demanding. The materials all need to be compatible with each other and to be chemically and physically stable at the operation temperature. This includes that the thermal expansion coefficients are suitable, that the morphology is stable and that no deteriorating phase transformations takes place. Chemical interaction between adjoining components may lead to changes of the original properties of the materials and new phases with undesired properties. Changes in dimensions may cause cracking and delamination.

The electrolyte is subjected to both oxidising and reducing conditions and is required to be stable in both atmospheres. It must be ionic conducting, dense to prevent gas leakage, have a high strength and low electronic conductivity.

Both anode and cathode must be electronic conducting and stable in reducing and oxidising atmospheres respectively. They also need a high catalytic activity with respect to the reactions taking place: reduction of the oxidant at the cathode and oxidation of the fuel at the anode. To allow gas diffusion to the reaction sites both the anode and the cathode must be porous.

The interconnect must be electronically conducting in dual atmospheres and dense to prevent contact between oxygen and fuel gas.

All materials and production processes must, of course, be as cheap as possible.

1.2.1 Anode

The most widely used anode for solid oxide fuel cells consists of a Ni-yttria-stabilised zirconia (YSZ) cermet, which is a mixture YSZ and NiO-particles. The NiO is reduced to Ni in situ when it is exposed to hydrogen in the fuel cell. The YSZ makes up an open solid network and in between, the nickel particles provide a percolation path for electrons. Upon reduction, the porosity of the cermet increases. This structure maximises the three phase boundary between Ni, YSZ and hydrogen, thereby creating more reaction sites for the electrochemical processes.

It is important to optimise the microstructure of the cermet. Control of starting powders can determine the particle size, which is important to prevent nickel particle sintering. The right porosity is crucial to let fuel reach the electrode/electrolyte interface and to let reaction products diffuse out [2].

Primdahl [7] established that a zone of no more than 10-20 μm exists where the electrochemical reactions occur. The rest of the anode acts as a current collector. The nature of the three phase boundary depends on the microstructure of the cermet, which thereby is an important factor in optimising cermets.

1.2.2 Electrolyte

The electrolyte in SOFC's is usually made of yttria-stabilised zirconia. Zirconia can be stabilised as a cubic phase at high temperatures and has the advantage of a high ionic conductivity. By doping the ZrO_2 with Y_2O_3 , oxygen vacancies are created and they contribute to the ionic conductivity. The maximum conductivity is found at an yttria content of 8 mol%. This composition, however, is not stable at 1000°C.

1.2.3 Cathode

Strontium doped lanthanum manganite (LSM) is the present choice for a cathode material. The strontium enhances the electronic conductivity and modifies the thermal expansion. At high temperatures and over long times, formation of new phases are seen at the LSM/YSZ interface with La, Mn and Sr diffusing into the YSZ.

1.2.4 Interconnect

At the present time a metallic interconnect is preferred as compared to the earlier ceramic LaCrO_3 interconnect. Metals provide better chemical compatibility, improved mechanical properties and lower cost.

1.3 Anode-electrolyte interface

The electrode-electrolyte interface is vital for the electrochemical reactions. Chemical reactions, corrosion or interdiffusion of species from one phase to another may lead to a change in the properties of the interface. This may have consequences for the electrochemical/electrode kinetic properties [2]. A chemically and microstructurally stable interface is desirable for long-term stability.

Generally the Ni-YSZ anode is found to be stable and without chemical interaction with the electrolyte at temperatures below 1000°C . However, it has been shown that NiO is soluble in cubic YSZ in the order of 1.2-1.8 mol% between 1200 and 1600°C [3] and upon reduction, where metallic Ni nuclei are precipitated, equilibrium formation of tetragonal YSZ is promoted. This strongly and irreversibly decreases the conductivity of the YSZ [4].

1.3.1 Three phase boundary

The electrochemical charge transfer reactions are believed to take place very close to the three phase boundary (TPB) zone between nickel, YSZ and hydrogen. The number of active reaction sites is supposed to be related to the three phase boundary length. If the reactions in the three phase boundary zone are inhibited e.g. by a very thin, but non-conducting impurity layer, it could prove to be disastrous for the performance of the electrode. The exact reaction mechanisms are still not well established and involve complex mechanisms [2].

Mogensen et al. [5] and Mogensen and Skaarup [6] consider available data on anode mechanisms. Hydrogen is easily adsorbed on the nickel surface and the surface diffusion of hydrogen on nickel is fast. None of these processes are rate determining. Protons are soluble in nickel and estimations of bulk diffusion yield considerable current densities. Small current densities are expected from proton diffusion in the YSZ. Probable rate limiting processes could involve transfer of protons from Ni to YSZ and H_2O formation on YSZ [5, 6].

1.4 Electrical losses/electrochemical efficiency

The cell (open circuit) reversible voltage (E_r) is determined by thermodynamics. The maximum voltage, which can be achieved by an SOFC with given reactant gases, is the reversible voltage. The operating cell voltage (E) (eq. 1.1) is always lower than the reversible voltage due to various losses [1].

$$E = E_r - IR_i - (\eta_a + \eta_c). \quad (1.1)$$

IR_i is the ohmic loss, η_a and η_c are the anode and cathode polarisation losses. Ohmic losses are a result of the resistance of the electrolyte and other cell components. The polarisation losses are associated with the electrochemical reactions presumably taking place in the three phase boundary zone.

The total polarisation or overpotential consists of different polarisations, which contribute additively to the overall polarisation. Minh & Takahashi [1] describe four types:

- 1) Charge transfer polarisation includes the energy barrier (activation energy) that reacting species have to overcome. Slow rate-determining steps e.g. adsorption, electron transfer, desorption may cause a charge transfer polarisation. This type is more important at lower temperatures.
- 2) Diffusion/concentration polarisation is due to mass transport effects.
- 3) Reaction polarisation appears when the rate of the reaction to supply cell reactants or to remove products is slow. This polarisation is similar to the concentration polarisation. Contributions are usually low at high temperatures.
- 4) The last type is termed resistance/ohmic polarisation and involves contact resistance between cell components and resistance to electronic and ionic conduction through the respective materials.

1.5 Previous studies on Ni point electrodes

Point electrodes are relatively simple compared to cermet electrodes. Their main advantage is that effects due to the complicated microstructure of the cermet are avoided.

The Ni point electrode studies previously published are limited to a few articles. Norby et al. [8], Norby [9] and Norby & Kofstad [10] examine point electrodes of nickel wires, wound around alumina rods and pressed against a YSZ pellet. In Norby et al. [8] the contacts consisted of multiple points. The surface morphology and purity of the nickel wire were not specified. The YSZ pellet was used as-sintered. Three phase boundary (TPB) lengths between 3.3-15.7 mm were obtained. Impedance spectroscopy at OCV revealed a single arc at 900°C after two hours of stabilisation time at 1000°C. In an atmosphere of $p_{H_2}=120$ Pa and $p_{H_2O}=630$ Pa, R_{ct} was found to be approximately 20 k Ω cm and showed an inverse linear relationship with the TBP length. Norby and Norby & Kofstad [9, 10] deal with the same two point electrodes of nickel (99.9 % Ni) wires, which were pressed against an unpolished YSZ surface. They were stabilised for two days at 1100°C in 98% $H_2/2\%$ H_2O . Depending on temperature (400-900°C), up to four overlapping semi-circles were found. Variations between the two electrodes are large considering deconvolution results and activation energies. The first electrode degraded considerably during the measurements. A roughened Ni surface was observed but no new phases were found. The second electrode was used for a study of isotope effects.

Guindet et al. [11] investigated a pure Ni ball point electrode pressed against a 10 mol% YSZ pellet with a contact area of $5 \cdot 10^{-3}$ cm² and a three phase boundary length of 0.25 cm. The temperature was 960°C and different p_{H_2}/p_{H_2O} were applied. At OCV ($p_{H_2}/p_{H_2O}=7.15$) two semi-circles were identified. A polarisation resistance of 850 Ω was found, leading to a length specific resistance (LSR) of 213 Ω cm and area specific resistance (ASR) of 4.25 Ω cm². The series resistance was in the order of 150 Ω ([11], Fig 5.a.).

Mohamedi-Boulouar et al. [12] investigated a Ni ball point electrode (99.99% Ni) with respect to the influence of water vapour. The temperature range was 700-1000°. One semi-circle was found at OCV at 975°C. The series resistance was 250 Ω and the polarisation resistance was 2200 Ω at $p_{H_2}/p_{H_2O}=14$. The electrocatalytic effect of water was demonstrated.

Aaberg et al. 1998 studied the electrochemistry of Ni-YSZ single contact electrodes at 1000°C. Ni electrodes showed one depressed semi-circle. It was found that redistribution of Ni from the electrode to the electrolyte occurred at anodic overpotentials, forming a string of Ni particles around the three phase boundary. Morphological changes in the contact area were observed.

Ni point electrodes were examined by Kek et al. [13] at 600-850° in variable mixtures of H_2/N_2 with 1 % H_2O and at potential ranging from -500 mV to +500 mV. Impedance spectra at OCV showed typically one semi-circle and could be fitted with an equivalent circuit $R_s(C_1(R_1(R_2Q_2)))$.

Studies of other types of simple electrodes are found in the literature: Ni pattern or Ni stripe electrodes are ideal for controlling the three phase boundary length [14,15,16]. Porous electrodes have been studied by de Boer [17], who also examined pattern and cermet electrodes.

1.6 Objective of the thesis

Despite the abundance of experiments on different types of Ni/YSZ anodes found in the literature, no consistency is found, neither between the different types of electrodes nor between nominally identical electrodes. The reproducibility is often poor and contradictory results are seen. Furthermore, a comparison of literature data is not straightforward due to different preparation methods, operating temperatures, atmospheres etc.

It was suggested [18] that a reason for the disagreements could be the presence of impurities and/or segregation of electrode and electrolyte components.

The interfaces (e.g. anode/electrolyte) are believed to be major contributors to electrical losses, which are reducing the performance of the cells, and changes in the microstructure may change the properties of the materials and interfaces and lead to degradation of the cells.

The main purpose of the thesis is to study the interface between Ni and YSZ and to determine how the interface behaves at 1000°C with respect to the morphological changes and chemical composition, and to try to correlate this with the electrochemical behaviour of the interface. Microstructural examinations are performed by a combination of scanning electron microscopy (SEM) and atomic force microscopy (AFM), where the latter is used especially for determining topographical relations. The chemical composition is measured using three different methods. Energy dispersive X-ray spectroscopy (EDS) is used for analysing features in the micron-sized range, X-ray photoelectron spectroscopy (XPS) is used for surface and subsurface (30 monolayers) analyses and finally, time of flight secondary ion mass spectrometry (TOF-SIMS) is used for determining the elemental composition of the surface (1 monolayer). The electrochemical properties of the interface are examined by impedance spectroscopy with the attention focused on the development of the polarisation resistance with time. Two types of nickel with different impurity contents were used to examine the impact of impurities on the electrochemical behaviour on the interface. To avoid the complicated microstructure of cermets, a Ni point electrode was employed to produce the Ni-YSZ interface.

1.7 Thesis layout

Chapter 2 describes the experimental work and the different types of samples and treatments. The following three chapters (3-5) deal with the obtained results. They are divided into “Morphology of contact areas”, “Impurities” and “Impedance spectroscopy”. These chapters are further subdivided into sections describing impure and pure electrodes separately. Each chapter contains its own discussion and a conclusion. Finally an overall discussion/summary is presented and a conclusion is given, and as the last chapter, the possibilities of further work are considered.

Five appendices are added; Appendix A contains a list of all the experiments, which were carried out. Appendix B displays the user interface of EasyPlot, a program, which was developed for plotting e.g. impedance spectra. Appendix C contains additional impedance spectra and Appendix D shows potential sweep curves. Appendix E is a collection of five publications, which are based on or contain essential data from the present work.

2 Experimental

The majority of the experiments that have been carried out were meant for electrochemical testing and later microstructural and chemical analysis. They were all of the same type and similar preparation and experimental procedures were attempted. The sample preparation, experimental set-up (fig. 2.1) and conditions are described in the sections 2.1 and 2.2. The temperature and the atmosphere/water content have been kept constant. A few experiments with other purposes and set-ups are described in section 2.3. The most important methods of analysis are mentioned in section 2.4.

2.1 Sample preparation

2.1.1 YSZ three-electrode pellets

Three-electrode pellets of 8 mol% Y_2O_3 in ZrO_2 (YSZ) (TZ-8Y, Tosoh Corporation) were isostatically pressed at 4000 kg/cm^2 and sintered for 2 hours at 1600°C in air. All pellets were mechanically worked before sintering. The grain size of the YSZ pellets is around $10 \mu\text{m}$.

The YSZ three-electrode pellets (fig. 2.2 A) were polished in several steps ending with $1 \mu\text{m}$ diamond paste. SEM and AFM images showed a few scratches of less than 20 nm depth after the polishing and an otherwise smooth surface.

The chemical composition of the powders (batch 106, 150 and 309) is shown in table 2.1. Despite the name TZ-8Y the three batches actually contain 7.82, 7.77 and 7.71 mol% Y_2O_3 .

A single crystal of 10 mol% Y_2O_3 in ZrO_2 was also polished and several samples were produced. The single crystal was acquired (in an earlier collaboration) from Dr. Sergey Shkerin, Institute of High-Temperature Electrochemistry, RAS, 20 S. Kovalevskaya Str., 620219 Ekaterinburg, Russia. The composition was stated as $0.9 \text{ ZrO}_2 + 0.1 \text{ Y}_2\text{O}_3$.

Table 2.1. The chemical composition in wt% of the three TZ-8Y batches used for pellet production.

	Batch 106	Batch 150	Batch 309
Oxide	Wt%	Wt%	Wt%
Y_2O_3	13.47	13.38	13.27
Al_2O_3	<0.005	<0.005	<0.005
SiO_2	0.005	0.004	0.003
Fe_2O_3	0.003	0.006	<0.002
Na_2O	0.052	0.078	0.060

2.1.2 Nickel wires

Three different nickel wires were used:

- Impure: 99.8 % Ni, 0.38 mm in diameter (from Johnson Matthey). A typical analysis (the only available from Johnson Matthey) is shown in table 2.2.
- Pure: 99.99+% Ni, 0.25 mm in diameter (Goodfellow). The impurity content is given in table 2.2.

- Pure: 99.995% Ni, Puratronic, 0.5 mm (Johnson Matthey). The impurity content is given in table 2.2.

The raw wires were rough and electropolishing was performed to achieve a smooth surface. The electropolishing was performed in an electrolyte of 120 ml H₂O, 700 ml ethanol, 100 ml Butoxy (C₆H₁₄O₂) and 78 ml perchloric acid, cooled to 3-5°C. A Pt cathode was used and the nickel wire (anode) was kept in the electrolyte for 1 minute with a voltage of 10 V. This produced smooth and shiny surfaces.

Table 2.2. The chemical analyses of impure (typical) and pure nickel wire provided by Johnson Matthey and Goodfellow. 1 ppm = 0.0001 wt%.

Impure (99.8%)		Pure, thin (99.99+%)		Pure, thick (99.995%)	
Element	Wt%	Element	ppm	Element	ppm
C	0.03	Al	1	Al	< 1
Co	0.02	Ca	10	Ca	< 1
Cu	0.03	Cu	1	Cu	< 1
Fe	0.05	Fe	< 1	Fe	< 3
Mg	0.01	Mg	< 1	Mg	< 1
Mn	0.15	Ag	5	Ag	< 1
S	0.001	Cr	< 1	Mo	2
Si	0.03	Si	3	Si	1
Ti	0.01			Pb	1

2.2 Experimental set-up for electrochemical testing

The YSZ three-electrode pellets (fig. 2.2 A) and nickel wires were polished to create a well defined contact interface. Except for the first experiments (samples 22a, 23o), all samples and supports were cleansed in an ultra sound bath (methylethylketone or ethanol) for 15 minutes and subsequently handled with gloves. The measurement rig was cleaned with pressurised air prior each experiment to remove dust particles before mounting the samples.

2.2.1 Geometry of the set-up

The nickel wires were placed in supporting alumina rods with two holes such that the nickel wires went all the way through one hole and bent back into the other hole (fig. 2.1 B, fig. 2.2 B). The bent nickel wires were positioned on the surface of and pressed against the YSZ pellets with a load of 82 g if not stated otherwise (see table 3.3 for variations), resulting in an average pressure of more than 10 MPa. The alumina rod with the nickel wire was supported by two broader alumina tubes (fig. 2.1 B, fig. 2.2 C).

The measurement rig is a four-wire configuration so two of the wires were short-circuited to accommodate the three-electrode set-up. Fig. 2.1 shows the set-up and the position of the three electrodes. The working electrode is the nickel wire, which is connected to a platinum wire. The reference electrode is a platinum ball, positioned in the bore of the hollow pellet and the platinum paste counter electrode is painted on the lower narrow part of the pellet (Pt-paint type 5542, ESL Europe). As a single electrode (working electrode) is tested, a reference electrode is introduced to avoid unintended interference from the other current electrode (counter electrode). The voltage drop between the working electrode and the reference electrode is accounted for by two contributions: one from the electrode process (polarisation resistance) and one, which is due to ohmic losses in the electrolyte.

The three-electrode pellet was designed at Risø National Laboratory to allow single electrode studies and it has been intensively used and tested. The validity of the geometry has been established and the pellet geometry is ideal as opposed to thin foil electrolytes [7]. The rig with the pellets was mounted in a furnace and heated (6°C/min) to a temperature of 1000°C in an atmosphere of wet hydrogen in nitrogen (9% H₂/3% H₂O). At 1000°C the atmosphere was changed to pure, wet hydrogen (97% H₂/3% H₂O, 100 ml/min).

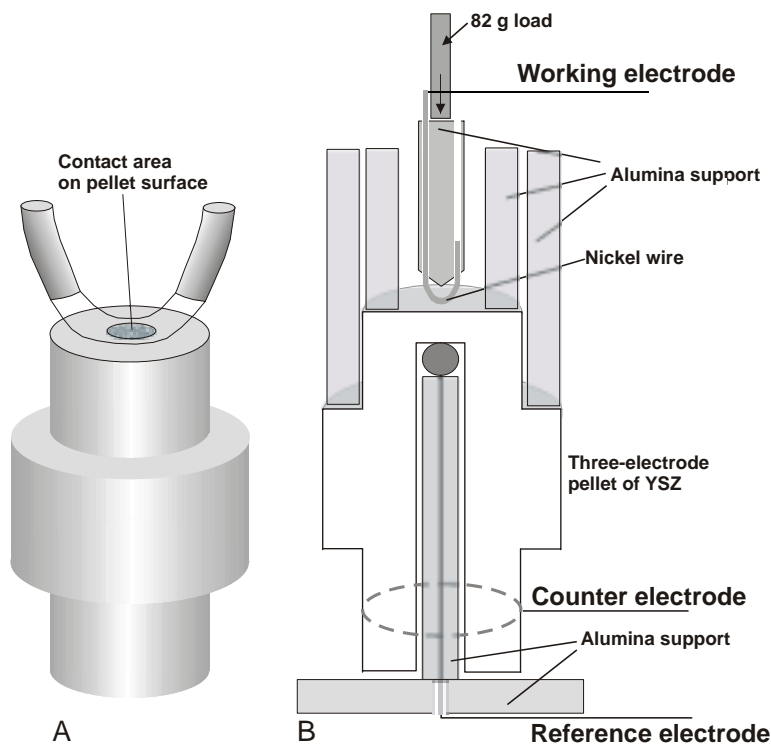


Fig. 2.1. The experimental set-up. A) The nickel wire is pressed against the YSZ surface of a three-electrode pellet, creating an elliptical contact area. B) The nickel wire (working electrode) is supported by alumina tubes and is pressed against the YSZ with a load of typically 82g. The reference electrode is in the bore of the hollow pellet and the counter electrode is painted on the lower narrow part of the pellet.

2.2.2 Electrochemical measurements

Four different treatments were given:

Non-polarised samples:

- Not electrically connected. Heat treatment and pressure only.
- Open circuit voltage (OCV); impedance measurements were performed.

Polarised samples:

- Anodic polarisation (100 mV). Impedance measurements were performed during polarisation and at OCV before and after the polarisation.
- Cathodic polarisation (-100 mV). Impedance measurements were performed during polarisation and at OCV before and after the polarisation.

After stabilisation at OCV (typically 24-72 hours), either anodic or cathodic overvoltages of 100 mV were applied to the respective pellets. The polarisations were continued for 2-7 days after which the pellets were left for up to two days at OCV before cooling down. Impedance measurements were generally repeated every 4-6 hours in the first experiments, every 0.5-2 hours in later experiments, during both OCV and polarisation. The experiments lasted typically 200-300 hours.

Chronoamperometry measurements were performed on a number of samples. In the first experiments, a measurement was done every 10 min throughout the entire experiment. In the later experiments, the measurements lasted between 1 and 17 hours with measurements every 10 seconds. Potential sweep measurements (0 mV-100 mV-0 mV) with different step rate (0.2 - 100 mV/s) were carried out at the end of the polarisation periods.

A Solartron 1260 Impedance/Gain-Phase Analyser was used for measurements at OCV; in the case of polarised samples, a Solartron 1286/1287 potentiostat and a Solartron 1250 Frequency Response Analyser were used. The amplitude of the potential applied was 14 mV RMS. The impedance spectra were recorded in the frequency ranges 0.1 Hz to 65 kHz (1250) and 0.05 Hz to 1 MHz (1260) at 9 or 11 points per decade. All instruments were operated from a PC running FCL [19]. The impedance spectra were analysed with the program EQUIVCRT [20].

After the furnace had cooled down, the samples were dismantled. The nickel and the YSZ separated easily from each other, thus making it possible to examine both surfaces.

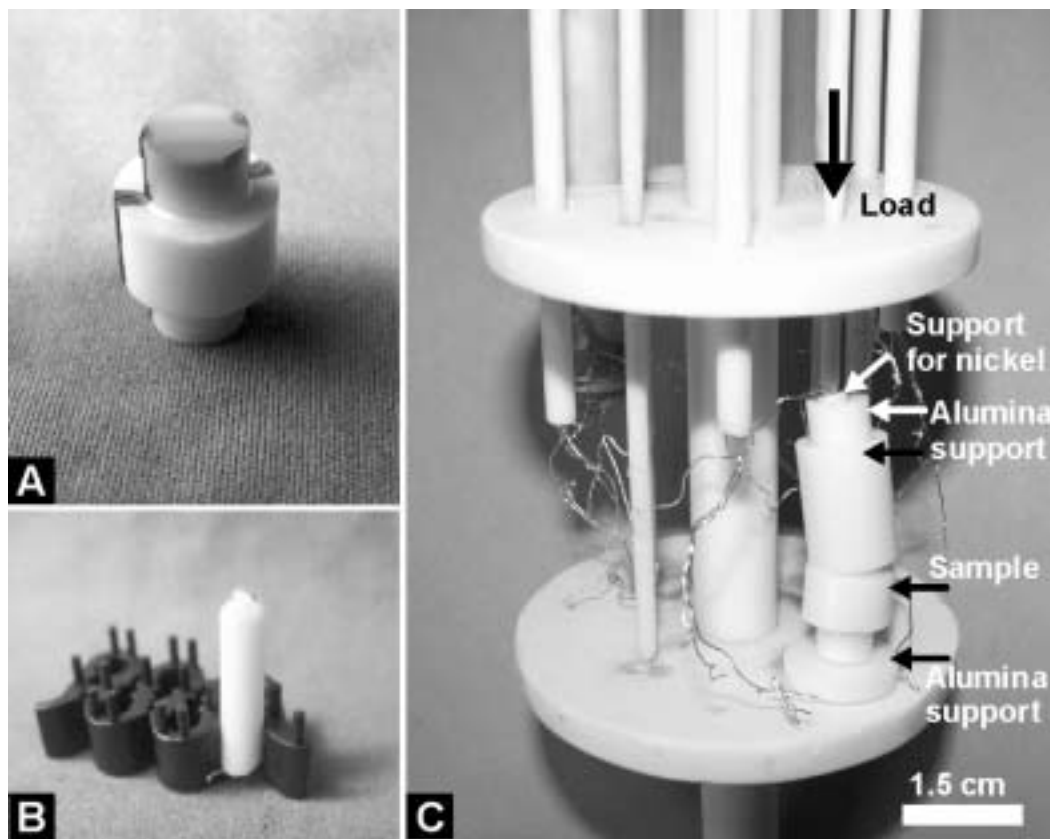


Fig. 2.2. A) Three-electrode pellet. The height of the pellet is 1.5 cm. B) The bent nickel wire in its support. The height of the support is 1.7 cm. C) The sample set-up.

2.2.3 Samples for electrochemical measurements

Table 2.3 presents a list of all the samples, which were tested and examined further. Appendix A contains descriptions of all the performed experiments and comments on the samples, which were not suitable for further examination.

The samples are named according to the experiment number, the sample number and the treatment: Sample code notation: *a*, *c*, *o* and *n* in sample names denote anodic or cathodic polarisation, open circuit voltage and ‘not electrically connected’. The last digit in each code (1, 2, 3, 4) is the sample number in the experiment and the first one or two digits (from 2 to 24) are the experiment series.

Some experiments were performed with loads less than 82 g, see table 2.3. The ‘not electrically connected’ samples included both three-electrode pellets (some of them pre-annealed) and two pre-annealed YSZ single crystals. The type of nickel wire is indicated in table 2.3.

Table 2.3. The samples, which were tested in the 3-electrode set-up and examined further (see Appendix A for a description of all experiments). Pols. = polarisations. SC = single crystal. # indicates thin and pure wires.

	Sample code	Nickel type	Comments		Sample code	Nickel type	Comments	
Anodic polarisation	22a	impure	no cleaning	Open circuit voltage	23o	impure	no cleaning	
	53a	impure			33o	impure		
	92a	pure	#12 h at 1000°C		34o	impure		
	111a	impure	multiple pols.		51o	impure		
	112a	impure	multiple pols.		72o	impure	21 g load	
	161a	impure	pre-annealed		73o	impure	pre-annealed	
	162a	impure			113o	pure	#	
	181a	pure	#		121o	pure	#	
	193a	pure	#		122o	pure	#	
	212a	pure						
	213a	pure						
	221a	pure			Not connected	54n	impure	
	222a	pure				74n	impure	pre-annealed SC
	224a	pure				81n	impure	0.07 g load
			82n	impure		6 g load		
			83n	impure				
			84n	impure				
			164n	impure		SC		
			123n	pure		#		
			124n	pure		#		
			131n	pure		#		
			132n	pure	#			
			133n	pure	#			
			233n	pure				
Cathodic polarisation	52c	impure						
	71c	impure	#					
	184c	pure						
	241c	pure						
	242c	pure						
	243c	pure						

2.3 Other experiments/analyses

Samples for XPS analyses: Four samples of 8 mol% yttria-stabilised zirconia were prepared especially for XPS (X-ray Photoelectron Spectroscopy). The upper 2-3 mm of YSZ three-electrode pellets were cut off to get a sample of a suitable height. The samples 61, 62 and 63 were all polished (section 3.1.1) and cleaned with methylethylketone. During preparation (annealing, cleaning) it was attempted to imitate real experimental conditions. The only

exception was that the pure hydrogen atmosphere could not be achieved and so 9% H₂/3% H₂O in N₂ was used instead.

Sample 67 was crushed to pieces and the fractured surface of a chosen piece (5 by 5 mm) was only subjected to air for a maximum of 15 minutes before the measurements.

The measurements were performed on the surface and at different depths after intervals of ion sputtering.

The four reference samples that were examined are listed in table 2.4.

Table 2.4. The samples for XPS analyses.

Sample	Treatment
61	polished, cleaned in methylethylketone
62	annealed (4 days in air, 1000°C)
63	annealed (4 days in 9% H ₂ /3%H ₂ O, 1000°C)
67	fresh fracture surface, no treatment

Copper/YSZ: To examine if the copper/YSZ interface behaved the same way that the Ni/YSZ interface did, a copper wire was placed on a polished three-electrode pellet and another pellet was put on top as load. The experiment was performed at 1000°C in 9% H₂/N₂. After the experiment, copper crystals were found all over the YSZ surface, primarily in triple points of grain boundaries. Due to copper contamination of the furnace and set-up rig it was less desirable to perform the usual electrochemical measurements with copper.

Samples for TOF-SIMS and XPS analyses: The upper 2-3 mm of YSZ three-electrode pellets were cut off to get samples of a suitable height. The samples were mounted in the usual rig, 231n with a pure nickel wire and 232n with an impure nickel wire. After 216 hours at 1000°C in 97% H₂/3% H₂O with a load of 82 g the samples were dismantled and kept in plastic containers, except for a brief examination in an optical microscope. Contamination of the samples prior to analyses was avoided. The samples were subsequently analysed with the XPS.

Thermally annealed YSZ: A polished three-electrode pellet, sample 151, was thermally annealed for 500 hours in air at 1200°C to establish if the YSZ surface was affected if exposed to higher temperatures and for longer periods of time.

2.4 Methods of analysis

2.4.1 SEM/EDS

After the experiments the surfaces of the nickel wires and YSZ pellets were examined in a scanning electron microscope (SEM: JSM-5310LV or JEOL JSM-840) with respect to the change in morphology and chemical composition. Carbon coating was necessary to prevent charging of the ceramic samples. Chemical analyses were performed with energy dispersive X-ray spectroscopy (EDS: Noran). EDS in combination with the SEM is not an appropriate method for chemical analyses of very small concentrations or very small areas of interest. The interaction volume is in the order of 1 μm³ thus making it very difficult to measure compositions of grain boundaries and other small scale features. All SEM images are secondary electron images unless stated otherwise.

2.4.2 XPS

The XPS technique yields quantitative results of chemical composition of the upper 30 monolayers of a sample.

The reference samples 61-67 were examined using a PHI 550 ESCA system with a double pass cylindrical-mirror analyser (CMA). The analysed areas were approximately 1 cm². The measurements were performed at the Department of Physics at the Technical University of Denmark.

XPS analyses on the samples 231n and 232n were performed using an SSX-100 (Surface Science Instruments, Mountain View, California, USA) with an Al K α X-ray source (1486.6 eV, 15–150 W) operated at a pressure of 3·10⁻⁸ Torr. The analyses were performed at a 55-degree angle to the surface with an analyser pass energy of 150 eV. The Zr 3d line (182.2 eV) was used as a reference to correct for sample charging. It was possible to analyse the contact areas alone. The measurements were performed at the Danish Polymer Centre at Risø National Laboratory.

2.4.3 AFM

Atomic Force Microscopy (Digital Instruments, NanoScope I (University of Oslo) and III (Risø National Laboratory)) was used to obtain 3D images of sample topography and measure heights of the surface structures. Height differences up to 5 μ m can be measured. Typically images up to 20×20 μ m were obtained.

It was necessary to cut the samples to make them fit into the AFM's. Different heights were accommodated by the different microscopes. Cutting involved subjecting the samples to cooling water and a rough treatment.

2.4.4 TOF-SIMS

The TOF-SIMS analyses were performed using a TOF-SIMS IV (ION-TOF GmbH, Münster, Germany) operated at a pressure of 2·10⁻⁸ Torr (with sample). High mass resolution spectra were obtained using 30-ns pulses of 25-keV Ga⁺ (primary ions), which were bunched to form ion packets with a nominal temporal extent of <1.1 ns at a repetition rate of 20 kHz, thus yielding a target current of 1.3 pA. These primary ion conditions were used to scan a 500×500 μ m² area of the sample for 262 seconds, which corresponds to an ion dose of 8.5·10¹¹ ions/cm². Images with a lateral resolution of 150 \pm 50 nm were obtained using 160-ns pulses of 25-keV Ga⁺ at a repetition rate of 20 kHz, thus yielding a target current of 0.6 pA. These primary ion conditions were used to scan 500×500, 50×50 and 20×20 μ m² areas of the sample, which corresponds to ion doses in the range 10¹¹–10¹⁴ ions/cm². A flood gun was used to minimize built-up charge at the surface. Desorbed secondary ions were accelerated to 2 keV, mass analysed in the flight tube, and post-accelerated to 10 keV before detection.

3 Morphology of contact areas

The SEM examinations of the YSZ pellets revealed that when an impure nickel wire was used, the contact areas were very easy to recognise. When pure wires were used, contact areas on anodically and cathodically polarised samples were similarly easy to find. For non-polarised samples the contact areas were at first impossible to find with the SEM. The carbon coating provided a larger contrast between the contact areas and the surrounding area and most contacts were then first found and marked in the optical microscope and afterwards examined with the SEM.

Both the impure and the pure nickel wires showed negative imprints of the YSZ surface and the developed structures. Stretching cracks are seen in the nickel wires as a result of bending and pressure from above.

Section 3.1 describes the structures that developed on the samples with impure electrodes. In section 3.2 structures found on samples with pure wires are described and finally, in section 3.3, structures developed on thermally annealed YSZ is described. The results are compared and discussed in section 3.4.

It should be noticed that in most of the 3D-AFM images shown, the scale on the Z-axis is different from the scale on the X-and Y-axes.

3.1 Samples with impure nickel wires as electrodes

The surface of the YSZ pellets may, after the experiments, be divided into the following elements (fig. 3.1.):

- a) A fracture in the centre of the contact area.
- b) A hill and valley structure where most grain boundaries are hard to distinguish. The areas appear disordered and are found closest to the fracture.
- c) A structure where grain boundaries are very conspicuous and where round or elliptical holes may be found within the grains.
- d) Structures which presumably are transition structures between b) and c). The grain boundaries are visible and the grains show a hill and valley structure.
- e) A rim ridge of impurities positioned at the contact area border. The ridge is not necessarily well developed along the entire circumference and is undetectable in some locations.
- f) The YSZ surface outside the contact area, which only shows changes caused by thermal annealing at grain boundaries.

In the centre of the contact area where the pressure was highest, a piece of YSZ adhered to the nickel wire and thereby an elliptical fracture was created in the YSZ. The depths of the fractures vary from 8 to 32 μm .

In the area where the pressure was less, the nickel and YSZ separated without deformation or destruction of the contact area (b, c and d) and here the hill and valley structure was revealed. Impurity particles were found in the interfacial region, superposed on the hill and valley structure (fig. 3.2).

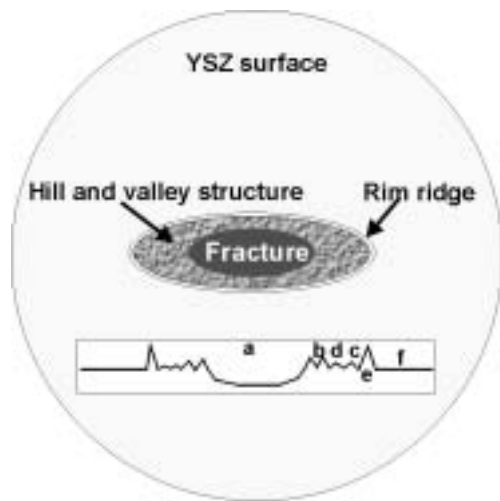


Fig. 3.1. A schematic drawing of a pellet surface after an experiment. A line profile through the contact area is shown. The letters a-f are referred to in the sections 3.1 and 3.1.2. The drawing is out of scale.

3.1.1 Contact areas on the YSZ pellets

The contact areas were easy to distinguish as they all developed the characteristic morphology (fig. 3.2) described above.

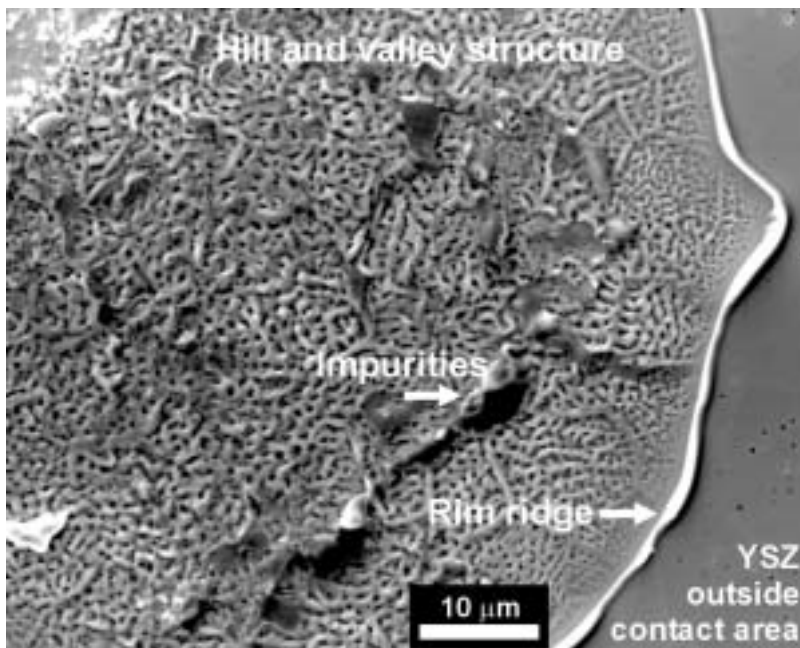


Fig. 3.2. An overview of the changes at the interface of the sample 51o. The hill and valley structure developed all over the contact area as compared to the YSZ outside the contact. Along the contact area boundary the rim ridge is developed. In the contact area large impurity particles are found superposed on the hill and valley structure.

The contact area border is sharp and delimits the propagation of the developed structures. The outer limits of the contact areas are characterised by a ridge of impurities (chapter 4).

The contact areas are generally elliptical (expected from the shape of the nickel wire) in circumference with an average aspect ratio of 2.93. The average lengths of the ellipse axes are 453 μm and 148 μm. The average contact area for samples with 82 g load is 0.060 mm². The variations are given in table 3.1. The topography of the contact areas results in a physical contact area, which is larger than the area measured by the dimensions of the ellipse. With the atomic force microscope it was possible to measure both areas and it was found that the topographical area is approximately 10% larger than the geometrical area. This is not taken into consideration in table 3.1.

Table 3.1. The smallest, largest and average values of contact area parameters for samples with 82 g load. 16 samples were measured.

	Area [mm ²]	Aspect ratio	Circumference [mm]	Long axis [μm]	Short axis [μm]	Pressure [MPa]
Smallest	0.033	2.28	0.87	375	110	8.8
Largest	0.093	4.63	1.68	671	206	16.9
Average	0.060	2.93	1.16	453	148	14.4
St.dev.	0.014	0.63	0.17	76	25	3.8

Table 3.2 collects some parameters for samples with loads less than 82 g. There are only three such samples so whether or not these values are typical is uncertain. The contact area decreases with load even though the 21 g load sample has an area comparable to areas found for the 82 g load samples.

Table 3.2. The size of the contact area, the aspect ratio and the average pressure for samples with loads less than 82 g. For a comparison, the average contact area for samples with 82 g load was 0.060 ± 0.014 mm².

Load	Area [mm ²]	Aspect ratio	Pressure [MPa]
21 g	0.044	2.66	4.17
6 g	0.0051	2.59	11.8
0.078 g	0.00053	1.94	1.5

3.1.2 Description of structure types

The three hill and valley structure types (b, c, d) mentioned in section 3.1 grade into each other and no clear limits can be set. In the areas closest to the border, the amplitude and wavelength of the structures often decrease toward the rim ridge (fig. 3.2).

3.1.2.1 Structure with holes in the grains (type c)

The structure with holes in the grains is always seen in a narrow zone close to the rim ridge (fig. 3.3). It is possible to correlate grains and grain boundaries outside the contact area across the rim ridge and into the contact area. The appearance of the grain boundaries change when they cross the rim ridge, From showing grooves and shoulders outside the contact area they become wider with material accumulating in the middle and a groove developing on each side (fig. 3.3 A).

The grains in this zone develop holes. The number of holes in each grain is random, a few may be found or the whole grain is covered. The shape of the holes varies from grain to grain. In some grains the holes are round; in others they are elongated. In the case of elongated holes, a distinct alignment along certain directions is seen (fig. 3.3 B). The diameter of the holes is up to 1 μm. The depth of the holes is in the order of 25-40 nm (measured on one sample only).

This structure was not found on all samples.

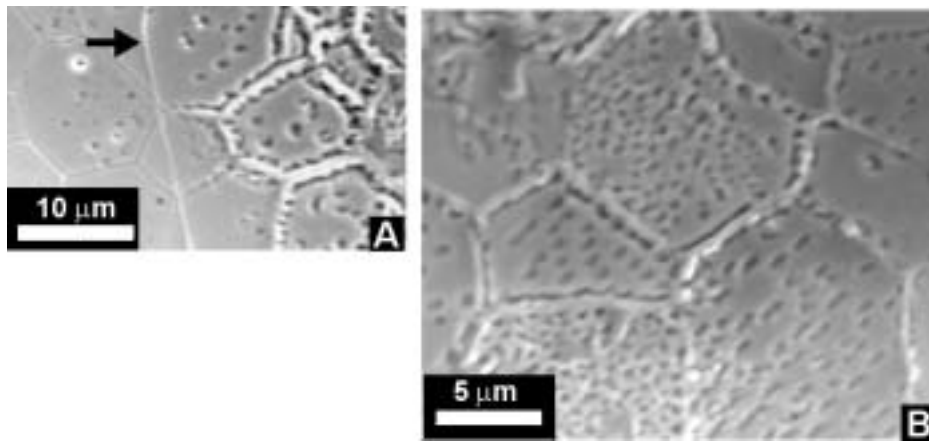


Fig. 3.3. Sample 33o. A) The grain boundaries outside the rim ridge (arrow) show signs of thermal annealing: grooves and shoulders. In the contact area the grain boundaries are characterised as wider, with material accumulating in the middle and a groove on each side. B) In the grain interior, holes start to develop. In some grains they are elongated and aligned and in others they are distributed more randomly.

3.1.2.2 Hill and valley/pyramidal tips transition structure (type d)

Between the two structure types b) and c) there is an area where grain boundaries can still be recognised. They are thicker and more massive than the hills (fig. 3.4). Thus the grains may be identified and within each grain the hill and valley structure is found. The appearance of the hill and valley structure may differ from grain to grain. Some grains are showing a weak or strong alignment of the hills and valleys. In other locations, all grains in an area may look alike with no preferred orientation of the hill and valleys. A close-up of the hill and valley structure is shown in fig. 3.4. The widths of the hills and valleys are regular around 0.4-0.5 μm .

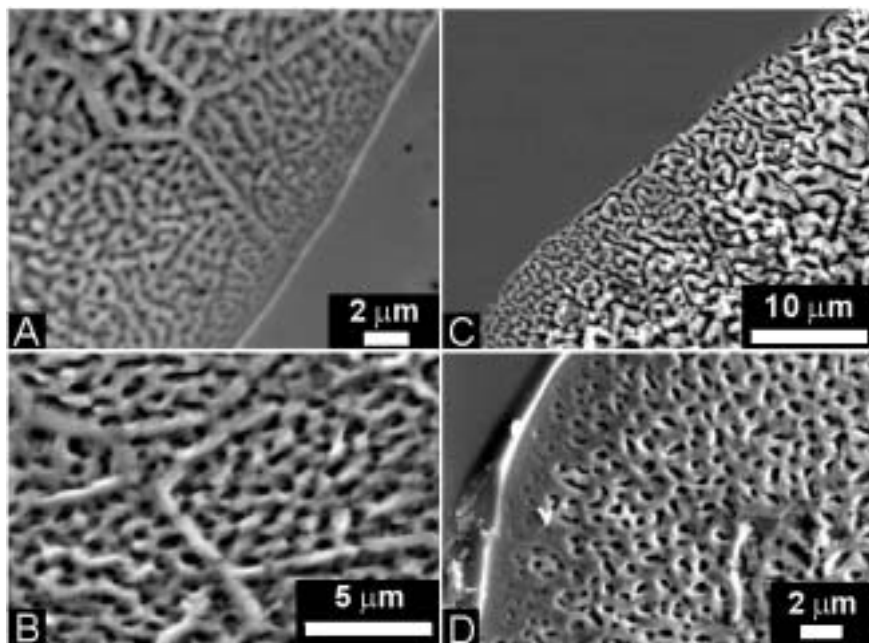


Fig. 3.4. A) and B) The hill and valley structure on the samples 83n and 51o at higher magnifications. The grain boundaries are massive and the dimensions of these as well as of the hill and valley structure decrease toward the contact area boundary. C) and D) Hill and valley structures on the two single crystal samples (74n and 164n).

In fig. 3.5 an AFM image of a whole grain with a hill and valley structure is seen. Some alignment of the hills is recognised. The line profiles (fig. 3.5 B) show the varying topography across the grain. The grain boundaries, even though they seem massive, are only recognised clearly in one of the profiles. A close-up of the hill and valley structure on one of the single crystal samples (fig. 3.6) shows that the hills consist of pyramidal shaped tips. The pyramids are often well aligned and showing similar orientations of the sides. The amplitude of the hills and valleys is around 100 nm.

3.1.2.3 Hill and valley structure/ pyramidal tips (type b)

The areas near the centre of the contact area (and the fracture) are characterised by a structure, which consists of hills and valleys (fig. 3.2). On an overview scale the hills make up a semi-network with isolated valleys. The structure may look rather chaotic or messy due to the unidentifiable grain boundaries. These are in most cases blurred or integrated in the hill and valley structure so that single grains cannot be distinguished. Impurities are lying as big islands or bands (e.g. 2 μm wide and 30 μm long in fig. 3.2) on the surface and contribute to the messy look (fig. 3.2). In the AFM this structure type is looks similar to the one from type c with well developed pyramids.

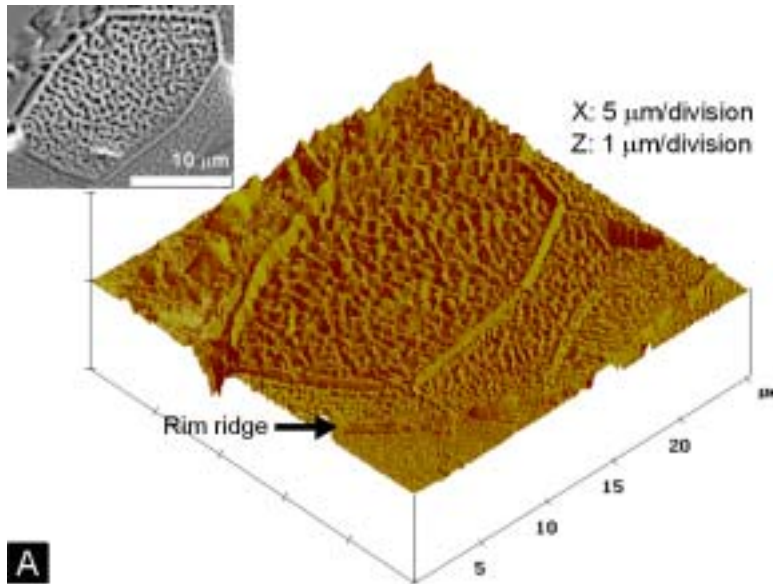
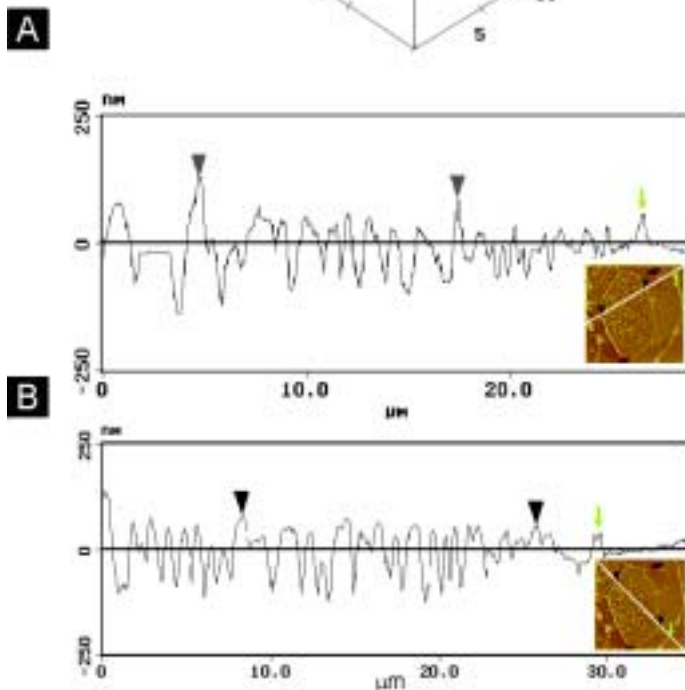


Fig. 3.5. A) AFM image of a complete grain on sample 84n. The inset shows the corresponding SEM image. The hills are aligned in a direction approximately parallel to one of the sides of the image. The rim ridge is seen (arrow).



B) Two line profiles through the grain from fig. 3.5 A. In both line profiles the black arrows mark the grain boundaries and the green arrows mark the rim ridge. In the upper line profile, the grain boundaries are higher than the surrounding hills. In the lower line profile this is not as conspicuous even though the boundaries appear more massive.

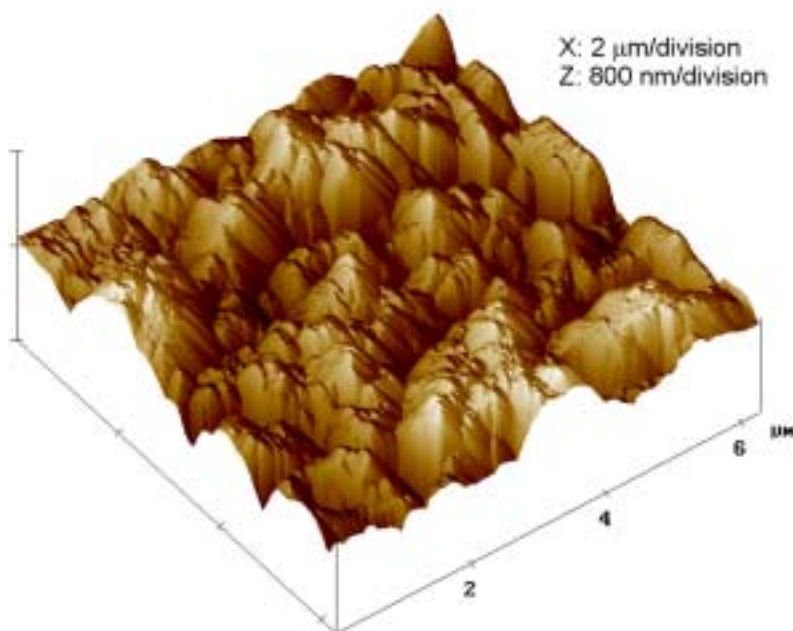


Fig. 3.6. A 6.2 μm by 6.2 μm AFM image of the hill and valley structure on the single crystal (74n). At a close range the hills resemble pyramids.

3.1.2.4 Structures on single crystal samples

Two samples of a pre-annealed single crystal of 10 mol% YSZ were examined and both show the hill and valley structure (fig. 3.4 C, D and 3.6). Fewer impurities are present in the single crystal but still the rim ridge is developed, weakly on one of the samples (74n), and more well developed on the other (164n) (fig. 3.4D). Large impurity particles in the interfacial region are abundant.

3.1.2.5 Pre-annealed three-electrode pellets

No significantly different structures from the already mentioned were found on these samples.

3.1.3 The rim ridge

The chemical composition and formation of the rim ridge is treated in chapter 4. In this section only the physical appearance is described.

The height of the ridge has been measured on several samples and reaches up to 1.6 μm . The height is not constant along the contact area border on the samples, but may vary from nanometres to microns (fig. 3.7 A, 3.8 A and 3.9 A). The width can be up to 4 μm but varies. The shape is mostly triangular in cross section (fig. 3.7) but the ridge may have more than one peak. The figures 3.7, 3.8 and 3.9 show atomic force microscopy images of the rim ridge and illustrate the different morphologies of the ridge.

The ridge is usually not well developed along the entire contact area boundary and is even undetectable in certain places. On a number of samples the fracture completely removes parts of the contact area boundary, preventing a measurement of the rim ridge coverage of the circumference. The typical rim ridge coverage is estimated to be 70-90% of the circumference of the contact area.

On one pellet (33o), a ring shaped ridge was found within the contact area (fig. 3.10). The YSZ surface inside the ridge had no hill and valley structure but was comparable to the YSZ outside the contact area. On the corresponding nickel wire a pore with the same size and geometry was found (fig. 3.10). Obviously no direct contact between the nickel and the YSZ had occurred within this ring.

3.1.4 Other features concerning the YSZ contact area

Due to the geometry of the experimental set-up it is not possible to produce contact areas, which all are regular and perfectly elliptical. Every contact area has something characteristically different: an irregular shape, extension of the fracture, which is ripping out more of the YSZ, “islands” within the hill and valley area, which may originate from irregularities in the nickel wire (fig. 3.11 A). “Fingers” are seen both in the nickel and the YSZ where the hill and valley area ends in thin stripes (fig. 3.11 B).

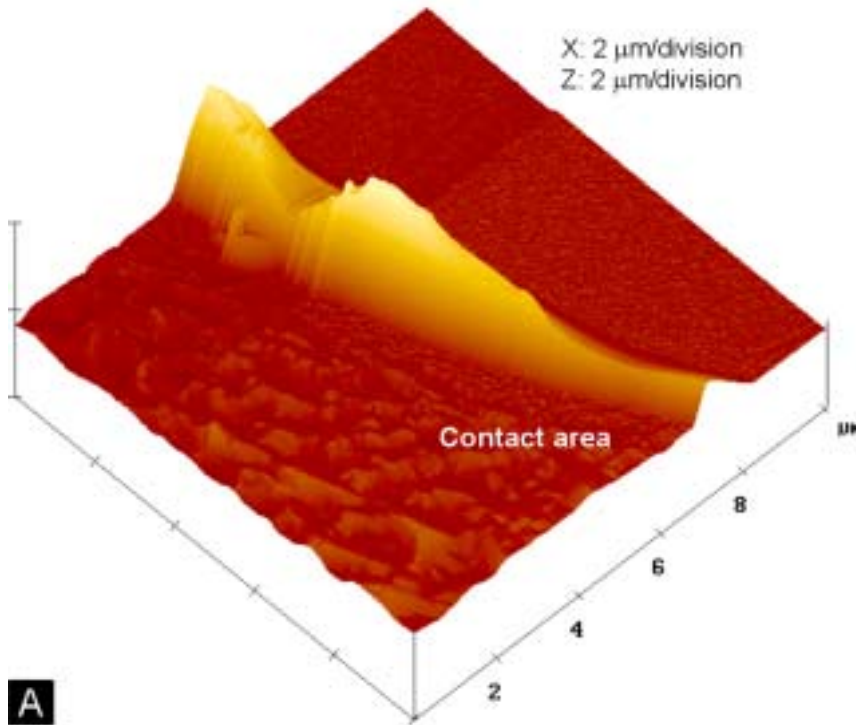
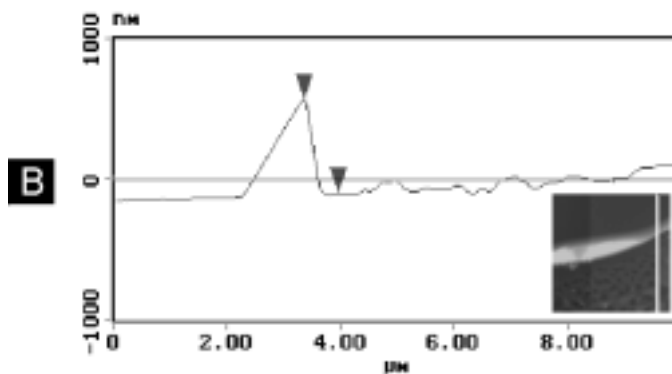


Fig. 3.7. A) AFM image of the rim ridge on sample 51o. The hill and valley structure is seen in the contact area.



B) Line profile of the rim ridge. The vertical distance between the arrows is 665 nm. The triangular shape is clearly recognised.

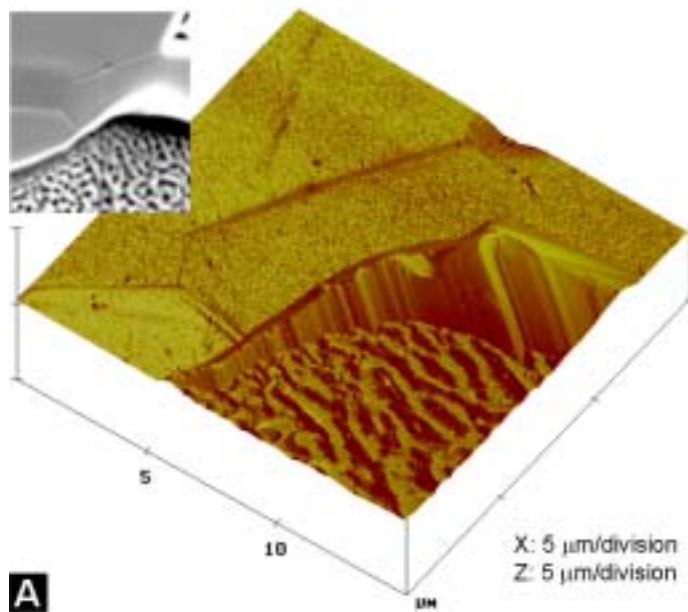
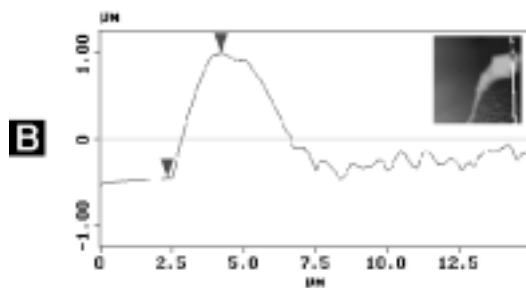


Fig. 3.8. A) AFM image showing the rim ridge and structures both outside and inside the contact area on sample 84n. The inset shows a SEM image of the same area.



B) Line profile of the rim ridge in fig. 3.8 A. The inset shows the position of the line profile. The vertical distance between the arrows is 1.43 μm .

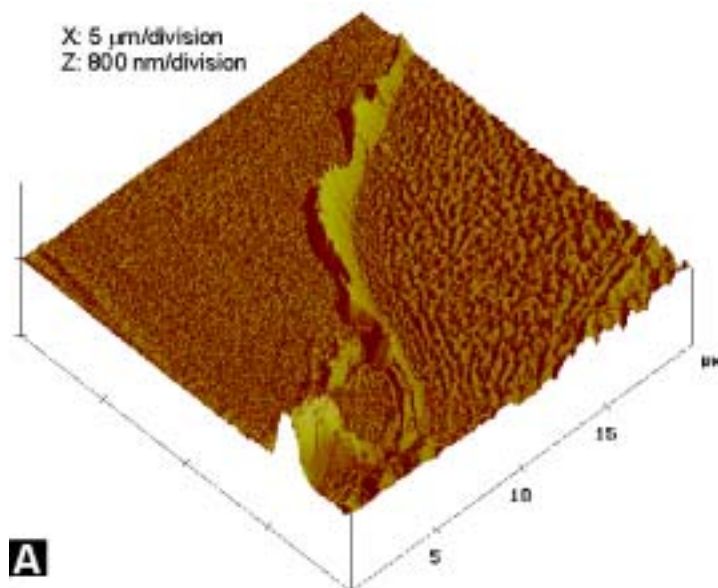
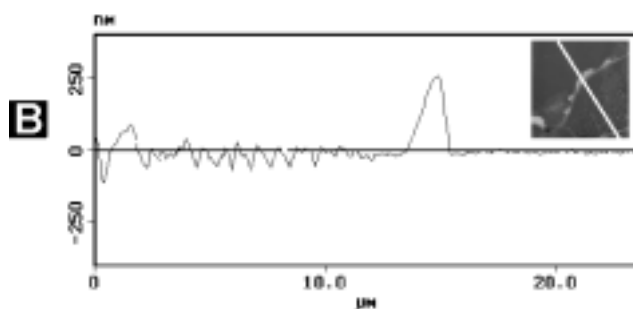


Fig. 3.9. A) The rim ridge and the hill and valley structure within the contact area on sample 84n.



B) Line profile showing the topography of the YSZ along a line starting outside the contact area, crossing the rim ridge and ending in the hill and valley structure (left side).

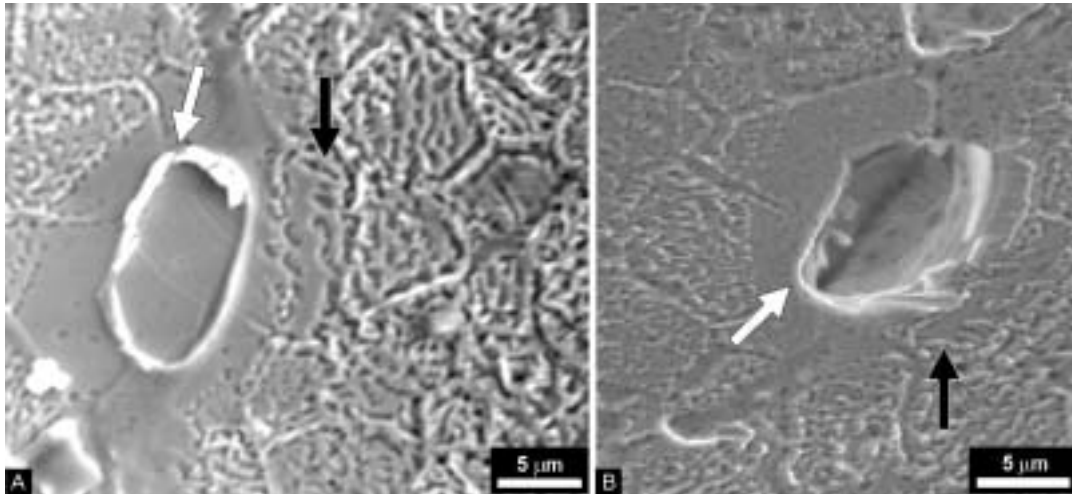


Fig. 3.10. A) A small, ellipse shaped ridge of impurities was found in the contact area on sample 33o (the inner rim ridge). Inside it the hill and valley structure was absent. B) The corresponding contact area on the nickel contact area showed a pore in the nickel. The two pairs of arrows mark corresponding points in the two images.

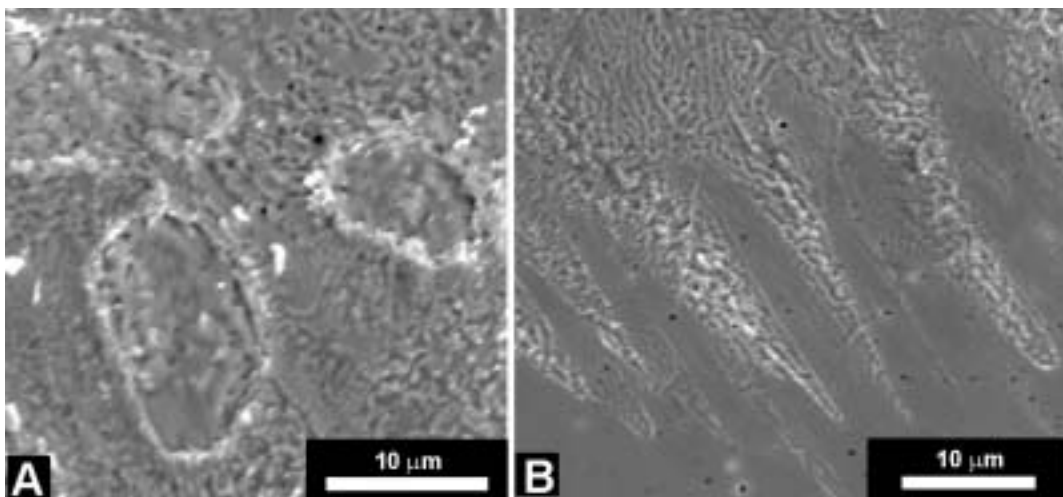


Fig. 3.11. A) Islands with different structures on sample 53a. B) Areas where the contact area border showing 'fingers' are found on a few samples (e.g. sample 53a).

3.1.5 The nickel wires

Due to the load and the temperature, the nickel wire changes shape during the experiments and the contact area increases with time. The rounded tip of the nickel wire becomes flat and the radius of curvature becomes larger.

The contact areas on the nickel wires were easily distinguished as they were relatively flat compared to the nickel outside the contact area, where terrace structures formed as a result of thermal annealing (fig. 3.12). The contact areas were raised a little and the grain boundaries and hill and valley structure of the YSZ were neatly imprinted onto the nickel (fig. 3.13). A direct correlation between grains, grain boundaries, impurity particles/imprints and even hills and valleys were possible.

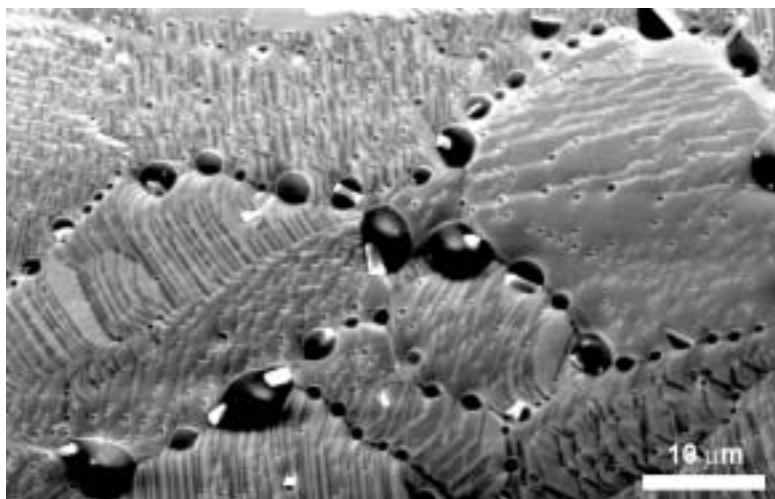


Fig. 3.12. Nickel terraces were formed outside the contact area. The grains develop different facets, depending on the crystallographic orientation of the grains. Bright and dark impurity particles (chapter 4) are seen in the grain boundaries and in the kinks and corners of the individual terraces.

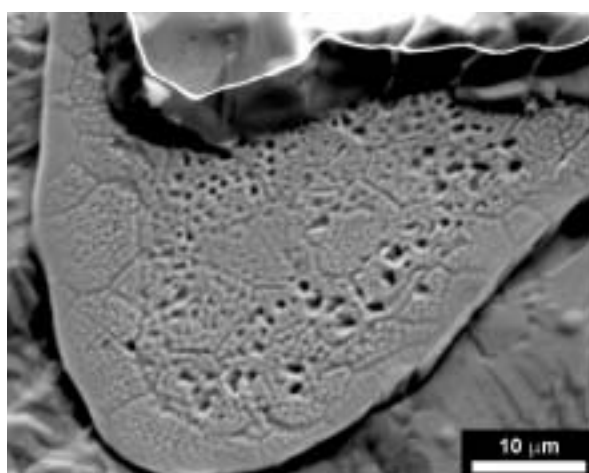


Fig. 3.13. The contact areas on the nickel wires (sample 52c) show imprints of the YSZ grain boundaries, the hill and valley structures developed in the YSZ and the impurities, which are now positioned on the YSZ part of the contact. In the upper part of the picture a piece of YSZ is adhering to the nickel.

3.2 Pure nickel wires as electrodes

The YSZ contact areas on non-polarised samples were very difficult to find. They did not have the same characteristics as the contact areas where impure nickel electrodes were used. The contact areas on the samples subjected to polarisation were on the other hand easily identified. The contact areas on the nickel wires (fig. 4.5) were relatively easy to find and often it was from those that the sizes of the contact area were determined. Both 0.25 mm and 0.5 mm nickel wires were used but the thinner wires did not show reproducible results, probably due to the thickness, which decreased after electropolishing. The thicker wires showed satisfactory reproducibility.

3.2.1 Contact areas on the YSZ pellet

The contact areas on non-polarised, anodically and cathodically polarised samples developed three different types of structures.

The contact areas are elliptical with an aspect ratio of 2.5 ± 0.4 for the thick wires and 3.3 ± 1.0 for the thin wires. The thin nickel wire produced contact areas, which in average are 0.034 ± 0.017 mm² but actually two groups of sizes were identified, one around 0.03-0.05 mm² and one below 0.01 mm². The contact areas on the thick nickel wires are 0.112 ± 0.042 mm². In table 3.3 selected parameters for samples with thick nickel wires are listed. All samples with pure nickel wires were loaded with 82 g. In the following sections, the focus will be mainly on the pure, thick wires. One exception is the sample 92a, which due to the short polarisation time, is very

interesting with respect to the development of the structures with time. Sample 124n was examined in the AFM, and some of the images are shown in section 3.2.2.1.

Table 3.3. The contact area size, aspect ratio, length of circumference, the short and long axes and the average contact area pressure for samples with a thick, pure nickel electrode. 11 samples were measured.

	Area [mm ²]	Aspect ratio	Circumference [mm]	Long axis [μm]	Short axis [μm]	Pressure [MPa]
Smallest	0.058	1.61	1.62	420	156	4.4
Largest	0.188	3.1	3.87	832	304	12.9
Average	0.112	2.5	2.48	610	250	7.6
Stdev.	0.042	0.4	0.95	134	43	3.2

3.2.2 Descriptions of structures

3.2.2.1 Non-polarised samples

The grains in the contact area had developed a hill and valley structure (fig. 3.14). In some grains the structure is more developed than in others and different orientations of the hills are found in different grains (fig. 3.14, 3.15 A). In certain grains the hills appear longitudinal whereas in others they look more like single tips (fig. 3.16). The AFM show as expected from SEM images a much lower topography (fig. 3.15 and 3.16) than for samples with impure electrodes. The measured amplitudes are 30-40 nm for the hill and valley structure but otherwise the pyramid structure (fig. 3.15 and 3.16) resembles the one found on samples with impure nickel wires (fig. 3.5 and 3.6). The grain boundaries within the contact area are wider than the grain boundaries in the YSZ outside the contact. The morphologies of the grain boundaries are characteristic for thermal annealing: grooves and shoulders. Exact imprints of the structures developed in the YSZ are found in the nickel wire (fig. 3.17).

A small rim ridge was seen on the contact area border (fig. 3.14 and 3.15 B). In many places it is barely visible in SEM images. AFM examinations show that the height varies between 13 and 50 nm and width was measured to 150-250 nm. The typical rim ridge coverage on non-polarised samples with pure nickel electrodes is estimated to be 50-70 %.

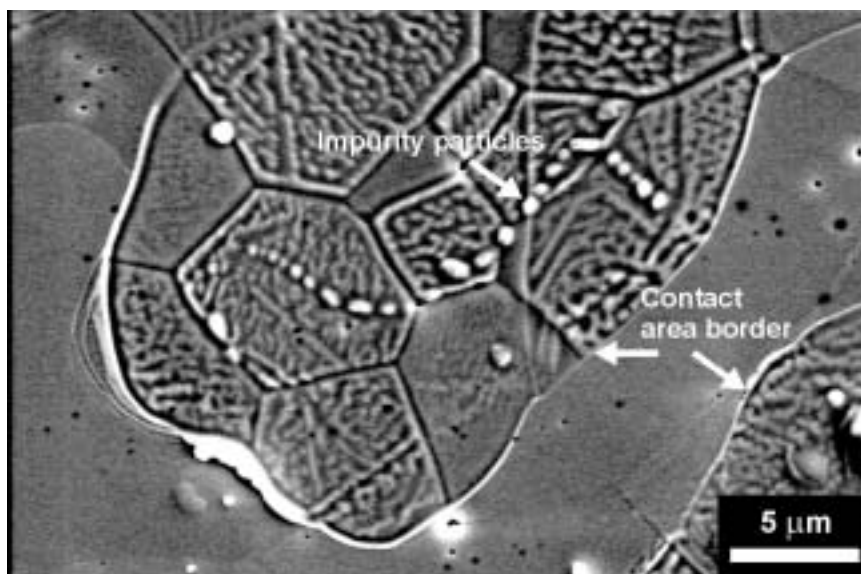


Fig. 3.14. SEM image of the hill and valley structure developed on non-polarised samples (233n). The grains show different hill and valley structures and both impurity particles and a rim ridge are seen.

Fractures or ripped out grains in the YSZ were not found. Impurity particles were found in the contact area (fig. 3.14), often in ellipse shaped formations roughly following the contact area but with a smaller radius (fig. 3.17 inset). Corresponding marks were observed in the nickel side of the contact area (fig. 3.17).

In the YSZ contact area, small areas, where pores in the nickel wire prevented contact between the Ni and YSZ were observed. Thin rim ridges were found along the border of these areas.

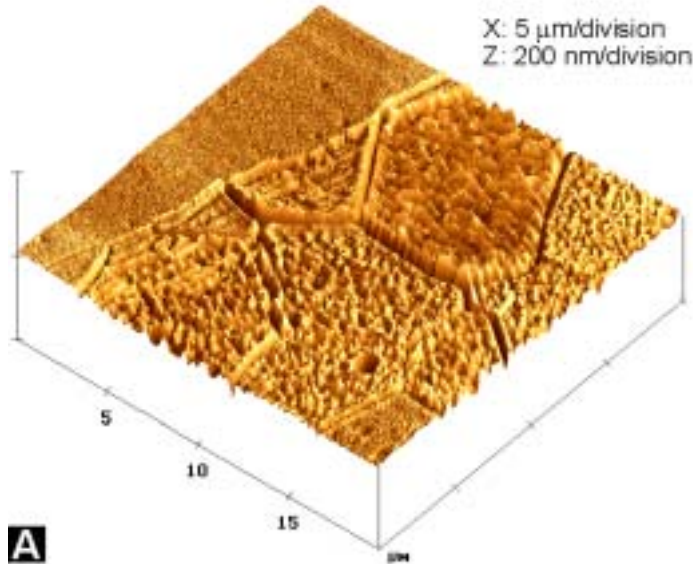
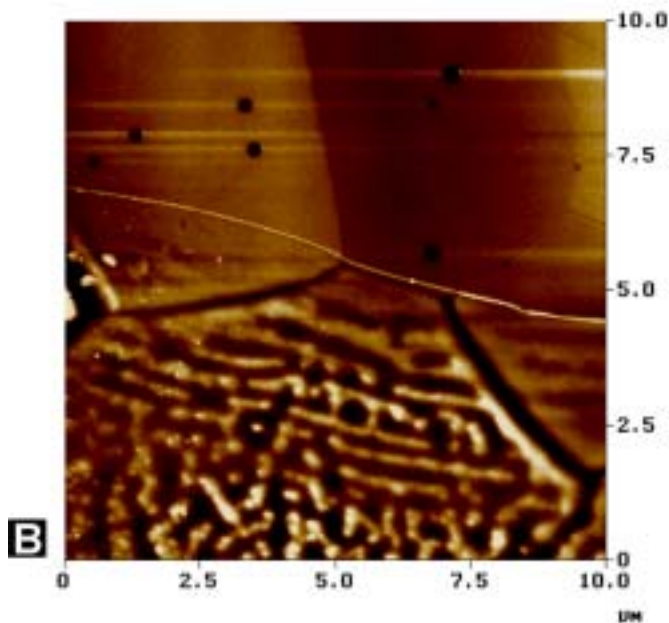
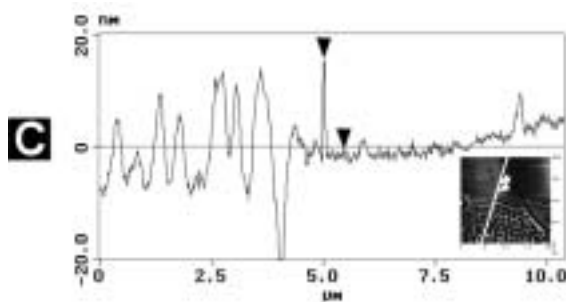


Fig. 3.15. A) AFM image of grains in the contact area of a pure sample (124n). The rim ridge is not very conspicuous in the 3D-image. Each grain shows its own version of the hill and valley structure.



B) 2D-AFM image of a part of image fig. 3.15 A. Light areas are high and dark areas are low. The rim ridge is seen as a thin, white line through the image. In the contact area a hill and valley structure has developed.



C) The line profile shows that the rim ridge is around 18 nm high in this place (arrows). The width of the rim ridge is 150 nm.

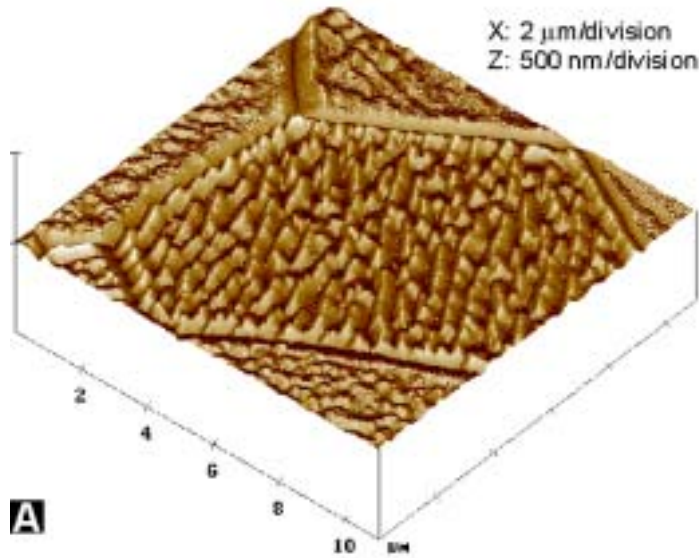
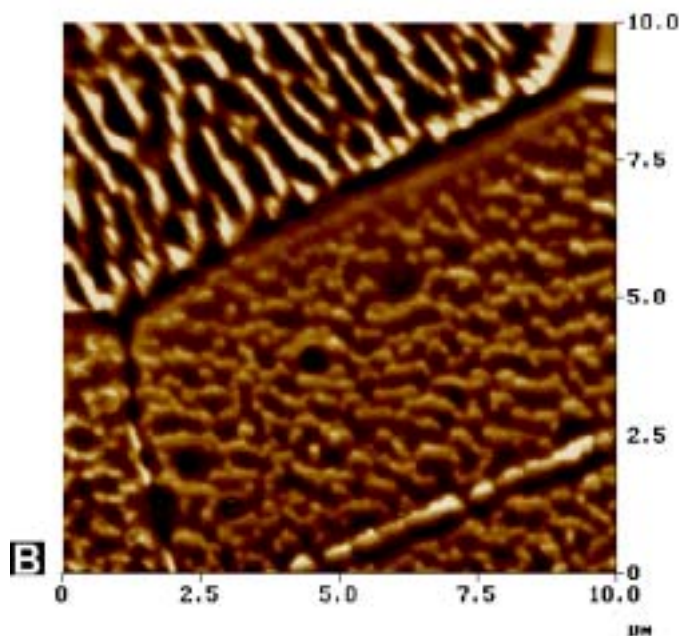
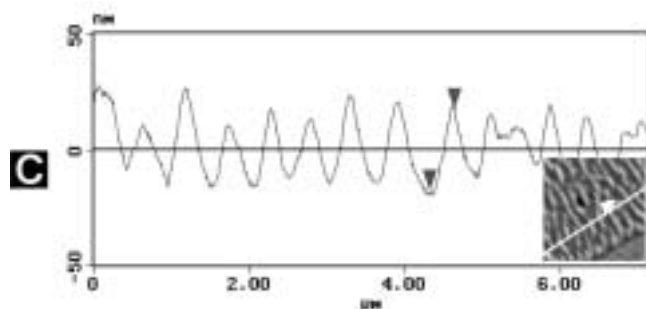


Fig. 3.16. A) AFM image of the hill and valley structure (sample 124n) of one of the grains from fig. 3.15a. The pyramid-shaped hills are aligned in regular patterns. Along the grain boundaries there is a row of pyramids.



B) 2D-AFM image of the grain in fig. 3.16 A and its neighbour. Light areas are high and dark areas are low. The structures of the two grains are very different, with a strong preferred orientation of the hills in the upper grain and a weaker orientation tendency in the lower grain.



C) Line profile of the upper grain in fig. 3.16 B. The regularity of the hills and valleys is very distinct. The vertical distance between the arrows is 35 nm. The typical distance between two hills is 500 nm.

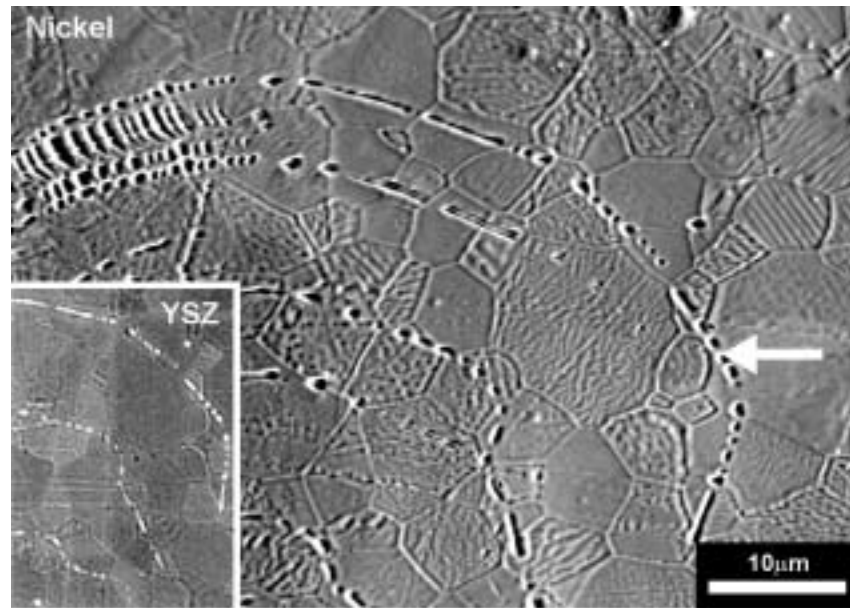


Fig. 3.17. Imprints in the nickel of the hill and valley structure that was developed in the YSZ on non-polarised samples (132n). The marks (arrow) are positioned in an ellipse shape concentric with the contact area. The inset shows the corresponding area on the YSZ sample (rotated and mirrored). Bright particles, which can be directly correlated with the marks in the nickel, are seen.

3.2.2.2 Anodically polarised samples

The anodically polarised samples clearly show a different and topographically higher structure than the cathodically polarised (section 3.2.2.3) and the non-polarised samples. Due to a breakdown of the furnace, the sample 92a experienced only 12 hours at 1000°C with anodic polarisation. In this early stage irregular islands develop (fig. 3.18). The entire contact area is rough and the grain boundaries are visible beneath the structure (fig 3.19). The islands contain bright particles. A rim ridge is not distinguishable but the contact area boundary is well defined (fig 3.18).

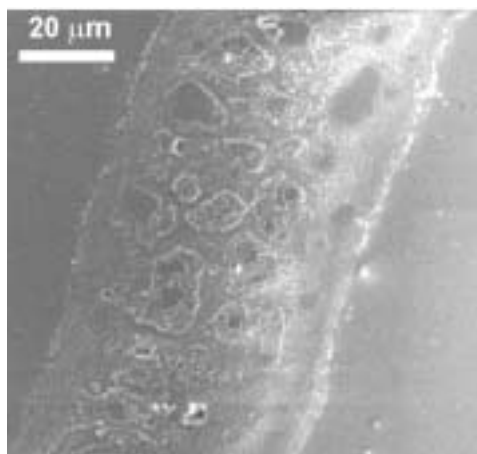


Fig. 3.18. After 12 hours of polarisation the contact area of sample 92a had developed islands.

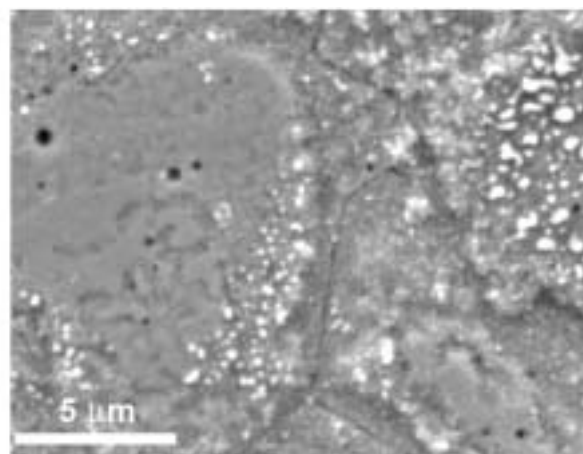


Fig. 3.19. A close-up of 92a. At a close range the YSZ grain boundaries can be distinguished.

Fig. 3.20 is an image of a complete contact area, where the polarisation was held for 53 h. The winding contact area border is typical for samples with thick nickel wires.

Fig. 3.21 (area α in fig. 3.20) shows typical contact area structures formed on anodically polarised samples. The contact area boundary is well defined. Holes after ripped out YSZ grains can be seen. In the contact areas of the samples 213a and 221a larger fractures were observed. Generally, two different kinds of morphologies can be distinguished (A and B). A-areas show relatively flat grain surfaces with bright Ni particles up to 1 μm in diameter. The grain boundaries seem wide and open. The B-areas are characterised by a structure made up of nano-sized particles, primarily of YSZ. Ni particles are also found on this layer. In fig 3.22 close up images of the two types of structures are shown.

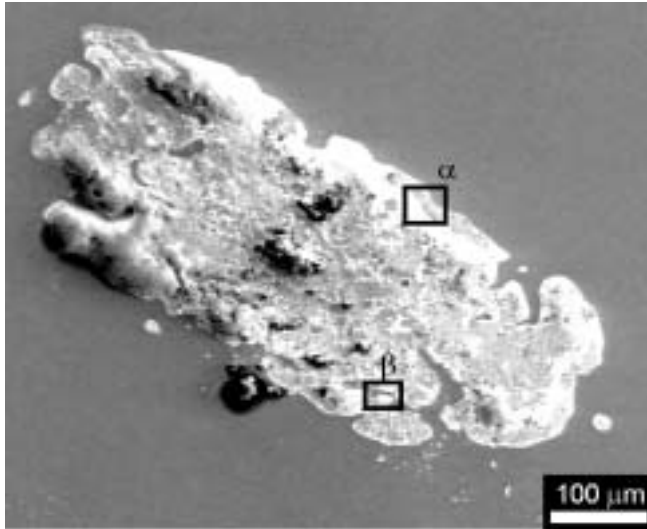


Fig. 3.20. SEM image of the complete contact area on sample 224a. Notice the winding contact area border. Compare the area α with fig. 3.21 and the area β with the figs. 3.23 and 3.24.

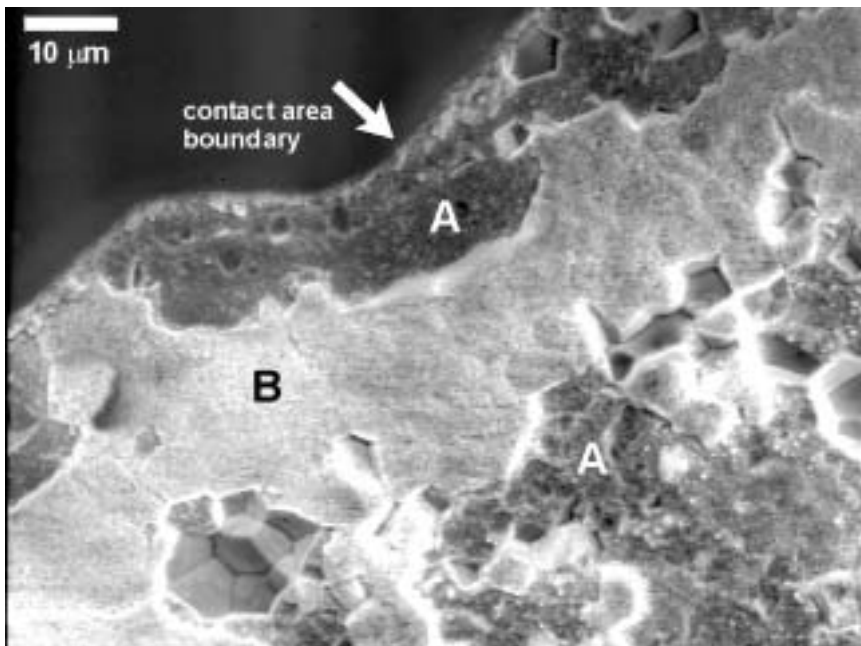


Fig. 3.21. SEM image of the area α in fig. 3.20 showing the A- and B-structures found on anodically polarised samples (224a). The structures are seen in a close-up in fig. 3.22.

The AFM image of a contact area boundary in fig. 3.23 shows areas of both A- and B-structures and YSZ outside the contact area (E-areas). The line profile reveals that the thickness of the interface layer is 600-700 nm but a thickness of up to 1.2 μm has been measured elsewhere. The A-areas are believed to represent the bottom level of the interface layer and B-areas probably represent the top of the layer.

In the contact areas on the nickel, the layered structure is also recognised and two corresponding structures, C and D, are seen (fig. 3.24). The missing YSZ grains are sitting on top of the

interface layer, which is easily recognised. Fig. 3.25 is a schematic drawing of the geometry of the interface layer and the A-, B-, C- and D-surfaces.

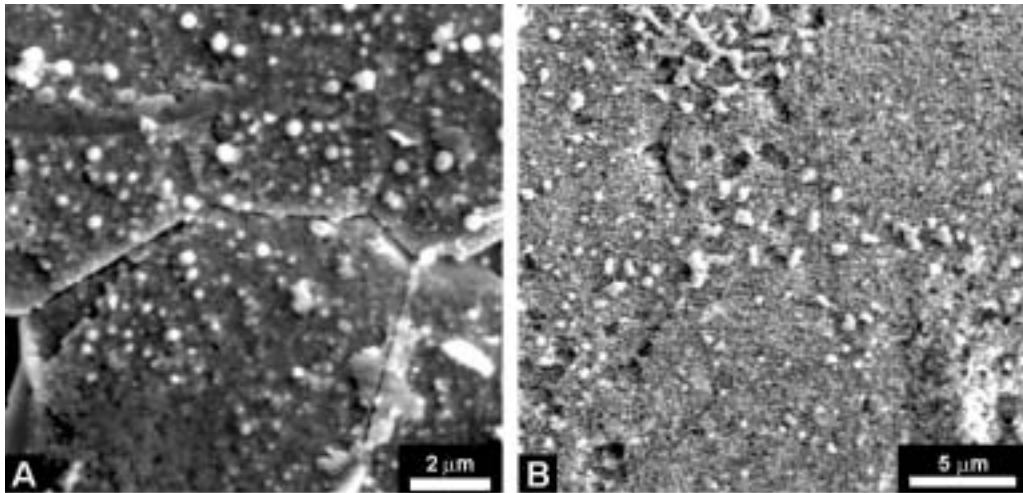


Fig. 3.22. A) SEM image of the A-surface. The grain boundaries seem wide and open. Bright Ni particles are seen on the grain surfaces. B) The morphology of the B-surface indicates a structure consisting of nano-sized particles. Nickel particles are also found on top of this layer.

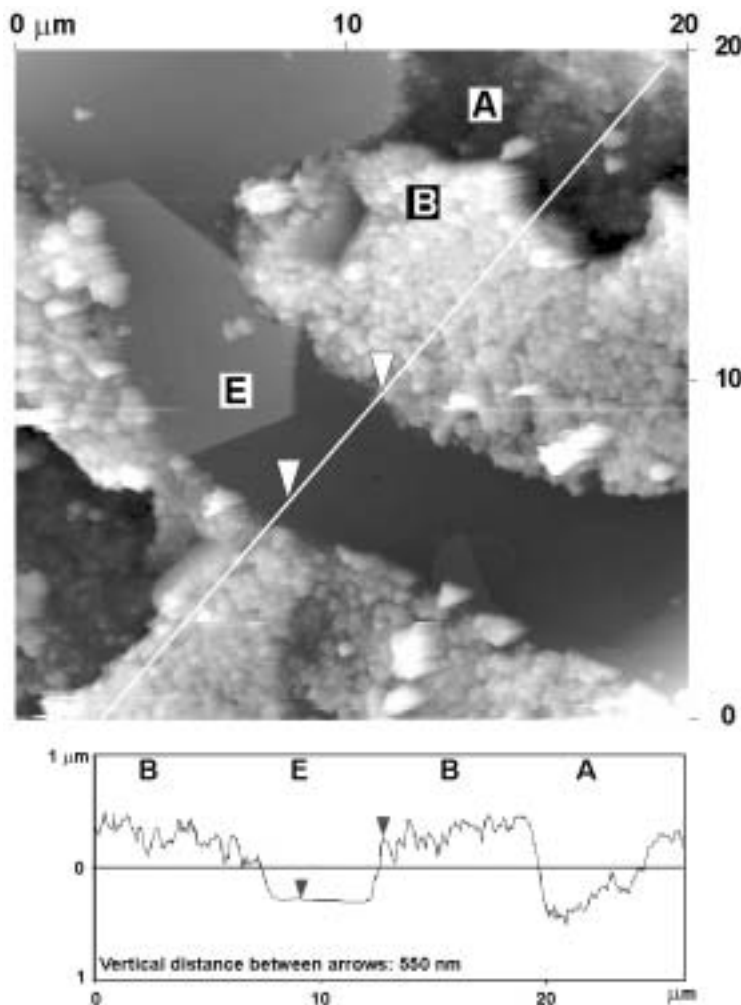


Fig. 3.23. 2D-AFM image of an anodically polarised sample (224a, area β in fig. 3.20) at a location where the contact area border is winding, see fig. 3.20. A and B refer to the two structure types, and E is the YSZ surface outside the contact area. Light areas are high and dark areas are low. The line profile shows the height relations between the A- and the B-structure. The two arrows mark corresponding points. The thickness of the interface layer is 600-700 nm.

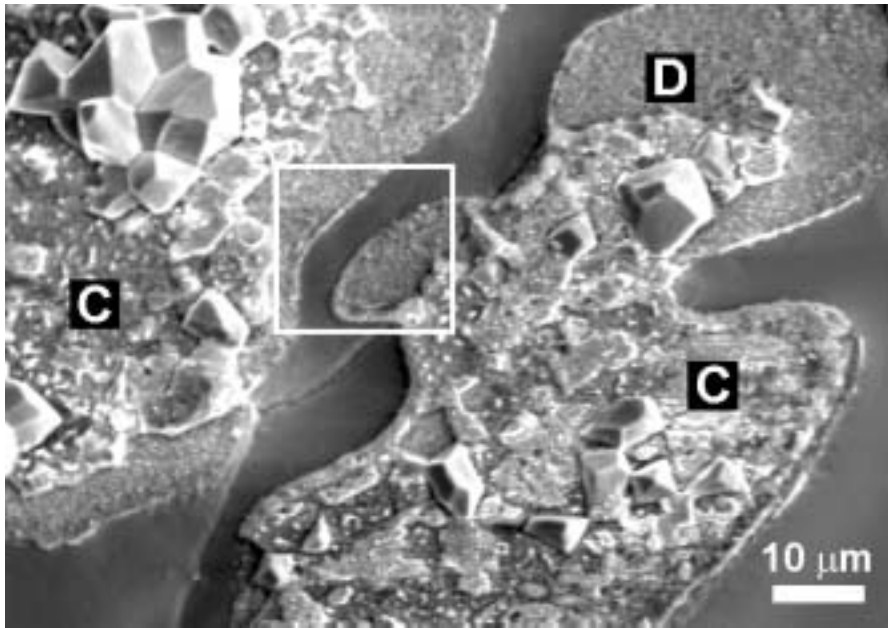


Fig. 3.24. SEM image of the contact area on the nickel wire of sample 224a. The C-surface is the interface layer adhering to the nickel. The D-structure corresponds to areas where the interface layer stayed on the YSZ part of the contact area. Compare with fig. 3.23 where the YSZ part of the framed area is seen.

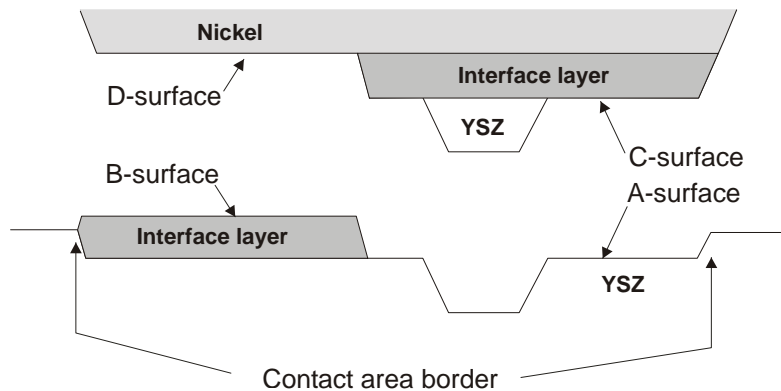


Fig. 3.25. Schematic drawing of the A-, B-, C- and D-surfaces and the interface layer in both the YSZ and nickel contact areas.

3.2.2.3 Cathodically polarised samples

The structures found on cathodically polarised samples partly resemble the structures found at OCV with visible grain boundaries and a hill and valley structure, but additionally areas with a granulated structure were found (fig. 3.26). AFM showed that the topography of this structure is varying (fig. 3.27) from 130 nm below to 80 nm above the YSZ surface. A rim ridge, 10-60 nm high, surrounds the areas with the hill and valley structure. The nickel wires show areas corresponding to both types of structures. The rim ridges are coincident with the circumference of the nickel contact areas. One of the three samples (241c) shows a fracture covering half the contact area. All samples showed ripped out YSZ grains.

3.3 Thermally annealed sample

Sample 151, which was thermally annealed for 3 weeks at 1200°C, shows a roughening of the YSZ surface with formation of different structures in different grains. AFM of the sample shows

a hill and valley structure with amplitudes up to 30 nm. Fig 3.28 shows an SEM image of the structures and fig. 3.29 shows an AFM image of two grains with different structures. These figures illustrate the differences in surface structure between grains, as one of the grains show a pyramid structure and the others show a step-like structure. Fig. 3.30 shows a line profile of four grains with different surface morphologies and here the variations in topography are obvious. The grain boundaries show grooves and shoulders (fig. 3.30).

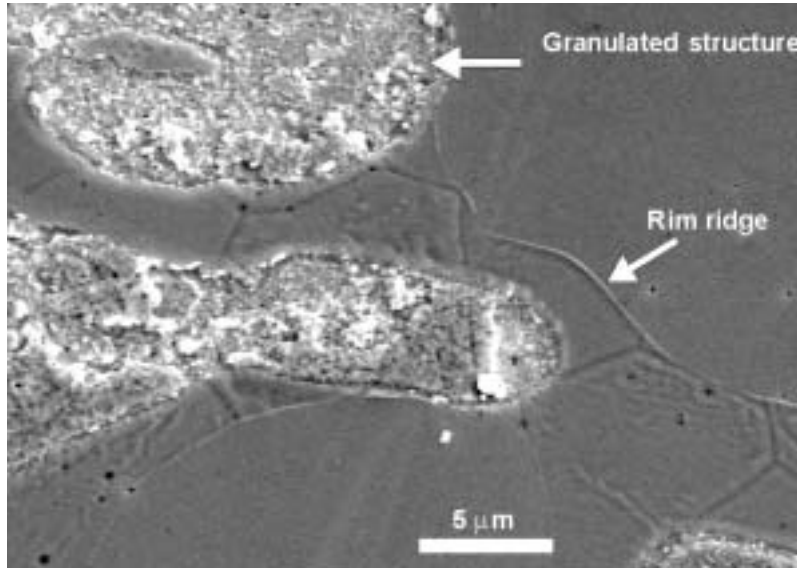


Fig. 3.26. SEM image of the structures on a cathodically polarised sample (241c). Both the granulated structure and the hill and valley type structure with a rim ridge are seen.

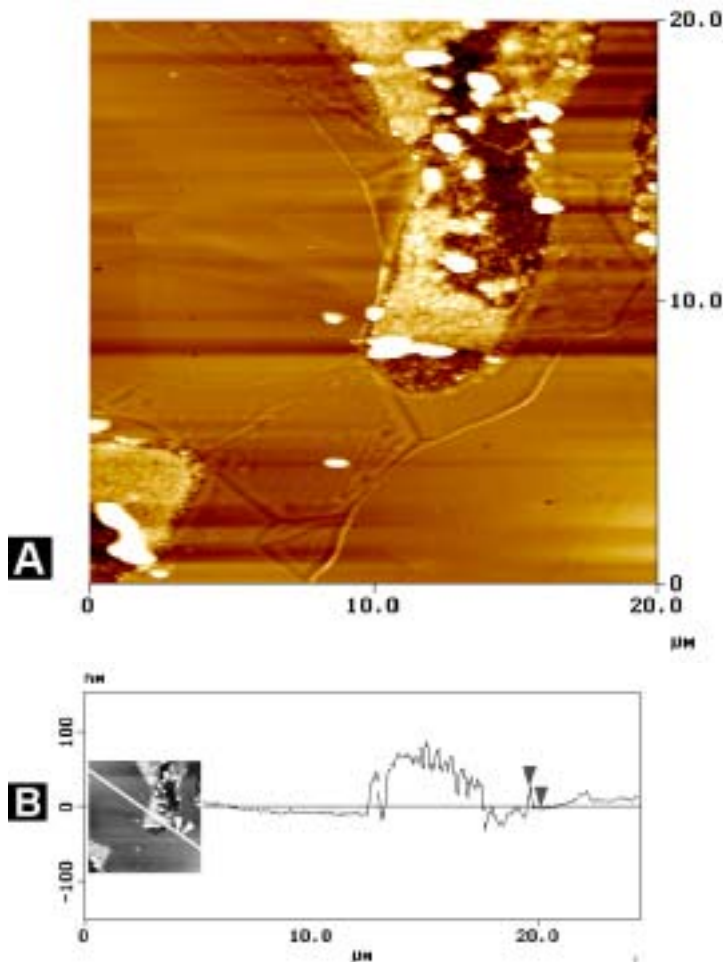


Fig. 3.27. A) 2D-AFM image of the sample 241c. Light areas are high and dark areas are low. Notice the two different types of structures. The granulated structure contains areas both higher and lower than the surrounding YSZ. The granulated area shows some very high points, which disturb the AFM and causes the horizontal stripes.

B) The line profile shows a height of the rim ridge of 28 nm. The profile cuts through an area where the granulated structure is relatively high.

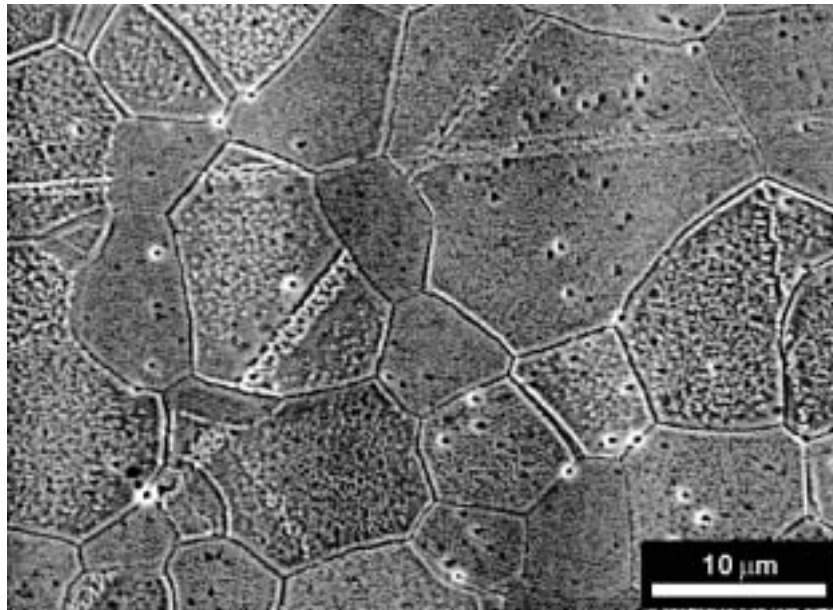


Fig. 3.28. SEM image of the YSZ surface structures after thermal annealing of sample 151. The grains show different surface morphologies. The grain boundaries have developed grooves and shoulders. Scratches after the polishing are recognised. During thermal annealing they become broader and more visible. The sample was annealed at 1200°C for 500 hours in air.

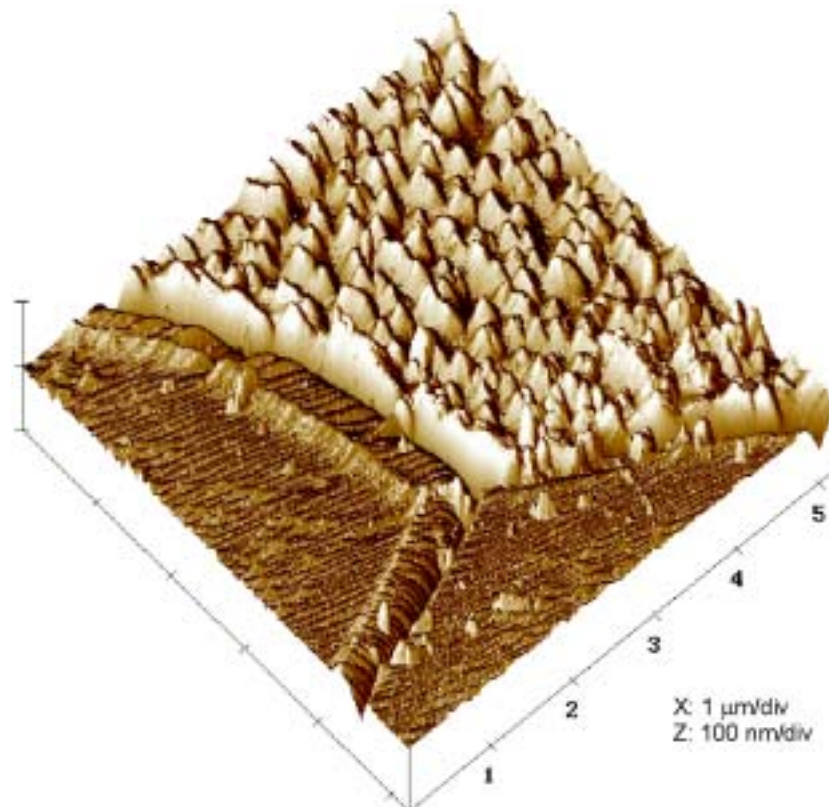


Fig. 3.29. AFM image of the thermally annealed sample 151. Three grains are seen in the image. One of them has a pyramid morphology whereas the two others show a step-like morphology. Grain boundary grooves and shoulders are seen.

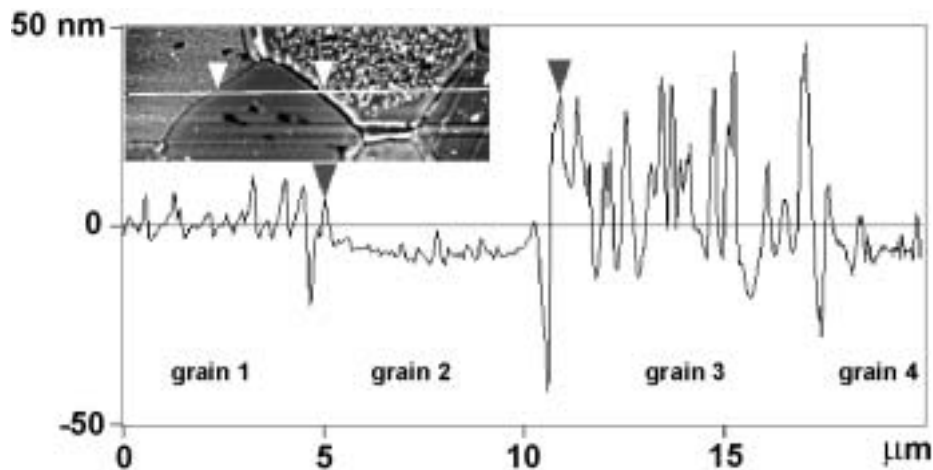


Fig. 3.30. Line profile showing the topography of four grains with different surface roughness on the thermally annealed sample (151). The arrows mark two of the grain boundaries.

3.4 Discussion on morphology

Three-dimensional structures in an interface are rarely easy to examine but in this case, as the nickel and YSZ can be separated after experiments, it was possible to map the topography of the two resulting surfaces.

3.4.1 Thermal annealing of YSZ

The morphology of the polished YSZ surfaces does not change noticeably after 7-10 days at 1000°C. During thermal annealing for 3 weeks at an elevated temperature of 1200°C, however, the YSZ grains developed a hill and valley structure.

Thermodynamically unstable surfaces attempt to reduce their surface free energy by decomposing into facets. This is well known from metals, as for example nickel (fig. 3.12), which during heat treatment develops terrace-like structures. The terraces consist of large low energy facets and small high-energy facets. This is energetically more favourable than a wide variety of facets of different energies [21]. Ceramic materials also try to decrease their surface energies by developing facets. This was shown [22] for an alumina (10 $\bar{1}0$) surface annealed at 1400°C. Grain surfaces very close to the equilibrium shape develop a terrace-and-step structure and surfaces deviating more develop hill and valley structures [23].

De Souza and Kilner [24] show an AFM image of thermally annealed strontium-doped lanthanum manganite. The grains show a well developed hill and valley structure and the grain boundaries show grooves and shoulders similar to the thermally annealed YSZ grain boundaries.

During thermal annealing, YSZ changes its surface morphology in the process of lowering its surface energy. The surface decomposes into two or more planar surfaces and, depending on the crystallographic orientation, different structures result.

3.4.2 Impurity influence on the formation of hill and valley structures

The comparison of thermally annealed YSZ with YSZ in contact with pure nickel shows that the YSZ/pure Ni develops the hill and valley structure much faster than the YSZ alone. Combining YSZ with the impure nickel accelerates the development of the hill and valley structure further, creating topographically higher structures, which are completely overriding the pattern of grain boundaries and the individual grain structures.

The formation sequence for the hill and valley structure in contact areas on samples with impure nickel electrodes is believed to start with a development of the groove-peak-groove grain boundaries and the hole structure. The holes develop into valleys, and at first this structure is ordered and grain boundaries are characteristic. Eventually, the hills become more massive, the grain boundaries disappear, and the morphology becomes more uniformly “chaotic” through out the contact area. Local pressure and contact time may play a role in the evolution of the different stages.

The grain boundary morphology in the YSZ contact area is different when the two types of nickel wire are used. The pure wires produce grain boundaries with the normal geometry of thermally annealed grain boundaries: grooves and shoulders. The impure wires produce grain boundaries enriched in material with a peak where normally the groove is expected. The main constituent of the grain boundary phase is believed to be an impurity phase.

The hill and valley structure develops in the (harder) YSZ, which is then shaping the softer nickel ($1000\text{ }^{\circ}\text{C}$ is $0.7 T_{\text{melting point}}$ for nickel whereas it is $0.4 T_{\text{melting point}}$ for YSZ). In the nickel, imprints of the hill and valley structure and the grain boundaries of the $5\text{-}10\text{ }\mu\text{m}$ YSZ grains are seen.

A closer investigation of the hill and valley structure on both thermally annealed YSZ and YSZ contact areas on samples with impure and pure nickel wires reveals that the hills consist of pyramidal tips, which are aligned and have similar orientations. The pyramids are believed to be a representation of the preferred facets developed by the YSZ.

During polishing the upper layers of a crystalline surface are changed/deformed and in order to examine if the resulting amorphous/deformed layer might be involved in the development of the structures by recrystallisation, pre-annealed samples were examined. The pre-annealed samples developed the hill and valley structures, which imply that the cause of the formation is not the recrystallisation of the surface layer. Neither is the cubic to tetragonal transformation directly involved. This was confirmed by the 10 mol% YSZ single crystal, which has a stable cubic structure at 1000°C .

In the literature, it has been shown that processes such as etching and adsorption are known to be able to change the surface properties of both oxides and metals.

When the MgO (110) surface is etched with phosphoric and nitric acid, facets are generated in the $\langle 001 \rangle$ and $\langle 110 \rangle$ directions [25]. Different morphologies develop as a function of etching time, starting with ill-defined pits and a later development into elongated pyramids. Thermal annealing does not produce faceting within the authors' time limit (10 minutes at 1000°C). Differences in etch rates for differently coordinated surface atoms decide the resulting structure. Chan et al. [26] have examined the phenomenon of overlayer induced faceting. Some bcc metal overlayers can make the substrate fcc metal facet if certain surface/interface energy conditions are fulfilled. It may be energetically favourable to form facets in more than one direction (e.g. pyramids). First principles calculations confirm their results [26]. The balance between the lowering of the surface energy and the increase in surface area determines if the surface will facet.

Metal-ceramic interactions are rarely described in the literature. However, Ghetta and Chatain [27] performed experiments with liquid Cu or Cu-Ti droplets on a polished Al_2O_3 single crystal substrate. They found that after some time, the alumina surface develops facets depending on the metal composition, and that a ridge develops along the three phase boundary.

It is thus not unusual for surfaces in contact with other phases to restructure by faceting in order to lower their surface energy. It is believed that the impurity phase and/or the nickel present in the contact area promote the formation of the hill and valley structure and that the pyramids observed in the AFM images are representing facets.

3.4.3 The rim ridge

The contact area boundary with the rim ridge marks the area where a mechanical contact between the nickel and the YSZ has been. On samples with both impure and pure nickel wires internal ring-shaped rim ridges were found (fig. 3.10). Inside the ring no hills and valleys were seen. On the corresponding nickel wire a pore with the same geometry as the ring was seen,

confirming that the rim ridge is formed at three phase boundaries and that a direct contact between the wire and the YSZ is required for hill and valley formation.

The rim ridge is always well developed when using impure nickel wires and very thin when the pure nickel is used. The dimensions of the ridge are thus dependent upon the amount of impurities present in the nickel.

The formation of the rim ridge is discussed in chapter 4.

3.4.4 Bonding between Ni and YSZ

The elliptical fractures found in the YSZ are observed on all samples with impure nickel electrodes, including samples with lower average pressure than the pressures than the pure nickel wires have been subjected to. Fractures were not observed on non-polarised samples with pure nickel electrodes. This implies that the bonding does not happen between the YSZ and nickel but that another phase acts as a bonding medium. The impurity phase present in the interfacial region may act as such a medium.

Two of the anodically and one of the cathodically polarised samples showed a fracture and single YSZ grains were in many places ripped out. Even for the anodically polarised samples, which developed a completely new structure, ripped out grains were seen. It is believed that the fractures on polarised samples with pure electrodes mainly are due to bonding caused by current-induced changes in the interface.

3.4.5 Influence of current

The structure development in the impure contact areas was apparently not affected by current passing through the interface. The structure development in the pure contact areas, however, was clearly current dependent. The structure on anodically polarised samples differs from structures on both non-polarised and cathodically polarised samples. On anodically polarised samples, an interface layer with a thickness of up to more than 1 μm exists at the Ni-YSZ interface, causing a separation of Ni and YSZ to occur at different levels. A complete reorganisation of the interface region is taking place, changing the dense YSZ into a structure consisting of nano-sized particles. As this only happens during polarisation it is reasonable to suggest that electromigration is the responsible mechanism. Electromigration is the process of mass transport driven by an externally applied electrical force and is commonly found in metal/semiconductor systems [28].

Nickel is abundant in the interface layer, especially as rounded particles, which suggest a gas phase transport mechanism. During anodic polarisation, water is produced at the three phase boundary zone. This could result in local oxygen partial pressures where Ni could be hydroxylated and transported through the gas phase as $\text{Ni}(\text{OH})_2$ into the YSZ interface layer. This is a mechanism already described by Aaberg et al. [29] but they observed nickel particles, as did Primdahl [7], along the contact area boundary.

Cathodically polarised samples with pure electrodes show two different types of structures, the granulated type and the hill and valley type structure. Processes causing bonding of the YSZ to the Ni are active as YSZ is found on the nickel side of the contact area. The occurrence of YSZ is only seen in the areas corresponding to the granulated areas. A difference in either current density or local pressure may be responsible for the two different structures.

It is probable that the same current effects are active in the contact areas of polarised, impure samples but that the impurity phase interferes with the effect of current. Perhaps longer polarisation periods may change the appearance of the structures in the impure contacts.

3.5 Conclusion on morphology

It may be concluded that:

- The Ni-YSZ interface is not stable at 1000°C in a wet hydrogen atmosphere.
- The YSZ develops a hill and valley structure in the contact area.
- The nickel and especially the impurity phase promote the development of the hill and valley structure.
- The hill and valley structure depends on the crystallographic orientation of the YSZ grains. The observed pyramid tips represents low energy facets in the YSZ.
- Imprints of the YSZ structures are formed in the nickel contact area.
- On the boundary between YSZ, nickel and the hydrogen atmosphere, impurities accumulate in a ridge. Its dimensions depend on the impurity content of the nickel.
- Current affects the structure development on samples with pure nickel wires.
- An approximately 0.5-1 μm thick interface layer develops on anodically polarised samples with pure nickel wires.

4 Impurities

Impurities may come from numerous sources. There are the impurities originally present in the Ni and YSZ, contamination during further processing, preparation and experiments. It is also possible to introduce impurities during the later analyses. Finally, adsorption on the surface of species present in the air is unavoidable.

Several techniques (EDS, XPS, TOFSIMS), each with specific advantages, were used to determine the chemical composition of the interface.

4.1 Impurities in YSZ

The chemical analysis of the YSZ powder from Tosoh Corporation includes impurities such as SiO_2 , Al_2O_3 , Fe_2O_3 and Na_2O (table 2.1). Impurities may be present because the cost of removing them is too high or they may be deliberately added to improve sintering [30, 31]. SiO_2 and Al_2O_3 are known to be sintering aids in zirconia [31, 2].

4.2 Results of XPS analysis of YSZ

Four reference samples (table 2.4) were examined to verify that the YSZ contributed with impurities and to evaluate the influence of the various treatments. One spectrum was obtained for each sample at each measurement depth. In the spectra, the heights of the element peaks were measured and the relative atomic percentages of the elements were calculated by incorporating an element specific sensitivity factor [32]. All peak heights were measured several times. The uncertainty is taken as the change that a measurement error of 0.5 mm causes in the final result. For less abundant elements with very low sensitivity factors (e.g. Si and C in some samples) the uncertainty is somewhat higher than for more abundant elements with higher sensitivity factors. Uncertainties for atomic ratios are found by calculating a 'worst case' from the uncertainties found for the atomic percentages.

The XPS studies (table 4.1) showed that besides Y and Zr and O, the following elements were found on the surface of the YSZ samples:

- carbon
- silicon
- sodium
- tin

Carbon was found in different quantities on the surfaces of all examined samples. The fresh fracture (sample 67) and two annealed samples (samples 62 and 63) showed a relatively low concentration whereas sample 61, which was not subjected to heat treatment, showed the highest concentration. Of the two annealed samples, the one annealed in air clearly and expectedly showed the lowest concentration of carbon. This is due to combustion of organic material at elevated temperatures in air.

Silicon was present on the surfaces of the samples that were subjected to heat treatment. The highest concentration was found on the sample, which was annealed in air (sample 62). Despite that the grinding and polishing partly take place with SiC paper, no trace of Si was found on sample 61, indicating that the SiC was not a contamination source.

A small amount of sodium was also found on all samples subjected to heat treatment and at the polished sample. The concentrations are so low that care should be taken when interpreting the data.

Tin was found on the surface of the sample, which was annealed in air (sample 62). Its presence was assigned to an earlier contamination of the furnace, and it only underlines the ease with which impurities may be introduced. This furnace was only used for this sample.

Table 4.1. The chemical composition of the sample surfaces in atom%. One spectrum was obtained for each sample. The uncertainties of the measured values are ± 0.2 atom% for O, Zr, Y, Sn, Na and the two highest values of carbon. For the rest of the carbon values and the Si values the maximum uncertainty is 1 atom%.

Sample Code	Treatment	O	C	Zr	Y	Na	Sn	Si
61	Polished, cleansed	27.4	59.5	10.5	1.7	0.8	0.0	0.0
62	Annealed 4 days, air. (1000°C)	52.8	15.9	18.0	4.3	0.3	0.7	7.9
63	Annealed 4 days, 9 % H ₂ . 1000°C	43.9	34.7	14.9	3.3	0.7	0.0	2.5
67	Fresh fracture	60.1	12.8	22.8	4.3	0.0	0.0	0.0

Table 4.2 shows relevant element ratios for the sample surfaces. The ratios for the fresh fracture (sample 67) are supposed to be closest to the expected values for bulk YSZ.

Calculating the theoretical values (for the 8 mol% YSZ) of the ratios give 0.174 for Y/Zr and 0.442 for Zr/O and 0.170 and 0.444 respectively for 7.82 mol% YSZ. From table 4.2 it is found that the fresh fracture (sample 67) does not match the ideal ratios. The Zr/O is too low and the Y/Zr is too high.

Table 4.2. Zr/O, Si/Zr, Y/Zr and Na/Zr ratios for all samples. The uncertainty is 0.02 for Zr/O, Y/Zr and Na/Zr. For Si/Zr the uncertainty is 0.05 (sample 62) and 0.04 (sample 63).

Sample code	Treatment	Zr/O	Si/Zr	Y/Zr	Na/Zr
61	Polished, cleansed	0.38	0.00	0.17	0.08
62	Annealed 4 days in air. (1000°C)	0.34	0.44	0.24	0.02
63	Annealed 4 days in 9 % H ₂ . (1000°C)	0.34	0.17	0.22	0.05
67	Fresh fracture	0.38	0.00	0.19	0.00
Tosoh	TZ-8Y powder, calculated values	0.44	0.00	0.17	0.00

Ion sputtering was used to remove some layers of atoms. After 5 minutes of sputtering (removing up to 35 Å) the Si/Zr for sample 62 was 0.08. After 10 minutes of sputtering no Si was detected on either of the samples 62 and 63. Equally, all the sodium had disappeared at this level.

4.3 Impure nickel electrodes

The 99.8% nickel contains many different elements (table 2.2). Only a typical analysis was provided from Johnson Matthey and so the actual composition of the impurity fraction is unknown. The EDS measurements after electropolishing showed no visible or detectable impurity particles on the surface, indicating that the impurities are dispersed evenly in the nickel.

The SEM images of the nickel wire outside the contact area after the experiments display multiple spherical, dark particles, up to 7-8 μm in diameter, situated in the grain boundaries of the nickel (fig. 4.1 and 3.12). The impurity particles are present everywhere on the nickel wire, including at distances of 1-2 cm from the contact area. Impurity bands with lengths of more than 100 μm , possibly formed by merged particles, are also observed (fig. 4.1 B). Small particles are seen in the kinks and corners of the Ni terraces. This is especially obvious in fig. 3.12. The dark particles are rich in Si and Al and contain Mg, Mn, Ti, Na and K (table 4.3).

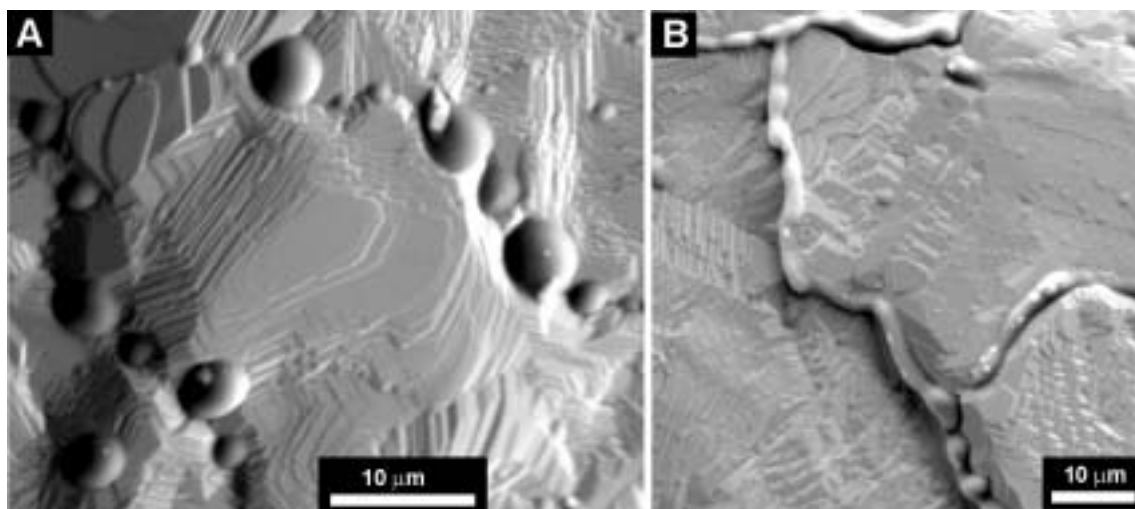


Fig. 4.1. The YSZ surface outside the contact area on an impure nickel wire after an experiment. A) The spherical impurity particles. B) Impurity particles merging into bands. The nickel terraces are the result of thermal annealing. Smaller bright particles may also be identified.

Smaller more edgy, bright particles are also seen on the nickel surface (fig. 3.12 and 4.1). They are often situated on the dark, spherical particles but they may also be located on the nickel terraces. The larger of them have a visible tabular habit. These particles are very rich in titanium and may contain some Mn.

Since the chemical analysis from Johnson Matthey did not state any Al, a minor experiment was performed to try to determine the source of Al. Nickel wires, which were annealed in a platinum crucible with no contact to alumina shows some aluminium (3-13 wt%) in the impurity particles. The nickel wires that were annealed in contact with alumina, as is the case in the real experiments, generally showed an aluminium content of 13-17 wt% in the impurity particles.

The SEM examinations of the nickel contact areas show imprints after impurity particles. Fig. 4.2 indicates that the imprints of impurity particles follow the pattern of the nickel grain boundaries with impurities outside the contact (fig. 4.2). The missing impurity particles are found on the YSZ part of the contact (section 4.3.1).

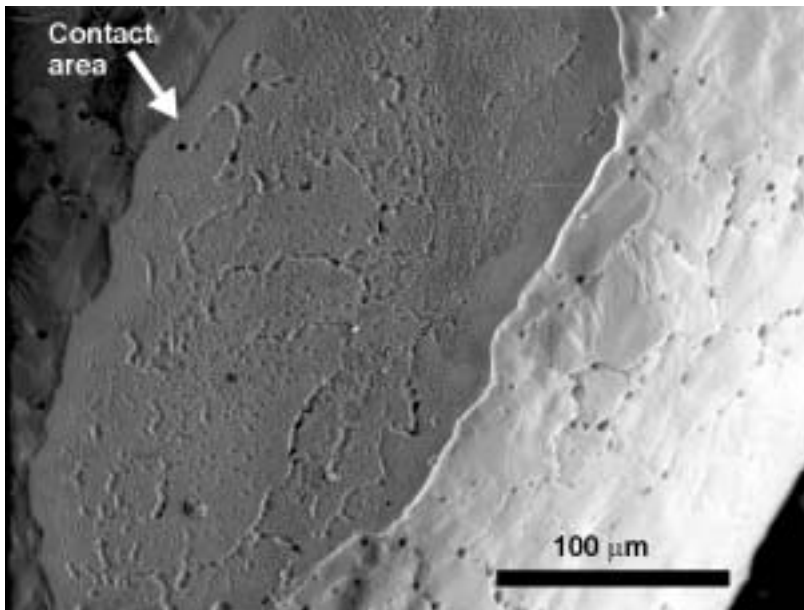


Fig. 4.2. Outside the contact area on the impure nickel wire, the dark impurity particles are located in the nickel grain boundaries. The same pattern but with imprints of particles are seen in the contact area.

Table 4.3. The chemical composition in wt% of impurities on the impure nickel wires after the experiments. Ni is left out of the calculation.

Elements	Dark particles Wt%
Si	59.3 ±5.2
Al	17.9 ±4.0
Na	9.6 ±3.5
Mn	5.8 ±2.1
K	3.9 ±0.7
Ti	2.2 ±1.2
Mg	1.3 ±1.3
Total	100.0

4.3.1 Contact areas on YSZ pellets

A very prominent feature within the contact area is the large impurity particles often found in bands (fig. 3.1, fig. 4.3). An EDS mapping of a large part of a contact area (sample 161a) reveals that the pattern of impurity particles is easily traced in the Si and Zr map. The impurities contain Si but not appreciable amounts of Zr (fig. 4.3). Fig. 4.4 shows two corresponding contact areas (Ni and YSZ) and a comparison shows that these impurity particles correspond to the above-mentioned imprints in the nickel part of the contact. Table 4.4 shows the chemical composition of the impurity particles measured by EDS. Local variations from particle to particle and from sample to sample account for the relatively large standard deviation for some elements.

The other very obvious impurity phenomenon is the rim ridge (fig. 3.7-3.9). The rim ridge is in most places a thin structure and EDS measurements are difficult to perform. Due to the dimensions, signal from the underlying YSZ is bound to show up in the spectra thus making it difficult to determine if the ridge contains yttrium and/or zirconium. The average composition without the Y, O, Ni and Zr is seen in table 4.4. An EDS mapping of a part of the rim ridge (161a) indicates that Si is present but that Zr is not very abundant.

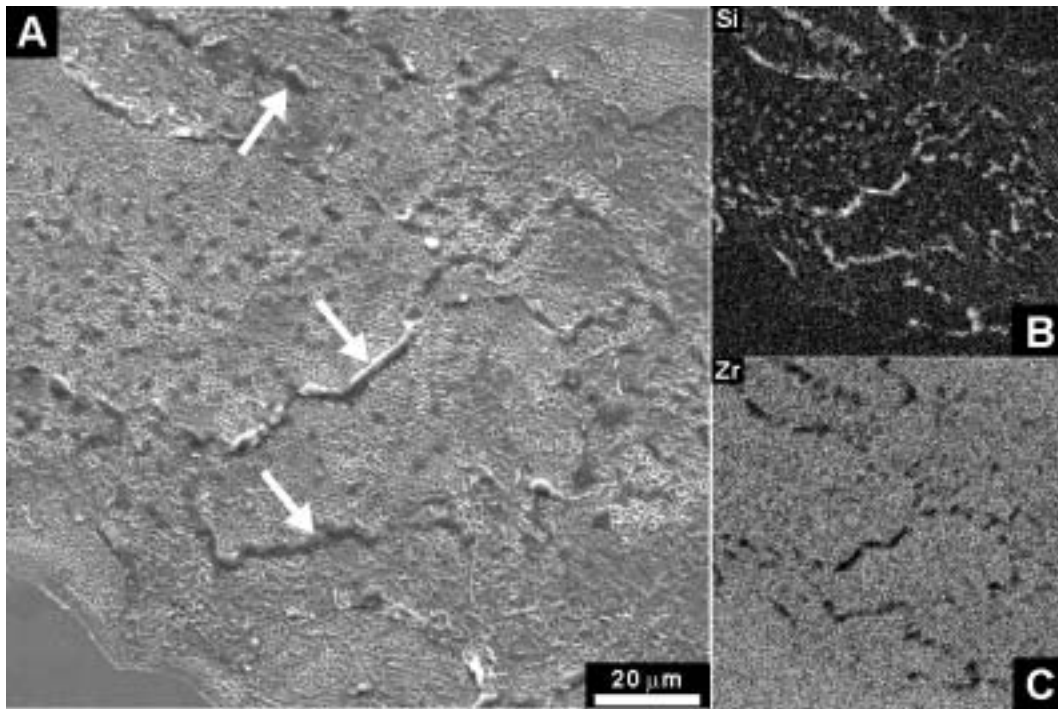


Fig 4.3. A) Impurity particles and bands (arrows) on the YSZ contact area of sample 161a. B) EDS map of Si. C) EDS map of Zr. The pattern of impurity particles is easily traced in the Si and Zr maps. The impurities contain Si but not appreciable amounts of Zr.

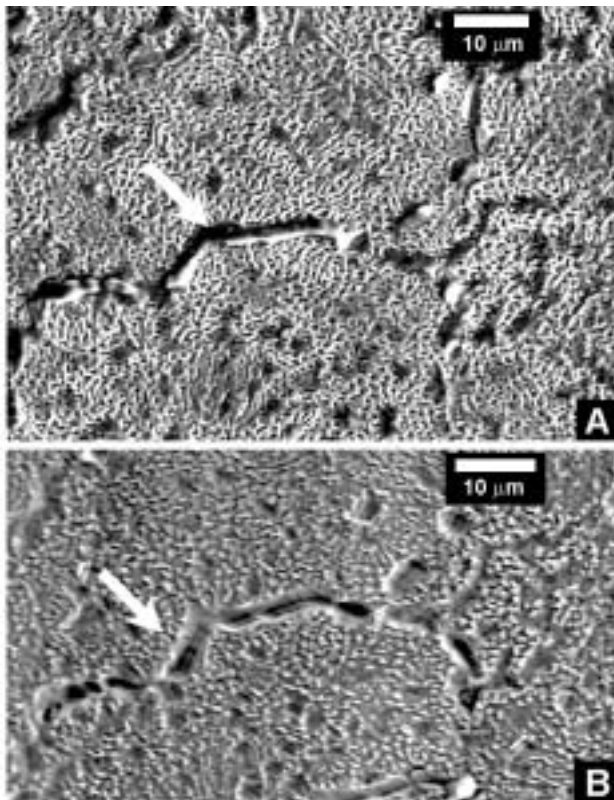


Fig. 4.4. A sub-area of the contact areas on A) the YSZ three-electrode pellet and B) the impure nickel wire (sample 161a). The hill and valley structure and impurity particles and bands are seen. The white arrows mark corresponding points. It is possible to correlate particles on the YSZ (image A) with imprints of particles in the nickel (image B). Image A has been mirrored and rotated to make correlations easier.

A weak signal from Ti indicates that the YSZ grain boundaries in the contact area probably are enriched in impurities. The grain boundaries are too thin to analyse properly with EDS.

The EDS measurements of the YSZ in the bottom of the fracture and in the area outside the contact area only shows Y, Zr and O (opposite the XPS and TOF-SIMS measurements in the sections 4.2 and 4.5).

Nickel is not abundant within the contact area, but single particles are sometimes seen; their size is in the nanometer range.

Table 4.4. The average composition of the rim ridge and the impurities at the interface. Y, Zr, O and Ni are left out of the calculations. The standard deviations are shown.

Elements	Impurities in the interface	Rim ridge on pellets
	Wt%	Wt%
Si	71.8 ± 11.0	63.6 ± 6.3
Al	5.5 ± 3.7	14.2 ± 2.2
Na	2.8 ± 1.3	8.6 ± 2.6
Mn	11.5 ± 9.0	5.8 ± 3.8
K	1.6 ± 1.6	5.0 ± 0.9
Ti	5.9 ± 5.8	1.4 ± 0.4
Mg	0.9 ± 0.5	1.4 ± 1.4
Total	100.0	100.0

4.4 Pure nickel electrodes

The terrace structure is not very conspicuous on the pure wires and the surface generally appears smooth (fig. 4.5). The Ni grains are difficult to distinguish from each other. Stretching cracks are seen. They are more pronounced for the thick nickel wires than for the thin wires.

After the experiments only a few impurities are found on the nickel wires. In the contact areas light, spherical particles are occasionally seen (fig. 4.6). Outside the contact area, foreign particles are seen clinging to the wire (fig. 4.5 and 4.6); most likely they come from the furnace. Alumina particles and particles containing, Fe, Na, Si, Cl, K, Cr in addition to O and C have been found sitting on the wire. Impurities were not detected in the grain boundaries.

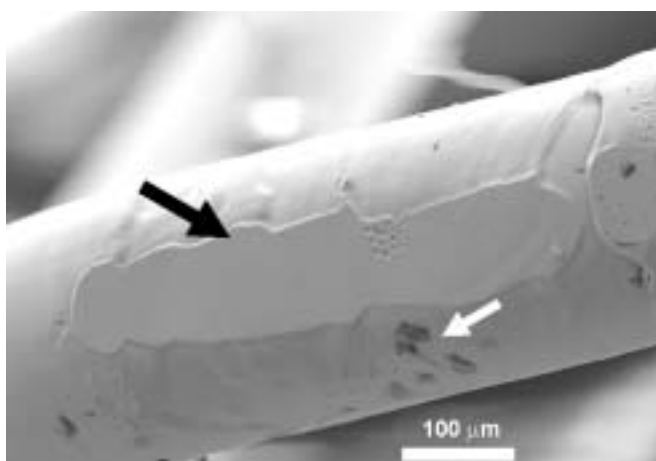


Fig. 4.5. The black arrow points at the contact area on a pure nickel wire. Impurity particles are seen sitting on the wire (white arrow) outside the contact area.

4.4.1 Contact areas on YSZ pellets

The contact areas appear very much cleaner with the pure nickel wire, but a few impurity particles are seen (fig. 3.15 and inset in fig. 3.17). The rim ridge is visible on non-polarised and cathodically polarised samples. The rim ridge is very thin and only on sample 233n was it reasonable to attempt an EDS measurement. 95 % of the signal originated from the YSZ. From the remaining 5 %, a composition of 38 % Si, 29% Al, 6% Na, 21% Ti, 5% K and 1% Ca was calculated. The composition of the impurities in the interface was also found and they contain roughly 30-50 % Si, 20-30 % Al, 4-16 % Na, 8-30 % Ca and possibly small amounts of Mn and Ti. Due to the very few measurements and the low concentrations, the above-mentioned percentages are not to be taken as anything else than a pointer to what the impurities contain. Measurements of the hill and valley structure yielded only Y and Zr. Dendritic KCl crystals were found outside the contact area on sample 133o (fig. 4.6).

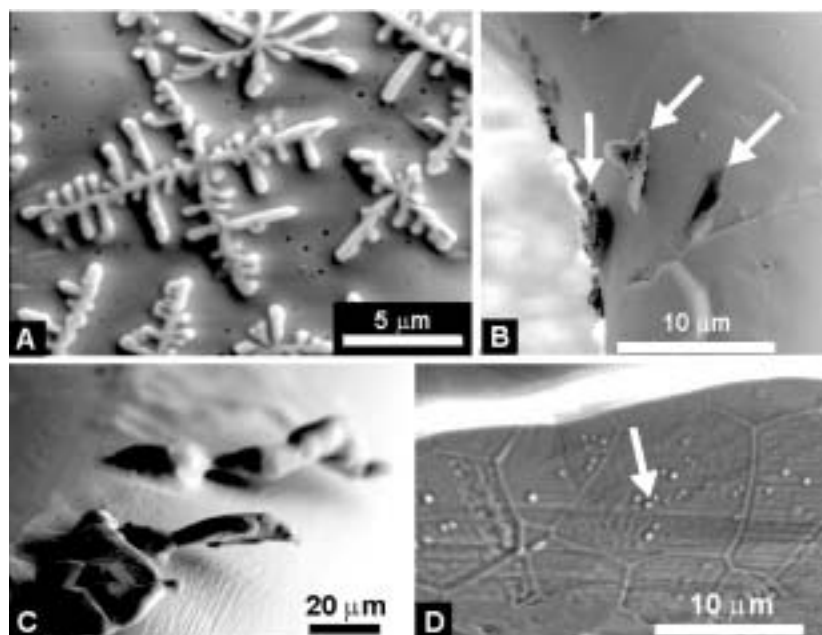


Fig. 4.6. Impurities on samples with pure nickel wires. A) Dendritic KCl crystals on the YSZ surface of sample 133n. B) and C) show impurities on pure nickel wires outside the contact area. D) Impurity particles (arrow) in a contact area on a pure nickel wire. Notice the imprints of the YSZ grains.

The anodically polarised samples with pure nickel electrodes developed an interface layer (section 3.2.2.2). The EDS analyses of the B-surface (the interface layer, fig. 3.26) show that the layer contains around 20 wt% Ni. Ni was also detected on the A-surface (fig. 3.26) preferentially as particles. EDS measurements of the interface layer sitting in the nickel contact area (C-surface) show a higher nickel content. This, perhaps, indicates that the underlying Ni contributes to the measurements. On surfaces where the interface layer has separated from the nickel wire (D-surface) some YSZ is still present. Table 4.5 summarises the chemical compositions of the different surfaces.

Table 4.5. EDS measurements in wt% of the interface layer on anodically polarised samples with pure nickel electrodes. The definition of the surfaces B, C and D is found in fig. 3.26.

Element	Surface B Wt%	Surface C Wt%	Surface D Wt%
Y	10.1 ± 2.1	7.2 ± 1.9	1.59 ± 0.01
Zr	69.3 ± 8.0	46.1 ± 7.0	12.16 ± 0.50
Ni	20.6 ± 9.7	46.7 ± 8.7	86.25 ± 0.42

Cathodically polarised samples showed to types of structures. Measurements in the YSZ contact area on both types of structures showed only Y and Zr. In the areas on the nickel wire corresponding to the granulated areas, Zr and Y were detected in concentrations up to 15 wt% and 2.5 wt%, respectively.

4.5 TOF-SIMS and XPS analyses

TOF-SIMS analyses were performed on two samples: one with an impure nickel wire (231n) and one with a pure nickel wire (232n). Both samples were non-polarised of the type 'not electrically connected' and measures were taken as not to contaminate the samples before and after the experiment. Optical images of both contact areas were obtained in the TOF-SIMS. The contact area on the sample with an impure nickel wire was easily recognised but the contact area on the sample with a pure nickel wire did not show up in the image. During analyses, however, the contact area on this sample was very conspicuous (fig. 4.7).

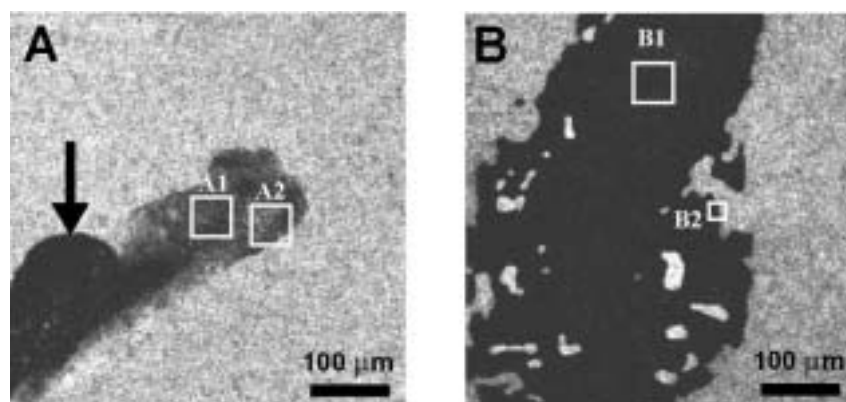


Fig. 4.7. The two analysed 500 by 500 μm areas. A) The analysed part of the contact area on the sample with an impure nickel wire (231n). The arrow marks the fracture. B) The analysed part of the contact area on the sample with a pure nickel wire (232n). Additionally, analyses of the framed areas (A1, A2, B1, B2) were performed.

The TOF-SIMS analyses provide information on the distribution of elements in the first monolayer of the surface both in and outside the contact area. Several scans were performed on the samples: a 500 by 500 μm scan of the contact area and the surrounding YSZ, a 50 by 50 μm scan of the interior of the contact areas (A1, B1) and the contact area border on the sample with an impure nickel wire (A2). The scan size of the contact area border on the sample with a pure nickel wire was reduced to 20 by 20 μm (B2). The contact areas on the two samples are 0.116 mm^2 (impure) and 0.188 mm^2 (pure). An ellipse shaped fracture (section 3.1) exists in the YSZ contact area on the sample with an impure nickel wire (fig. 4.7 arrow), and the corresponding piece of YSZ is found on the nickel wire. Contamination of the sample was found both as silicone and other organic compounds.

XPS measurements are, contrary to the TOF-SIMS analyses, quantitative. Both the two contact areas and areas far away from the contact areas were analysed with the XPS. It was possible to focus the XPS such that the contact areas could be analysed without contributions from the surrounding YSZ.

4.5.1 Overview scans

The elemental composition of two contact areas differs very much from the surrounding YSZ surface and from each other (fig. 4.8, 4.9 and 4.10). The 500 by 500 μm scan of the sample with an impure nickel wire clearly shows the presence of several elements both in and outside the

contact area. In fig. 4.8 the content of Mn, Y+Zr and Na is shown. Only the fracture, which has a depth of several microns, shows Y+Zr. The contact area contains Mn and Na, and Na is observed outside the contact area. The contact area on the sample with a pure nickel wire shows mainly Y+Zr, and again Na is found outside the contact area.

Fig. 4.9 and 4.10 show comparisons of the intensities of the elements present in the two areas. Fig. 4.9 concentrates on Ni, YSZ and the impurities originally present in the YSZ: Na, Si and Al. The main observations are that the Na, Si and Al are distributed principally outside the contact areas, but a weak signal arises from the contact areas as well. Nickel is present in the contact areas only. The YSZ intensities again show that no YSZ signal is coming from the contact area on the sample with an impure nickel wire, only in the fracture area is YSZ detected. In the contact area on the sample with a pure nickel wire, however, a strong YSZ signal is observed.

Fig. 4.10 shows the intensities of Mn, Ti, Mg, Ca and K. Mn and Ti are present in both contact areas. In the contact area on the sample with a pure nickel wire it is noted that Mn is distributed preferably in the outer 20-50 μm of the contact area. Ti is also present outside the contact area on the sample with an impure nickel wire. Ca is present both outside the contact areas and in the contact areas on both samples but the intensity from the sample with a pure nickel wire seems stronger than from the sample with an impure nickel wire. K is present outside the contact area on both samples and in the contact area on the sample with an impure nickel wire.

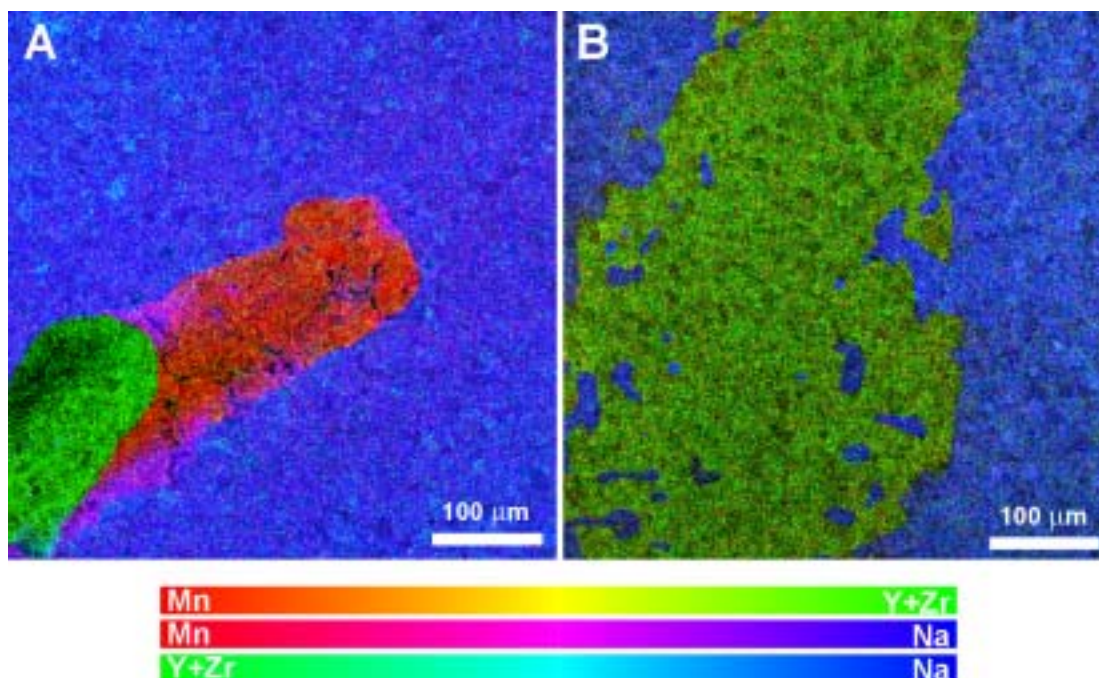


Fig. 4.8. 500 by 500 μm scans of A) the impure sample (231n) and B) the pure sample (232n) showing the distribution of the elements Mn (red), Na (blue) and Y+Zr (green). Intermediate colours show mixtures of two elements.

4.5.2 The contact area interior

A 50 μm by 50 μm area of the hill and valley structure including impurity particles on the sample with an impure nickel wire was analysed (fig. 4.11 A, B and C). From these images it is seen that some elements are not distributed evenly throughout the entire contact area but are more or less localised in oblong particles. The particles contain Mn, Si and Al, and are slightly enriched in Na and K. The underlying hill and valley structure seems to consist mostly of Y+Zr with some Ti, Al, Na, Si and Mn present. The Ni, which is present, is distributed in particles not coincident with the above-mentioned impurity particles.

Analyses of the contact area interior on the sample with a pure nickel wire are shown in fig. 4.11 D, E and F. The colour of the pure contact area in fig. 4.11 E and F indicates the presence of Ti and Al. No impurity particles were found in the analysed area. An examination of the intensity images (not shown) reveals signals from Ni, Mn Ti, K, Ca, Si and Mg.

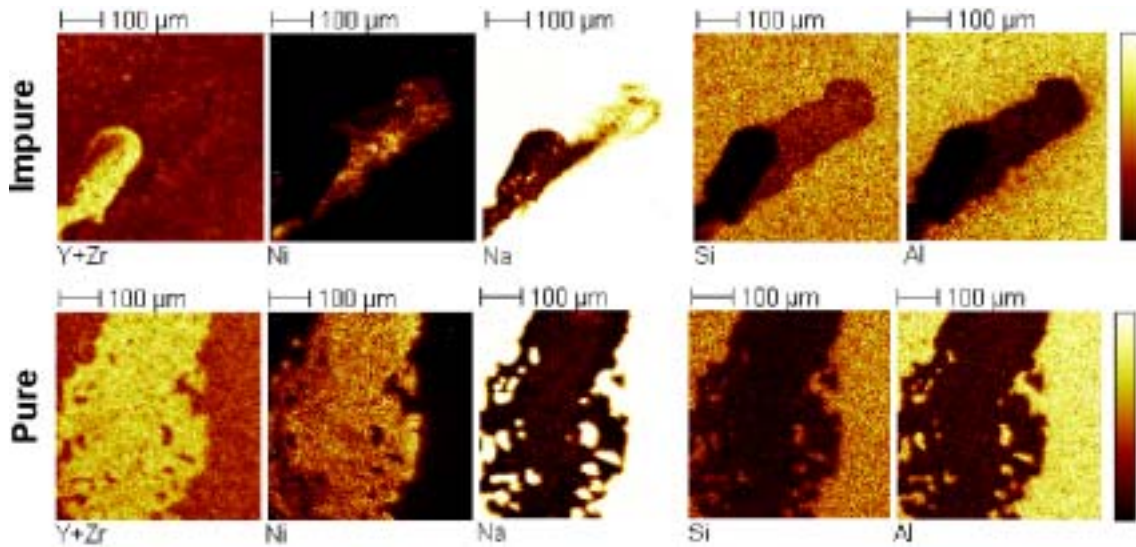


Fig. 4.9. Intensities of Y+Zr, Ni, Na, Si and Al from the sample with an impure nickel wire (upper row) and the sample with a pure nickel wire (lower row). White signifies a high intensity of the element and black signifies no signal from the element in question.

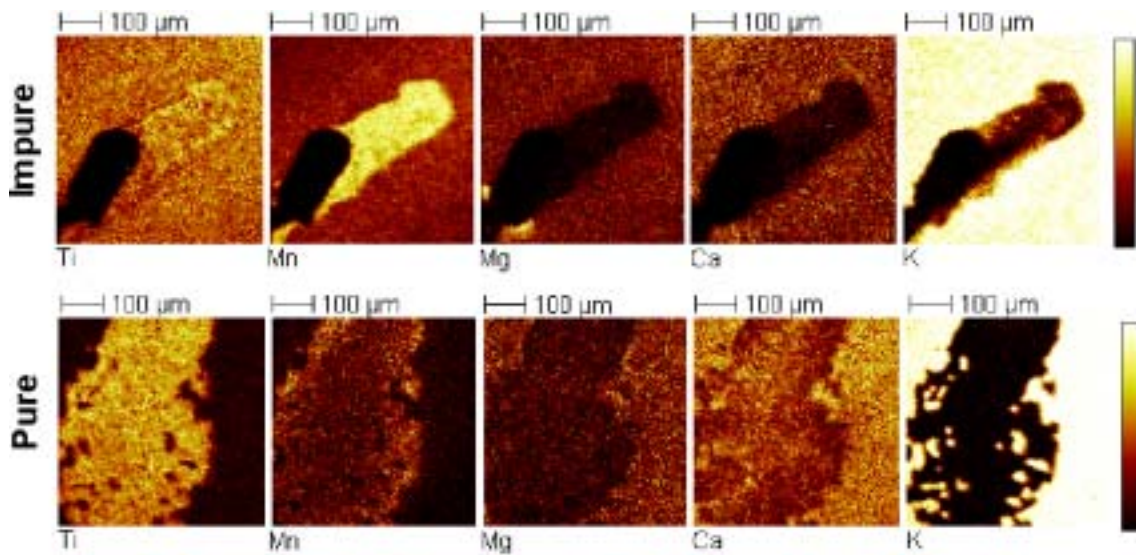


Fig. 4.10. Intensities of Ti, Mn, Mg, Ca and K signals from the sample with an impure nickel wire (upper row) and the sample with a pure nickel wire (lower row). White signifies a high intensity of the element and black signifies no signal from the element in question.

Colour coded images were produced for a sub-area the pure contact area and for a sub-area outside the contact area (fig. 4.12). In the contact area only a uniform colour (fig. 4.12 B) is seen whereas outside the contact area it is found that some grain surfaces are richer in e.g. Ca+Al+Na than others (fig. 4.12 D). In the total ion images (fig. 4.12 A and C) the YSZ grains can, due to different crystallographic orientations, be distinguished. Total ion images show the sum of all the detected ions.

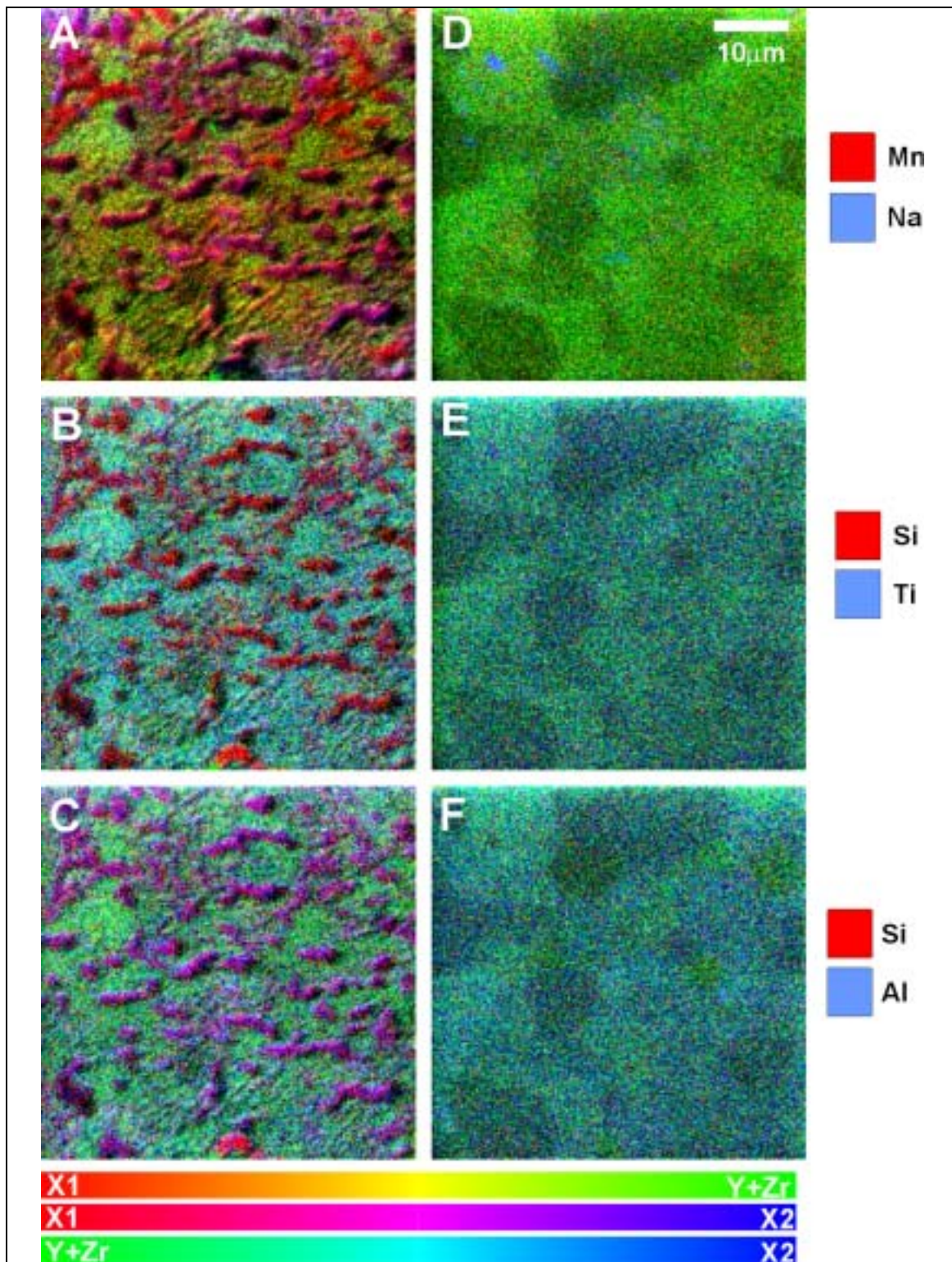


Fig. 4.11. A, B and C show the contact area on the sample with an impure nickel wire (A1 in fig. 4.7). D, E and F show the contact area on the sample with a pure nickel wire (B1 in fig. 4.7). The colour coding indicates the present mixtures of elements. In 4.11A and 4.11D X1 =Mn and X2=Na. In 4.11B and 4.11E X1=Si and X2= Ti. In 4.11C and 4.11F X1= Si and X2= Al.

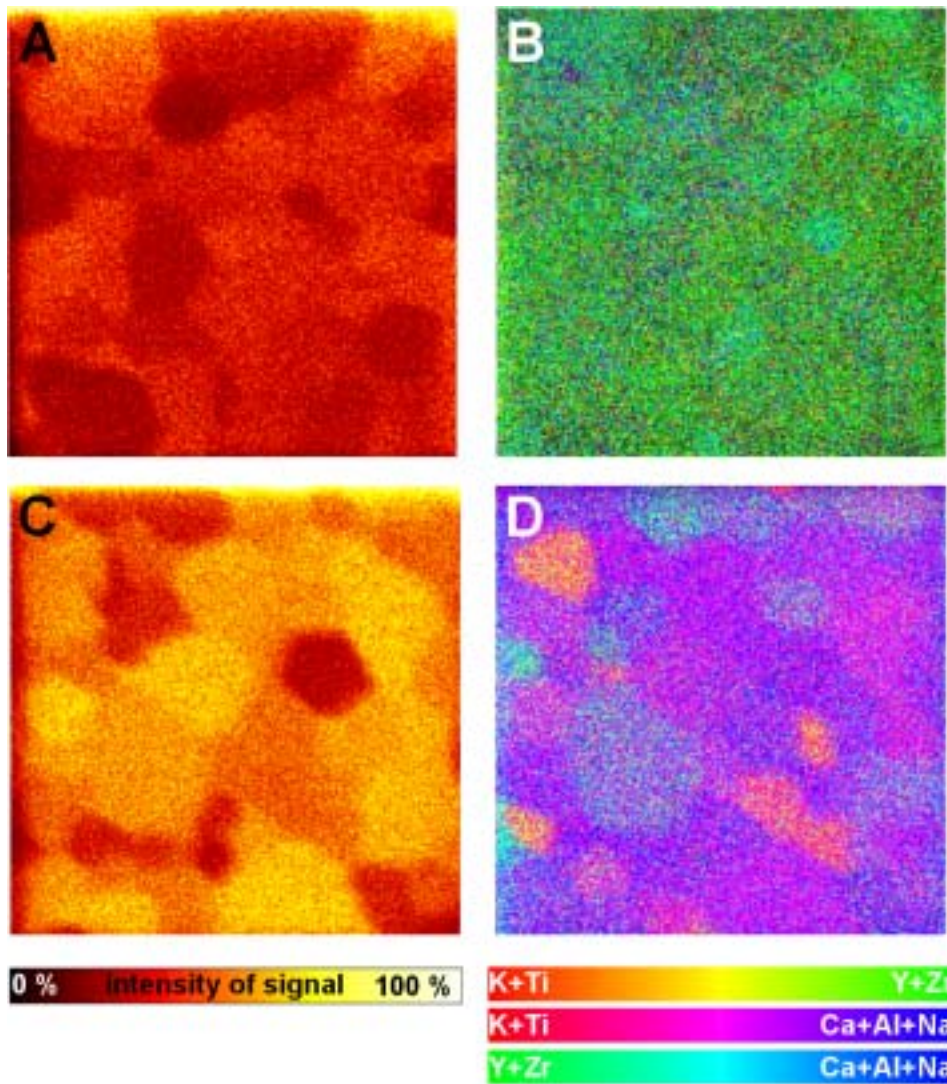


Fig. 4.12. A) and C) Total ion images of the contact area (B1 in fig. 4.7) and the YSZ surface outside the contact area, respectively, on sample 232n. The YSZ grains are seen in different colour due to crystallographic orientation. B) and D) Colour coded images showing the distribution of K+Ti, Y+Zr and Ca+Al+Na in the contact area (B) and outside the contact area (D). The clear difference in colour between fig. 4.12 B and D indicates different surface compositions. The distribution of elements in fig. 4.12 D is related to the pattern of YSZ grains outside the contact area, compare with fig. 4.12 A and C.

4.5.3 The contact area border

The contact area border was very well defined on both samples. The scans confirmed the already known distribution of elements. In fig. 4.13 three corresponding images are shown: A) is an SEM back-scatter electron image of an area on 213n. B) is an SEM image of the corresponding area on the nickel wire and finally, C) is a colour coded TOF-SIMS image of approximately the same area. It is possible to correlate structures in the three images. Impurity particles (dark) in A) are easily identified in 4.13 C) and their imprints are recognised in 4.13 B). In 4.13 C) it is found that Mn and Na are distributed all over the contact area, whereas only Na is seen outside the contact area border. The rim ridge is recognised in 4.13 A) and 4.13 C). In a few areas in 4.13 B) the green colour of Y+Zr is dominating. It was found that some impurity

particles had stayed on the nickel wire (framed area, fig. 4.13 B) and thereby left the YSZ surface exposed. The particles on the nickel wire were identified with SEM and EDS.

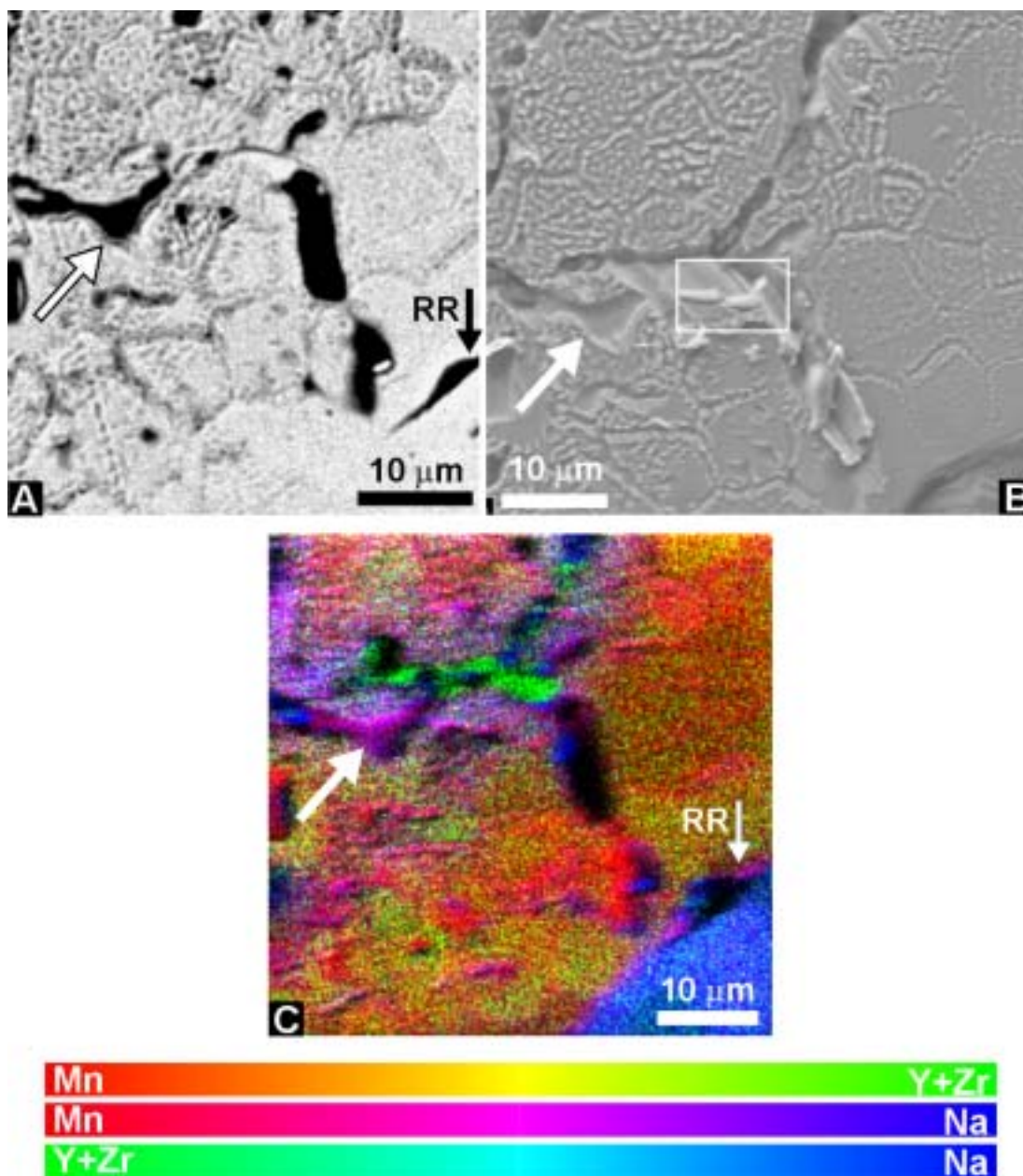


Fig. 4.13. A) SEM-BSE image of YSZ contact area. B) SEM image of the corresponding area on the nickel wire. C) TOF-SIMS image of the contact area border on sample 231n. Corresponding points in the three images are marked with arrows. The contact area border is easily distinguished. In the contact area Mn and Na is more dominating than the YSZ except for a few small areas. It was found that in these areas, the impurity particles stayed on the nickel wire (framed area in B). The rim ridge (RR) is recognised in A and C.

4.5.4 XPS analyses

Four areas were analysed: both contact areas (80-90 % of the entire contact area) and an area on each sample at a distance from the contact area. Table 4.6 shows the results in atom% when C, O, Zr and Y are subtracted. In the contact area on the sample with an impure nickel wire Si, Na,

Ti and Mn were detected. In the contact area on the sample with a pure nickel wire Si, Ti, Mn and Ni were detected. Outside the contact areas Si and Na were found.

By comparing the ratios of the impurity elements against Zr it is possible to see the relative difference between the different areas on the two samples (table 4.7). The Si/Zr ratio for the sample with impure nickel wire is 0.6 both in and outside the contact area. This is higher than for the sample with a pure nickel wire where the ratios are 0.2 in and 0.3 outside the contact area. The Na/Zr ratio outside the contact area was highest for the sample with an impure nickel wire. No Na was found in the contact area on the sample with a pure nickel wire. Mn was found in both contact areas, but the Mn/Zr ratio shows that the concentration is much higher in the contact area on the sample with an impure nickel wire. The TOF-SIMS analyses indicated Ti outside the contact area on the sample with an impure nickel wire, but the concentration was not high enough for the XPS to detect it. The Ti/Zr ratio in the contact area of this sample was much higher than in the contact area on the sample with a pure nickel wire.

As the analyses consisted of single measurements, a calculation of statistical uncertainties was not possible. Therefore, a number of alternative signal top integrations were performed to estimate the uncertainties related to the different element concentrations. Each top was re-integrated several times from different starting points, and the uncertainties were estimated from the observed variation in the quantification.

The uncertainties for the ratios in table 4.7 are based on worst case calculations with the values from table 4.6.

Table 4.6. XPS results for samples 231n (impure nickel wire) and 232n (pure nickel wire). Both the contact area and an area outside the contact area were analysed. The concentrations are in atom%.

Detected Elements	231n (impure)		232n (pure)	
	Contact area	Outside	Contact area	Outside
	Atom%	Atom%	Atom%	Atom%
Zr _{3d}	7.9 ±0.8	9.1 ±0.4	11.6 ±0.5	10.4 ±0.3
Y _{3p}	3.4 ±0.2	3.2 ±0.2	3.4 ±0.1	3.8 ±0.1
Si _{2p}	5.1 ±0.4	5.5 ±0.2	2.5 ±1.0	3.6 ±0.2
C _{1s}	22.0 ±1.0	19.5 ±1.2	30.3 ±1.5	23.3 ±1.1
O _{1s}	53.6 ±1.0	60.3 ±0.5	49.8 ±1.5	57.0 ±0.6
Na _{1s}	1.4 ±0.5	2.4 ±0.8	0.0	2.0 ±0.7
Ni _{2p}	0.0	0.0	1.3 ±0.4	0.0
Ti _{2p}	3.1 ±0.4	0.0	0.8 ±0.2	0.0
Mn _{2p}	3.6 ±0.5	0.0	0.4 ±0.2	0.0

Table 4.7. The element ratios for the samples 231n (impure nickel wire) and 232n (pure nickel wire).

Element ratios	231n (impure)		232n (pure)	
	Contact area	Outside	Contact area	Outside
Y/Zr	0.4 ± 0.14	0.4 ± 0.08	0.3 ± 0.04	0.4 ± 0.04
Si/Zr	0.6 ± 0.23	0.6 ± 0.10	0.2 ± 0.19	0.3 ± 0.06
Na/Zr	0.2 ± 0.16	0.3 ± 0.20	-	0.2 ± 0.15
Ti/Zr	0.4 ± 0.18	-	0.1 ± 0.14	-
Mn/Zr	0.5 ± 0.22	-	0.03 ± 0.07	-

4.6 Discussion on impurities

4.6.1 Impurity segregation in YSZ

Carbon is always found in high quantities on samples that have been subjected to air. The sample that was annealed in air show a lower concentration of carbon (16 atom%) than samples, which were not annealed (60 atom%). This is explained by combustion of the organic material in air at elevated temperatures. The sample that was annealed in hydrogen shows a higher carbon content (35 atom%) than the air-annealed sample, but still it was lower than the samples, which were not annealed. In hydrogen the carbon species do not combust but are converted to CH_4 , which is a slow process. The carbon on the fresh fracture sample (13 atom%) is representative for the airborne species settling immediately on the surface when the sample is exposed to air.

The silicon found on the annealed samples originates from the small amounts of impurities present in the TZ-8Y powder. During heat treatment, the Si segregates to the grain boundaries and external surfaces. This is well known from the literature [33, 34].

Sodium is also found to segregate from the bulk YSZ to surfaces. There is, however, also the possibility that some of the sodium may come from the environment.

Comparing the calculated and measured ratios of Y/Zr and Zr/O it is found that they differ. For the fractured YSZ surface, which should represent the pure YSZ, the Y/Zr ratio is 0.19 compared to the theoretical value, 0.17. This may be ascribed to preferential sputtering in the oxide [35] and may give an indication of the uncertainty of the method.

However, even with the fresh fracture as a reference it is seen that all annealed samples show a higher Y/Zr ratio, implying that Y segregates to the surface region during heat treatment. The low value of the Y/Zr ratio for the polished and cleansed sample can be explained by leaching of yttrium during the cleansing process.

Yttrium segregation is commonly observed to occur during sintering or annealing [30, 33, 34, 2]. By depleting the stabiliser, yttrium, from the YSZ the grains cannot stay cubic, and this may accelerate a reversion to the tetragonal form. Compared to cubic zirconia, tetragonal zirconia has a lower ion conductivity and a transformation into the tetragonal phase degrade the performance of the electrode/electrolyte [4].

No iron was detected at the surface of the YSZ by the XPS analyses despite the fact that iron is present in the bulk YSZ.

It has been found in single crystals of 10 mol% YSZ that during air annealing Fe segregates readily to external surfaces whereas in argon annealing no iron was detected [31].

In the literature many analyses of a segregated impurity phase in YSZ are found. The composition of the phase varies with temperature and length of heat treatment as well as with the annealing atmosphere. The yttrium silicate impurity phases found [31, 2, 34, 33] exist at temperatures as low as 800°C and are described as very mobile phases. They are glassy and some of them have a melting point below 1000°C [30].

4.6.2 Impurity segregation from the Ni to the interface

The impurities, which initially are present in the impure nickel wire, migrate to the nickel surface to lower the free energy of the system. On the nickel surface they are found as large, spherical particles sitting preferably in the grain boundaries, and also as smaller particles sitting in energetically favourable sites in the terrace steps and kinks (fig. 3.12). A comparison of the morphology of the impure Ni contact area (imprints of impurities) with the impurities in the Ni grain boundaries outside the contact area, leads to the conclusion that during the experiments the impurities, which have migrated to the nickel grain boundaries in contact with the YSZ, are transferred to the YSZ surface. The impurity phase obviously prefers contact with the YSZ compared to the nickel. The band-shaped impurity particles found on the YSZ thereby delineate nickel grain boundaries.

Considering the above-mentioned, it is not surprising that the chemical analyses of the impurity particles on the YSZ and on the nickel show that the two compositions are relatively close to

each other. A mixing with the impurities that are migrating out of the YSZ is likely to take place. The same phenomenon is likely to take place in the pure nickel/YSZ system.

4.6.2.1 Impurities in the impure interface

Si, Na, Ti, Mn

The EDS, TOF-SIMS and XPS analyses agree on the presence of Si, Na, Ti and Mn in the contact area (including impurity particles and the rim ridge). According to the EDS measurements, Ti is located in the impurity particles but the TOF-SIMS analyses indicate a more widespread occurrence both in the contact area and on the YSZ surface. The XPS did not find any Ti on the YSZ surface, indicating that Ti is only present in the upper few monolayers. The source of titanium is the impurities in the nickel wire.

Mn is only present in the contact area, distributed both into the impurity particles and over the entire contact area. Mn also originates from the nickel wire impurities.

The Si/Zr ratios in and outside the contact area are equal for the samples with an impure nickel wire. For the sample with a pure nickel wire, the ratio is clearly larger outside the contact area (0.4) than in the contact area (0.2). These differences show that the samples with impure nickel wires probably have received additional Si from the nickel. Impurity particles all over the Ni wire contain a relatively large amount of Si. The Si in the contact area is located preferably into the impurity particles but also as a thin film on the contact area surface.

The Na found outside the contact areas on both samples originates mainly from the YSZ. However, the Na/Zr ratios for the sample with an impure nickel wire indicate that another Na source may exist. Na is found in the impurity particles on the nickel wire.

Mg, Al, K

Both the EDS and the TOF-SIMS analyses detected Mg, Al and K on the samples with impure nickel wires. Aluminium is found both outside the contact, in the contact area, in impurity particles in the contact area and also in impurity particles on the nickel wire. The chemical analysis of the impure nickel does not state any Al but further tests have shown that some Al seem to be coming from the nickel. The impurities in the YSZ are probably the source for the Al distributed on the surface. Even though the aluminium seems to show up everywhere, the concentration is below the detection limit of the XPS.

Mg was also detected in the impurity particles and outside the contact area. The chemical analysis of the nickel provided by Johnson Matthey shows Mg.

K, on the other hand, is not an element found anywhere in the Ni-YSZ-system and it may, therefore, be supplied from the laboratory environment.

Ni, Ca

The distribution of nickel is shown in the TOF-SIMS images. The XPS measurements of the sample with an impure nickel did not reveal any nickel, confirming that only very small amounts of Ni is present in the contact. Ca is not mentioned as an impurity in the analysis of the impure nickel but is present outside the contact area.

4.6.2.2 Impurities in the pure interface

Si, Na, Ti, Mn

The EDS, XPS and TOF-SIMS detected Si, Na, Ti and Mn on the sample with a pure nickel wire. The main source of Si is the YSZ, but 1 ppm Si is present in the pure nickel so a small contribution from the nickel is possible.

The Na/Zr ratio is a little lower than for the sample with an impure nickel wire, indicating that the Na originates from the YSZ only.

Ti is not mentioned in the chemical analysis but shows up within the contact area of the sample with a pure nickel wire. The only known source of Ti is the impure nickel wire, which was placed a few centimetres away from the pure wire during the experiment. The Ti/Zr ratio is 4 times lower for the pure sample than for the impure sample.

Mn is not found in the chemical analysis of the nickel either but the XPS measures a Mn/Zr ratio of 0.03 in the contact area, which is 17 times lower than for the impure contact area. The sources of Mn and Ti are not known.

Al, K, Ca

The EDS and TOF-SIMS analyses showed Al, K and Ca on the sample with a pure nickel wire. Al is present in the nickel in ppm amounts, but the main source is probably the YSZ. Ca is an impurity in the pure nickel in amounts < 1 ppm.

K does not belong to the Ni-YSZ system according to the analyses. Cl is sometimes detected with the K and dendritic KCl crystals have been observed (fig. 4.6). In another study [36] KCl crystals were also observed on a single sample. The source of K or Cl has not been identified.

Mg, Ni, Cr

Mg, Ni and Cr were detected by the TOF-SIMS only. Cr is not present in the nickel analysis and as the XPS did not detect Cr, only very small amounts are present. Nickel was found in the contact area as opposed to the impure contact interface.

If the Mg comes from the impurities in the nickel wire it has migrated to the interface and further out on the YSZ surface.

4.6.3 Summary on the origin of impurities

The origin of most of the detected impurities can be explained by the initial impurity contents of the nickel and YSZ (Si, Na, Al, Mg for both samples; Ti and Mn for the impure sample; Ca for the pure sample). Experiments have shown that some of the Al present in the impurity particles (both in the interface and on the nickel wire) is likely to originate from the nickel wire. As the exact chemical composition of the nickel wire is not known, Ca may originate from the nickel as well. Some of the elements may be present in larger or smaller concentrations than stated in the analysis.

The content of K and Cl (both samples) and Cr, Ti and Mn (pure sample) are not accounted for by any analysis. This may be due to element concentrations, which are below the detection limit of the analyses from Johnson Matthey, or the elements may be supplied from the laboratory/testing environment. The presence of Ti and Mg outside the contact area indicates that impurities from the nickel migrate further than the contact interface.

Even though only ppm levels of impurities are present in the Ni and YSZ the impurities still can be detected at the YSZ surface and Ni-YSZ interface after the experiments.

The rim ridge and the impurities in the interface consist of an alkali silica impurity phase/glass phase, which originates from the impurities in the nickel and YSZ. The composition of the impurity phase may differ from sample to sample, as indicated by the relatively large standard deviations of e.g. Si and Mn in table 4.4.

The TOF-SIMS, which is the most sensitive analysis method, shows that a thin film of the impurity phase is present in the interfacial region on samples with both impure and pure nickel wires.

XPS studies of YSZ where Y-rich glassy silicate phases were found are abundant [30, 33, 34, 2] and it is thus likely that Y is a constituent of the impurity phase found in the present investigation. Both EDS (fig. 4.3) and TOF-SIMS (fig. 4.11 A) reject the presence of Zr in the impurity phase but it is difficult to determine.

4.6.4 Rim ridge formation

The differences in impurity content in the nickel wires are reflected in the dimensions of the rim ridge: a high impurity content in the nickel gives a high and wide rim ridge, whereas a low impurity content results in a thin and low ridge. Thus, the impurities from the nickel wire seem to end up in the rim ridge.

The formation of the rim ridge may take place by different mechanisms. One of the early suggestions was a mechanical push-up of the impurity phase in front of the nickel, as the contact area expanded. The finding of a rim ridge formed along the boundaries of a pore in the nickel wire (fig. 3.13) lead to rejection of this theory.

The present theory for the rim ridge formation involves a combination of diffusion and surface/interface energy driven migration. A more or less continuous film of the impurity phase is present on the YSZ surface as visualised in the data from the TOFSIMS analyses. From the shape of the rim ridge it is deduced that the interfacial impurity phase is sufficiently mobile to assume equilibrium shape.

The driving force for interface formation is the decrease in free energy, ΔG , when a common interface is established. The general equation for a liquid on a solid surface in equilibrium with a gas phase is per unit area:

$$\Delta G = \gamma^{LV} + \gamma^{SV} - \gamma^{SL}, \quad (4.1)$$

where the γ 's are interface energies between liquid (L) (or mobile phase), solid (S) and vapour (V) phases [21]. The Ni-YSZ-hydrogen-impurity phase(s) system is much more complicated than that, but the same principles apply.

The contact angle, θ , between the solid and liquid, specifies the condition for minimum surface energy:

$$\gamma^{LV} \cos \theta = \gamma^{SV} - \gamma^{SL}. \quad (4.2)$$

Spreading occurs when the substrate is completely wetted by the liquid phase and the contact angle is then 0° . As the contact angle increases, different degrees of wetting are observed, eventually ending with non-wetting for contact angles larger than 90° [21].

Interface and surface energies are dependent upon e.g. bonding type between the phases, chemical composition and defect chemistry of the interface/surfaces [37]. This study has revealed that the chemical composition of a Ni-YSZ interface depends very much on the impurities initially present. Furthermore, they modify the surface and interface properties.

Ranløv & Bilde-Sørensen [38] observed that when a homogeneous Ni layer on 13 wt% Y_2O_3 in ZrO_2 (~7.5 mol% YSZ) was heated to $1450^\circ C$ in a reducing atmosphere, the Ni formed small islands. It dewetted the YSZ, implying that γ^{Ni-YSZ} is relatively high. Information on the impurity content is not available but it is unlikely that this system was extremely pure.

The segregated impurities change the properties of the Ni-YSZ interface by lowering the interface energy. This change in surface energy of the YSZ results in the promotion of the hill and valley structure as described in chapter 3.

The chemical analyses indicate that the impurity phase in the interfacial region and at the three phase boundary originates from the impurities present in the nickel mixed with the impurities segregating out of the YSZ. The impurities in the nickel are well dispersed before the experiment. During heat treatment they diffuse to the grain boundaries and proceed to the nickel surface (fig. 4.14), where they are observed as large, spherical particles in the grain boundaries (fig. 3.12 and 4.1). The impurity phase (IP) is wetting the nickel and the contact angle has been estimated to be larger than 45° .

In the interface between Ni and YSZ, the impurity phase prefers forming an interface with the YSZ, therefore the impurity phase – YSZ interfacial energy, γ^{IP-YSZ} , is low. The impurity phase is close to spreading conditions and a contact angle close to zero is expected.

For impure nickel wires, bonding is observed in the central regions of the contact areas where the pressure is assumed to be high. In the surrounding areas the Ni separates from the substrate without deformation. This does not indicate a large degree of wetting and the interface energy between Ni and the interface impurity phase must be relatively high. Fig. 4.15 is a schematic drawing of the wetting behaviour of the different phases.

For non-polarised samples with pure nickel wires, bonding is not observed. For polarised samples with pure nickel electrodes the bonding is assumed to occur due to interfacial changes related to the passage of current.

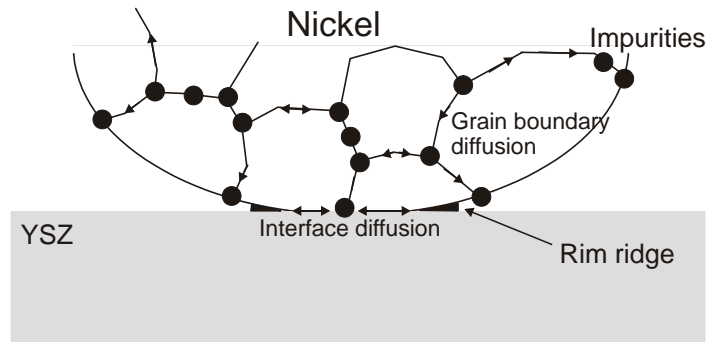


Fig. 4.14. Diffusion of impurities from the bulk nickel to the nickel surface, the Ni-YSZ interface and the three phase boundary.

The interface region is an area of fast diffusion, and migration of the impurities may cause them to end up at the three phase boundary. Here they are accumulated in the rim ridge due to surface and interface energy minimisation processes. The triangular cross sectional shape of the rim ridge is due to the shape of the cavity between the nickel and the YSZ, and the tendency to minimise the interface area towards the hydrogen atmosphere (fig. 4.15). By redistribution of the impurity phase, the total interface/surface energy of the system is lowered.

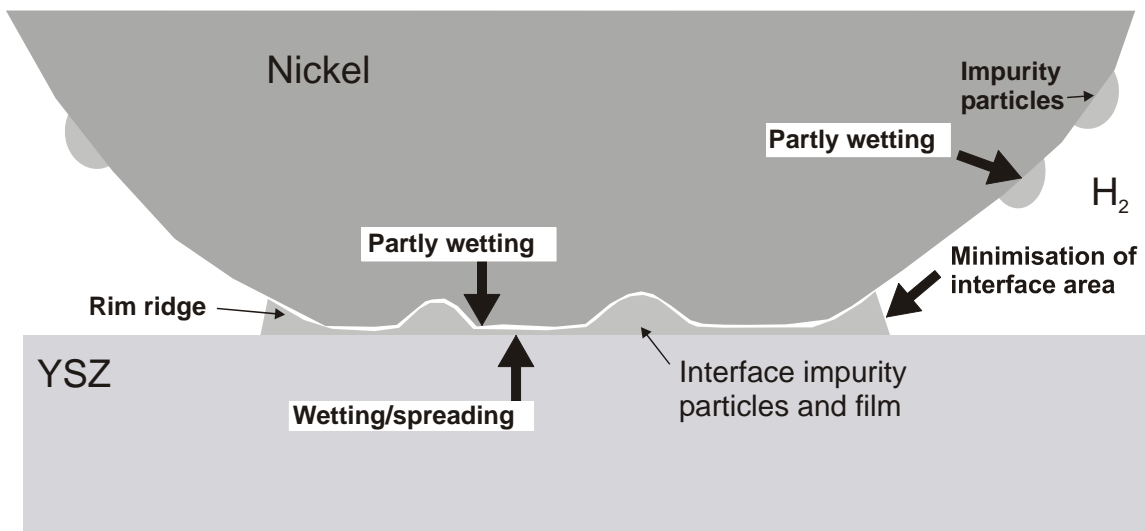


Fig. 4.15. The wetting relations in the Ni-YSZ/impurity phase/hydrogen system. The shape of the impurity particles sitting on the nickel wire indicates an intermediate degree of wetting. The impurity phase wets the YSZ. The surface area of the rim ridge against the hydrogen atmosphere is minimised as a part of the process of decreasing the total free energy of the system.

4.7 Conclusion on impurities

It may be concluded that:

- Impurities in the YSZ were found to have segregated to the YSZ surface during heat treatment. Yttrium enrichment was also found in the surface layer.
- The impurity particles and the rim ridge found at the Ni-YSZ interface originate partly from the YSZ but mostly from impurities in the nickel.
- The impurities present in the starting materials end up in the contact area and form a rim ridge at the three phase boundary even for very small amounts of impurities.
- The surrounding environment probably contributes with impurities.
- The impurity phase is an alkali silicate (glassy) phase, possibly containing yttrium.
- The rim ridge is formed by redistribution of the impurity phase in order to decrease the energy of the entire system.
- The impurity phase is more or less continuously distributed in the entire interfacial region.

5 Impedance Spectroscopy

The electrochemical characterisation was done by impedance spectroscopy. Impedance analyses were performed on samples subjected to OCV only, and to samples, which after a period at OCV were polarised either anodically or cathodically. After the polarisation period, the samples were subjected to OCV for a shorter period. In the following analysis of the impedance spectroscopy, the attention has been focused on the series resistance (R_s) and the electrode polarisation resistance (R_p) (fig. 5.1). From the series resistance the area of electrical contact can be calculated. The polarisation resistance reveals information on the electrode reactions, which are generally believed to occur at or near the three phase boundary zone between nickel, YSZ and hydrogen.

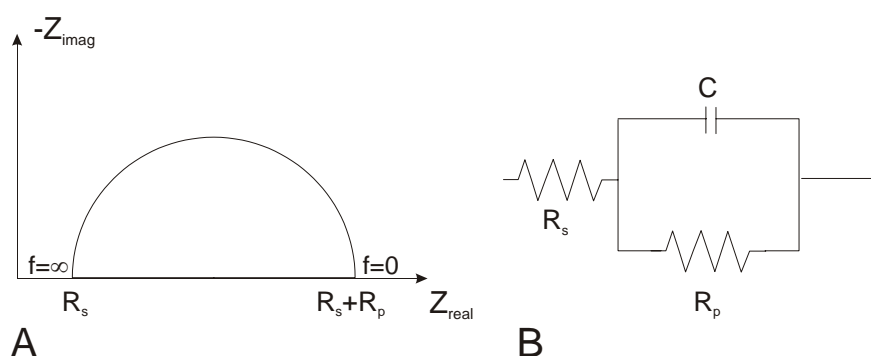


Fig. 5.1. A) Schematic impedance spectrum showing R_s and R_p . B) Equivalent circuit

The electrical behaviour of samples with impure and pure nickel wires are described separately, first with respect to the series resistance (section 5.1) and then with respect to the polarisation resistance (sections 5.2) and in section 5.7 the results are compared and discussed. The trends of the impedance spectra for samples with pure and impure electrodes are given in section 5.3, and in 5.4 some calculations of capacitances are performed. Sections 5.5 and 5.6 show a few results from the chronoamperometry and potential sweep measurements.

The results obtained with the pure nickel wires presented in this chapter are all based on the thick wires, except for one sample. The samples with the thin wires did not show satisfactory reproducibility. However, the majority of them showed resistances and microstructures, which were consistent with the results for the thick wires.

The task of plotting the impedance spectra, resistance plots etc. was simplified by a computer program, EasyPlot, which was developed by the author. The program was specifically designed for making the plotting routines as easy as possible. It was also used for extracting and calculating the time relations between the individual measurements. Appendix B shows the user interface of the program.

5.1 Series resistance

The series resistance is due to the ohmic losses in the electrolyte and the nickel electrode. It is found by reading the value in the impedance spectra where the high frequency end intercepts the real axis (Z_{real}) (fig. 5.1).

5.1.1 Impure nickel wires as electrodes

The figures 5.2-5.4 show plots of the series resistance versus time for comparable samples. It is seen that R_s tends to decrease toward a constant value, indicating that after 48-72 hours the contact areas have reached a final size. In table 5.1 the stable R_s values are presented. For samples subjected to OCV only, one value is shown. For samples subjected to a subsequent polarisation, both the stable value at OCV before polarisation and the stable value at polarisation are shown. For these samples, the average series resistance is $105 \Omega \pm 19 \Omega$ at OCV before polarisation and $115 \Omega \pm 16 \Omega$ at polarisation, i.e. there is an increase of the series resistance of up to 22%.

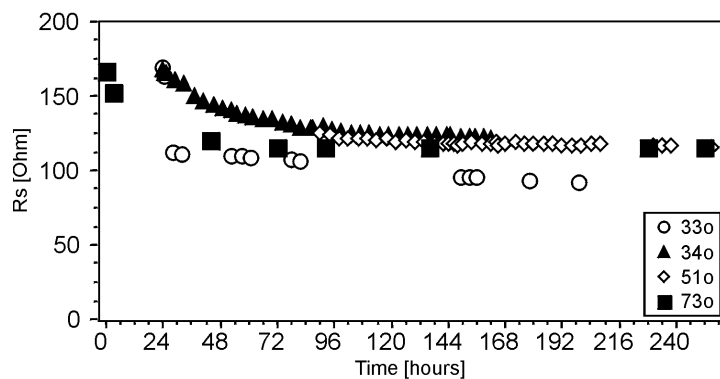


Fig. 5.2. R_s as a function of time for samples with impure nickel electrodes subjected to OCV. Zero time is when the temperature of the set-up reached 1000°C .

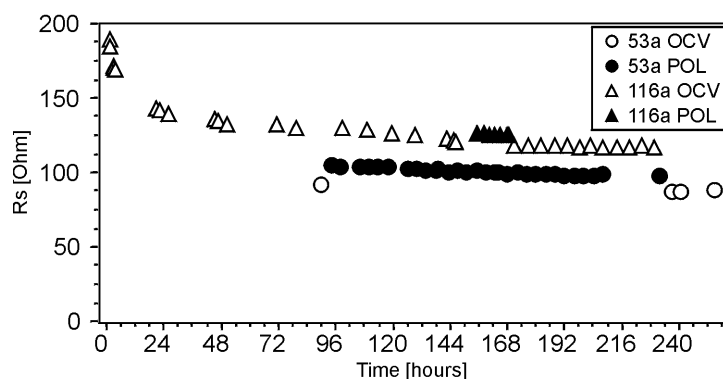


Fig. 5.3. R_s as a function of time for samples with impure nickel electrodes subjected to an anodic polarisation of 100 mV. The open and closed symbols indicate measurements at OCV and polarised (POL) conditions, respectively. Zero time is when the temperature of the set-up reached 1000°C .

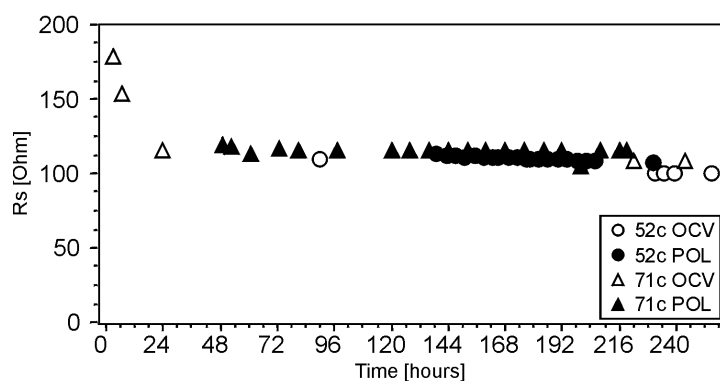


Fig. 5.4. R_s as a function of time for samples with impure nickel electrodes subjected to a cathodic polarisation of 100 mV. The open and closed symbols indicate measurements at OCV and polarised (POL) conditions, respectively. Zero time is when the temperature of the set-up reached 1000°C .

Table 5.1. Stable R_s values for samples with impure nickel wires as electrodes and 82 g load.
* indicates that the sample was pre-annealed. - indicates that data are not available.

Sample code	R_s (OCV) [Ω]	R_s (pol) [Ω]	Sample code	R_s (OCV) [Ω]	R_s (pol) [Ω]
22a	130	-	52c	100	109
53a	86	99	71c	108	115
111a	88	107	33o	92	-
112a	95	107	34o	122	-
161a*	117	124	51o	116	-
162a	141	146	73o*	116	-

5.1.1.1 Multiple polarisations

For two samples multiple polarisation experiments were performed. This was done during the same experiment: when 111a was anodically polarised, 112a was at OCV and vice versa. The figures 5.5 and 5.6 show the R_s -curves for the two samples. The polarisations applied did not alter the trends of the curves. The R_s shows the usual decreasing trend in both cases, intercepted by the periods during polarisation where the R_s -values are raised a few ohms.

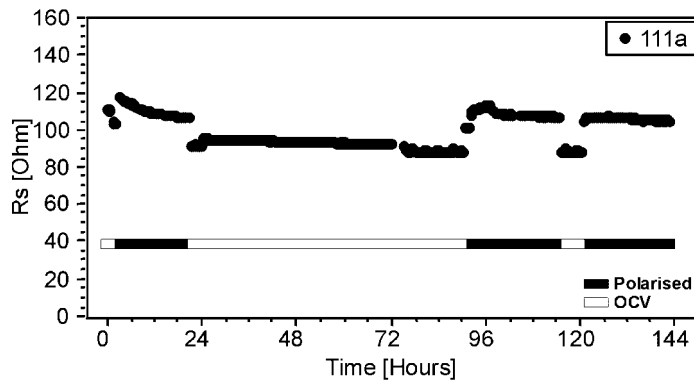


Fig. 5.5. R_s as a function of time for sample 111a. The bar indicates periods of anodic polarisation (100 mV) and OCV periods. Zero time is when the temperature of the set-up reached 1000°C.

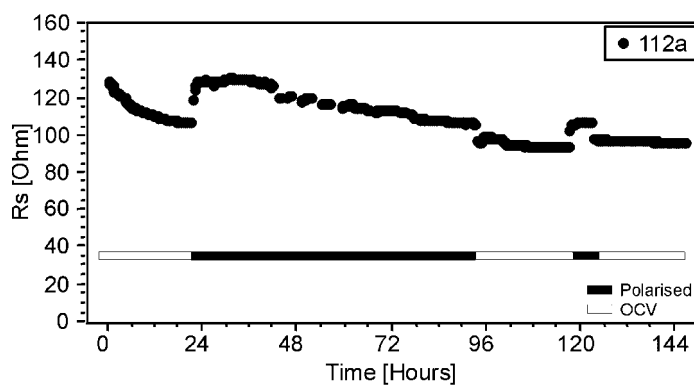


Fig. 5.6. R_s as a function of time for sample 112a. The bar indicates periods of anodic polarisation (100 mV) and OCV periods. Zero time is when the temperature of the set-up reached 1000°C.

5.1.2 Pure nickel wires as electrodes

The OCV conditions that the samples experience before polarisation are similar for all samples. The OCV data for pure electrodes mentioned in the following are taken from the pre-polarisation period of the anodically polarised samples.

The first few hours at OCV are characterised by a strongly decreasing R_s , eventually followed by a flattening of the curve after 24-48 hours (fig. 5.7 and 5.8). The R_s -values at OCV conditions range between 50 and 100 Ω (table 5.2), with the average R_s being 71 ± 17 at OCV. The values during polarisation (table 5.2) are up to 27 % higher, omitting sample 222a.

Table 5.2. Stable R_s values for samples with pure, thick nickel wires as electrodes and 82 g load. 222a shows a very high R_s during polarisation. This is ascribed to a change in the contact possibly when moving the leads from sample to sample.

Sample code	R_s (OCV) [Ω]	R_s (pol) [Ω]	Sample code	R_s (OCV) [Ω]	R_s (pol) [Ω]
212a	100	99	224a	60	76
213a	65	82	241c	86	88
221a	81	98	242c	61	63
222a	69	145	243c	49	54

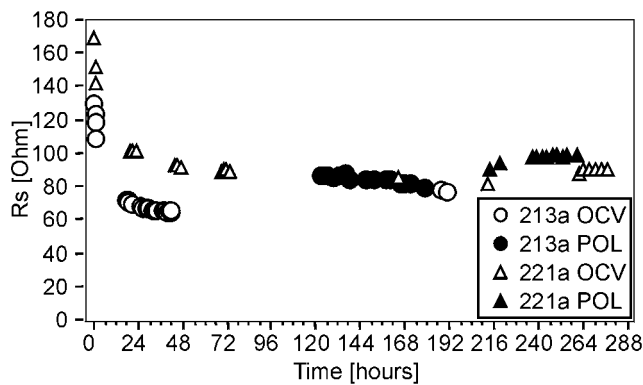


Fig. 5.7. R_s as a function of time for samples with pure nickel electrodes subjected to anodic polarisation at 100 mV. Zero time is when the temperature of the set-up reached 1000°C.

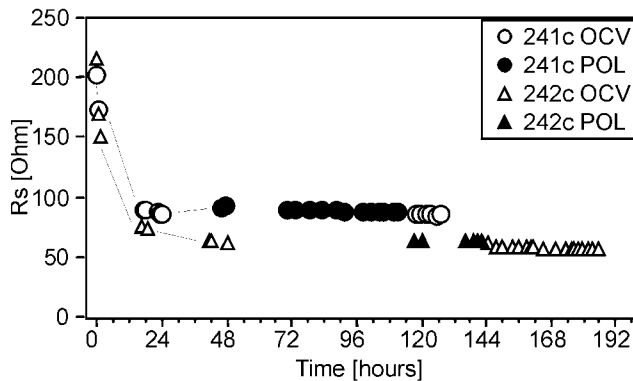


Fig. 5.8. R_s as a function of time for samples with pure nickel electrodes subjected to cathodic polarisation of 100 mV. Zero time is when the temperature of the set-up reached 1000°C.

5.1.3 Electrical contact areas

From the Newman equation [39] it is possible to correlate the series resistance (R_s) with the electrical contact area for a circular contact. Holm [40] added a shape factor f to account for elliptical contact areas (eq. 5.1):

$$R_s = \frac{1}{4\sigma r} f, \quad (5.1)$$

where σ is the conductivity of the electrolyte and r is the radius of the equivalent circular area. In the shape factor (eq. 5.2), γ is a measure of the ellipticity of the contact (measured in SEM images as the ratio between the lengths of the axes: $l_{\text{long}}/l_{\text{short}}$):

$$f = \frac{4}{\pi\gamma} \ln(2\gamma). \quad (5.2)$$

The literature does not agree on the ionic conductivity of 8 mol% yttria-stabilised zirconia. The conductivity of TZ-8Y tends to decrease with time and is in general dependent on the pre-history of the samples. Values ranging from 0.1-0.2 S/cm are reported [41, 42, 43, 4]) and thus a round number of 0.15 S/cm has been chosen.

Table 5.3 and 5.4 show the sizes of contact areas on samples with impure and pure electrodes, respectively, estimated from SEM micrographs (physical contact areas, $A_{\text{ellipse}} = \pi r_1 r_2$) and calculated from electrical data including deviations, both for polarised and open circuit voltage samples. A 10-15% uncertainty of the physical contact areas is estimated as the geometry of the areas is not always strictly elliptical and the fracture in places conceals the contact area boundary. The contact areas in the SEM micrographs are approximated to an ellipse of which the area is found. The electrical contact areas in table 5.3 and 5.4 are found (eq. 5.1 and 5.2) by using the individual aspect ratio of each contact area. Calculations of the uncertainty of the electrical areas have been performed. Assuming representative values for ellipse size and R_s and assuming an uncertainty for the axes of the ellipse of each $\pm 10 \mu\text{m}$, for R_s of $\pm 5 \Omega$ and that σ_{YSZ} is constant at 0.15 S/cm, the resulting standard deviation of the electrical area is $\pm 0.003 \text{ mm}^2$ for the impure electrodes.

For all samples (except 73o) the calculated electrical area is smaller than the measured area. Sample 73o is discussed in section 5.7.1.2.

Table 5.3. The measured (SEM) and electrical contact areas in mm^2 for impure electrodes. The last column shows the deviations of the electrical areas from the SEM areas. (* = pre-annealed).

Sample code	Area estimated in SEM (mm^2)	Calculated electrical area (mm^2)	Deviation (%)
22a	0.033	0.030	-20
53a	0.093	0.065	-25
111a	0.053	0.065	-10
112a	0.052	0.056	-21
161a*	0.049	0.033	-33
162a	0.064	0.024	-63
52c	0.049	0.050	-20
71c	0.062	0.043	-29
23o	0.060	0.042	-39
33o	0.076	0.056	-53
34o	0.062	0.034	-43
51o	0.049	0.037	-4
72o	0.044	0.010	-74
73o*	0.017	0.037	146

Table 5.4 shows the estimated contact areas and calculated electrical contact areas for the pure wires. Calculations of the uncertainty of the electrical areas assuming an uncertainty for the axes of the ellipse of each $\pm 10 \mu\text{m}$, for R_s of $\pm 5 \Omega$ and that σ_{YSZ} is constant at 0.15 S/cm resulted in a standard deviation of the electrical areas of $\pm 0.015 \text{ mm}^2$. All the electrical areas are smaller than or very close to the physical contact areas.

Table 5.4. The measured (SEM) and electrical areas in mm^2 for thick, pure electrodes. The last column shows the deviations of the electrical areas from the SEM areas.

	Sample code	Area estimated in SEM (mm^2)	Calculated electrical area (mm^2)	Deviation (%)
OCV part	212a	0.058	0.061	5
	213a	0.128	0.139	8
	221a	0.113	0.104	-8
	222a	0.105	0.113	8
	224a	0.144	0.168	17
Polarisation	212a	0.058	0.062	7
	213a	0.128	0.087	-32
	221a	0.113	0.071	-37
	222a	0.105	0.026	-76
	224a	0.144	0.105	-27
	241c	0.064	0.071	11
	242c	0.125	0.147	18
	243c	0.175	0.168	-4

5.2 Polarisation resistance

The polarisation resistance is found as the difference between the low frequency and high frequency intercepts of the impedance arc with the real impedance axis (fig. 5.1). In cases where the series resistance is less than 1 % of the polarisation resistance, the series resistance is not subtracted.

5.2.1 Impure nickel wires as electrodes

In most cases the polarisation resistance increases during the first 24-48 hours at OCV (fig. 5.9, 5.11, 5.12 and 5.13). For many samples in the early experiments, too few measurements were performed in the in the first 48 hours. For samples kept at OCV, R_p was more or less constant at approximately the reached level (e.g. 120-210 $\text{k}\Omega$) but the results did not show good reproducibility (fig. 5.9).

For the polarised samples, R_p dropped upon polarisation (fig. 5.10 and 5.11), approaching a constant value. The values for anodically polarised samples are lower than for cathodically polarised samples. After the polarisation was stopped, the following OCV measurements show an increase in R_p , approaching the level previous to polarisation (fig. 5.10 and 5.11).

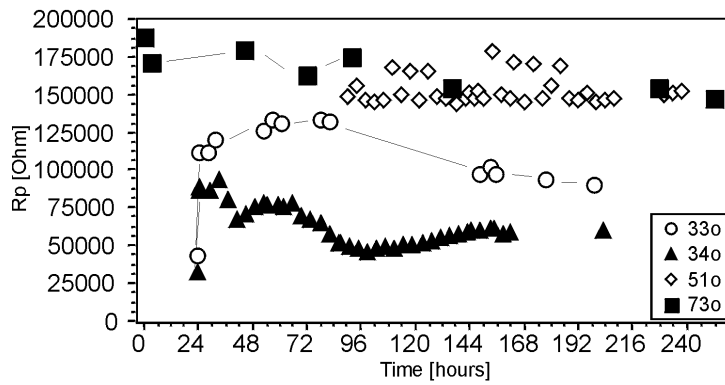


Fig. 5.9. R_p as a function of time for samples with impure nickel electrodes subjected to open circuit voltage. Zero time is when the temperature of the set-up reached 1000°C.

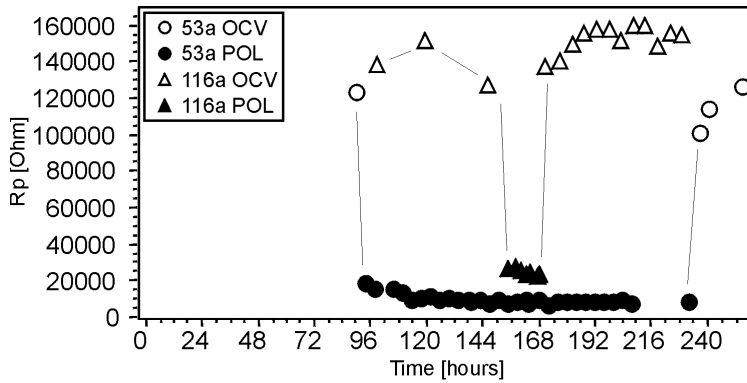


Fig. 5.10. R_p as a function of time for samples with impure nickel electrodes subjected to an anodic polarisation (100 mV). Open and closed symbols indicate measurements during OCV and polarised conditions. Zero time is when the temperature of the set-up reached 1000°C.

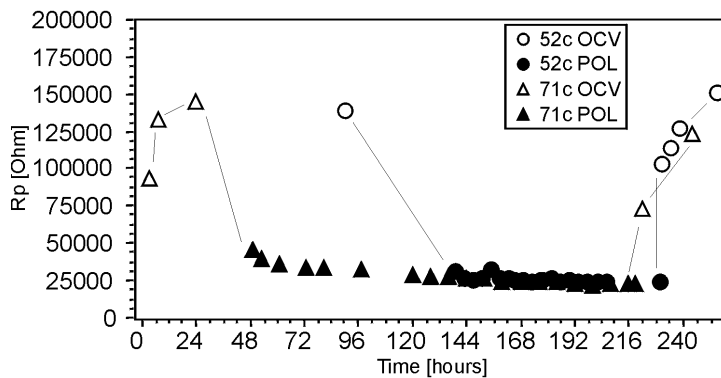


Fig. 5.11. R_p as a function of time for samples with impure nickel electrodes subjected to a cathodic polarisation (100 mV). Open and closed symbols indicate measurements during OCV and polarised conditions. Zero time is when the temperature of the set-up reached 1000°C.

Table 5.5 shows the stable R_p values before and during polarisation together with the corresponding area specific resistance (ASR) and length (of circumference) specific resistance (LSR). The area specific resistance is calculated as SEM contact area times the polarisation resistance. The length specific resistance is found from the product of the length of the circumference of the approximated ellipse and the polarisation resistance. The anodically polarised samples clearly produce the smallest area and length specific resistances, closely followed by the cathodically polarised samples. The samples kept at OCV show much larger values.

Table 5.5. R_p , ASR and LSR for the electrically connected samples with impure electrodes. Both values at OCV prior to polarisation (POL) and values at polarisation are given.

Sample code	R_p [Ω]		ASR [Ωcm^2]		LSR [Ωcm]	
	OCV	POL	OCV	POL	OCV	POL
22a	170000	28000	56	9	14858	2447
53a	124000	8500	115	8	16790	1151
111a	-	12000	-	6	-	1205
112a	125000	6000	65	3.1	14150	679
161a	210000	20000	135	10	24150	1890
162a	146000	21000	71	13	13797	2415
52c	139000	25000	68	12	15679	2820
71c	145000	22000	90	14	16341	2479
23o	40000	-	24	-	4752	-
34o	60000	-	37	-	10086	-
33o	90000	-	69	-	13716	-
51o	150000	-	73	-	13650	-
73o	154000	-	26	-	8716	-

5.2.1.1 Multiple polarisations

The R_p curves for 111a and 112a are shown in fig. 5.12 and 5.13. The periods during open circuit voltage are clearly characterised by higher polarisation resistances than for periods with polarisation applied. However, the R_p values for the successive OCV periods are decreasing for each new period (except for the first and second OCV periods for 111a, but this is believed to be due to the lack of time for stabilisation). The R_p values for the periods with polarisation also decrease in an equal way, leading to lower and lower ASR and LSR over time. Table 5.6 presents the R_p values both at OCV and polarisation and the area and length specific resistances under polarisation. It is observed that the change in R_p from OCV to polarised and back happens within minutes.

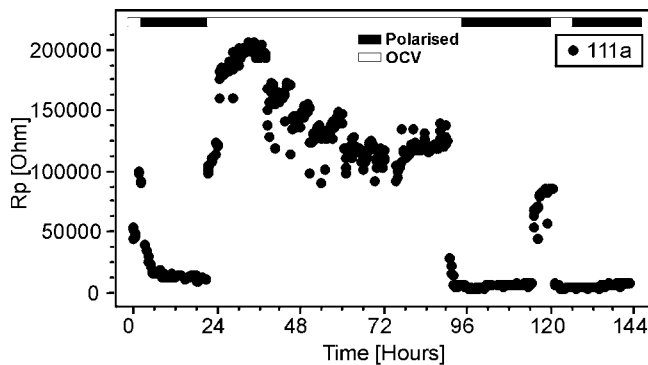


Fig. 5.12. R_p as a function of time for sample 111a. The bar indicates anodic polarisation (100 mV) and OCV periods. Zero time is when the temperature of the set-up reached 1000°C.

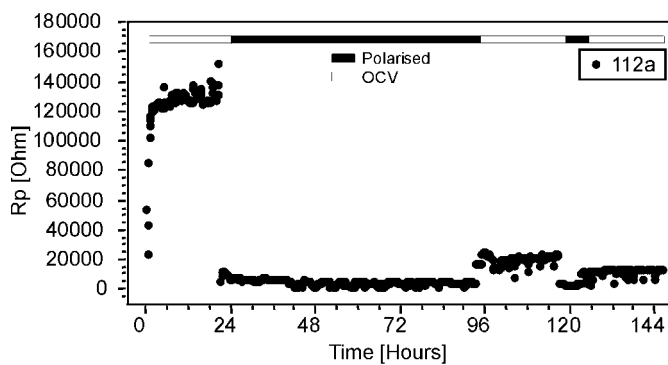


Fig. 5.13. R_p as a function of time for sample 112a. The bar indicates anodic polarisation (100 mV) and OCV periods. Zero time is when the temperature of the set-up reached 1000°C.

Table 5.6. R_p , ASR and LSR for the multiple polarisations on samples 111a and 112a. The first OCV period is followed by the first polarisation (POL) period, which again is followed by the second OCV period and so on.

Period	Sample 111a			Sample 112a		
	R_p [Ω]	ASR [Ωcm^2]	LSR [Ωcm]	R_p [Ω]	ASR [Ωcm^2]	LSR [Ωcm]
1. OCV	-	-	-	125000	65	14150
2. OCV	120-200000	-	-	18000	9	2038
3. OCV	90000	48	9036	12000	6	1358
1. POL	12000	6	1205	6000	3.1	679
2. POL	7000	4	703	2500	1.3	283
3. POL	4500	2.4	452			

5.2.2 Pure nickel wires as electrodes

The figures 5.14 and 5.15 show the polarisation resistance curves for the samples with pure electrodes. An initial decrease in R_p from well above 100 k Ω down to a constant value below 35 k Ω during the first 24-48 hours at OCV is observed. Subsequent anodic polarisation causes the R_p to drop considerably, typically below 1000 Ω for the thick electrodes. R_p increases again upon the change back to OCV. For some samples this constitutes only a few hundred ohms, for others R_p increases approximately to the level before polarisation.

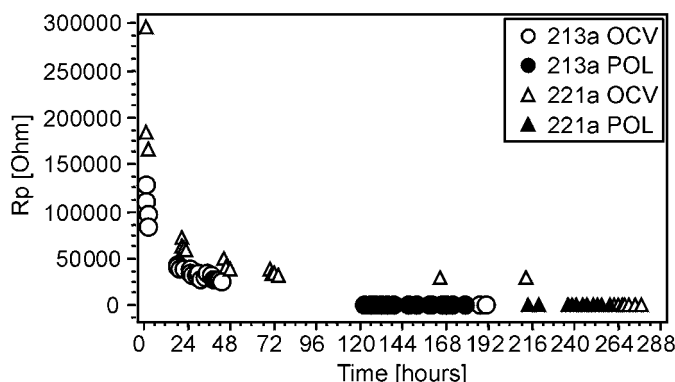


Fig. 5.14. R_p as a function of time for samples with pure nickel electrodes subjected to anodic polarisation. Zero time is when the temperature of the set-up reached 1000°C.

Cathodic polarisation also causes the resistance to drop, but not as low as for anodically polarised samples. The OCV measurements in the post-polarisation period show, contrary to all other types of samples, a further drop in the polarisation resistance (fig. 5.16). This result in ASR values around 2-4 Ωcm^2 compared to 7-17 Ωcm^2 during polarisation.

Table 5.7 shows polarisation resistances, ASR and LSR for the samples with thick electrodes and for sample 92a (thin electrode). The anodically polarised samples clearly show the lowest ASR and LSR values.

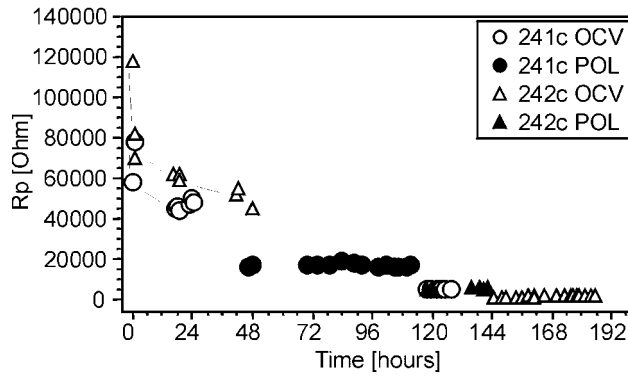


Fig. 5.15. R_p as a function of time for samples with pure nickel electrodes subjected to a cathodic polarisation of 100 mV. Zero time is when the temperature of the set-up reached 1000°C. The R_p values at OCV after polarisation are lower than during polarisation.

Table 5.7. Polarisation resistance, ASR and LSR for the relevant electrically connected samples with pure electrodes. 92a (thin nickel electrode): Only a few measurements were performed before the furnace malfunctioned. Due to a fracture on sample 212a the contact area (and ASR and LSR) is not very well determined.

Sample code	R_p [Ω]		ASR [Ωcm^2]		LSR [Ωcm]	
	OCV	POL	OCV	POL	OCV	POL
92a	--	1549	-	0.49	-	169
212a	17000	6500	10	max. 3.8	1719	657
213a	16000	500	21	0.64	4925	164
221a	30000	770	34	0.87	4860	125
222a	29000	600	30	0.63	7189	62
224a	24000	280	35	0.40	6617	77
241c	50000	16000	32	10	13575	4344
242c	50000	5600	62	7	19370	2169
243c	11000	9800	19	17	3960	3528

5.3 Impedance spectra

The impedance spectra generated in this work generally show a depressed arc, which can be fitted to 1-4 semi-circles with the ‘Equivcrt’ software [20]. Due to the nature of the experiments, it is doubtful if any useful interpretation of the spectra is possible. A meaningful fitting and detailed interpretation would require additional experiments at other temperatures, other polarisation voltages or in other atmospheres to observe the effect of these parameters [44]. However, some general features may be extracted from the impedance analysis. Figs. 5.16 to 5.19 show sequences of selected impedance spectra for pure and impure samples, at OCV before polarisation, at anodic or cathodic polarisation and at OCV after polarisation. In the figures the R_s and R_p graphs are also present to show at which points the selected impedance spectra were obtained. Notice the differences in units: the Y-axis in the R_s and R_p graphs is in Ω , whereas in the impedance spectra, the units of the axes are Ωcm^2 . The descriptions in figs. 5.16 to 5.19 are general to each type of sample (nickel wire, polarisation direction). For additional spectra, see Appendix C.

5.3.1 Spectra from samples with impure electrodes

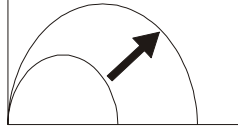
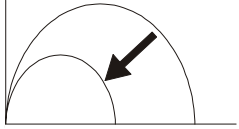
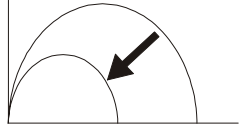
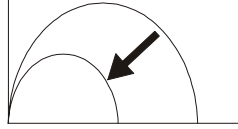
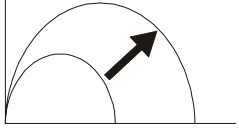
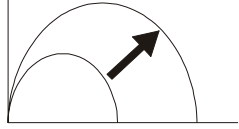
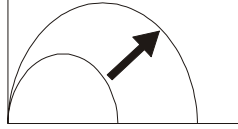
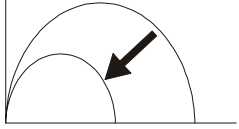
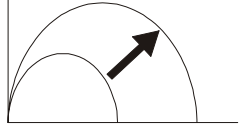
The typical impedance behaviour for the impure electrodes is shown in the figures 5.16 and 5.18. The samples at OCV show an ASR increasing from 25-60 Ωcm^2 to 55-100 Ωcm^2 and a

small decrease in the summit frequency of the depressed arc from 8-17 Hz to 1-2 Hz. Upon polarisation the ASR drops considerably (as seen in section 5.7.1) to 2-15 Ωcm^2 and the summit frequency increases to 4-30 Hz. During the polarisation period the ASR decreases and the summit frequency does not change considerably. At the change back to OCV conditions the ASR increases and the summit frequency decreases to around 1 Hz.

5.3.2 Spectra from samples with pure electrodes

The spectra from the pure samples show a trend at OCV opposite to the impure samples. Initially the polarisation resistance decreases from 50-180 Ωcm^2 to 20-60 Ωcm^2 . There is no general trend for the behaviour of the summit frequency. It may decrease (from 50 Hz to 6 Hz), increase (from 8 Hz to 17 Hz) or stay at the same value. Upon polarisation the polarisation resistance decreases to below 1 Ωcm^2 for anodically polarised samples and to 7-12 Ωcm^2 for cathodically polarised samples. The summit frequency increases. For anodically polarised samples the frequency increases to 100-200 Hz, whereas for the cathodically polarised samples the increase results in frequencies around 10-20 Hz. At OCV after polarisation the polarisation resistance increases slightly for the anodically polarised samples where the summit frequency decreases to 70-80 Hz. For the cathodically polarised samples the polarisation resistance decreases further to 1.5-3 Ωcm^2 and the summit frequency increases to 100-200 Hz. The information in the sections 5.3.1 and 5.3.2 is summarised in table 5.8

Table 5.8. Overview of the trends of the impedance arcs and the summit frequencies as the OCV/polarisation conditions are changed. The arrows show the direction in which the arc (and R_p) grows or shrinks with time and the frequencies given below are the summit frequencies of the arcs. For pure samples no value is given at OCV because no definite trend was found among the samples. The changes in polarisation resistance during polarisation for the samples with pure electrodes are relatively insignificant.

	Impure samples	Pure samples	Pure samples
	Both polarisations	Anodic pol.	Cathodic pol.
OCV	 8-17 Hz → 1-2 Hz		
Polarisation	 8-30 Hz → 40 Hz (Ano) 1-4 Hz → 5-7 Hz (Cat)	 100-200 Hz	 10-20 Hz
OCV after polarisation	 → 0.77-2 Hz	 70-80 Hz	 100-200 Hz

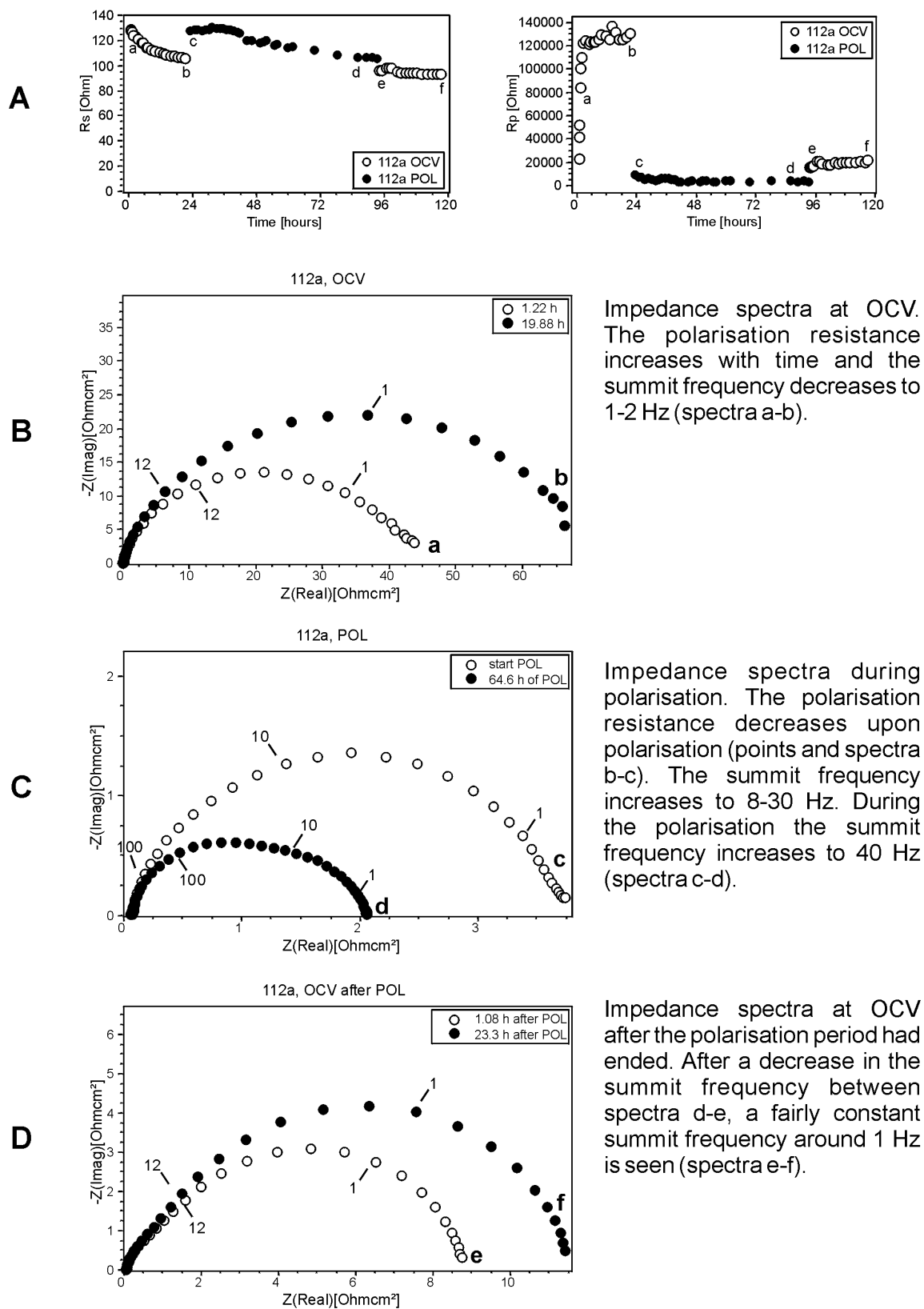
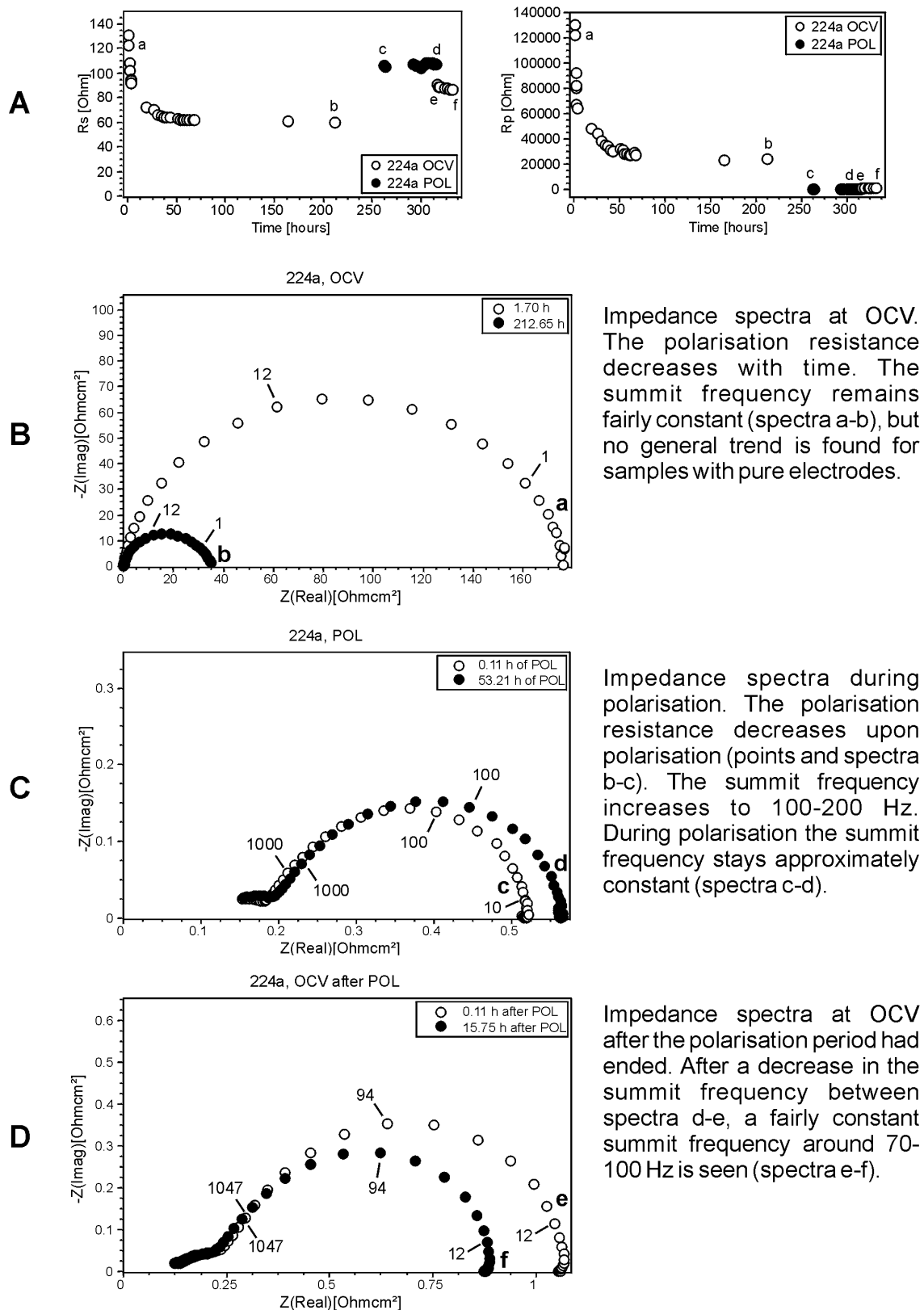


Fig. 5.16. Impedance spectra for the sample 112a (impure electrode). A) R_s and R_p graphs. The letters a-f show the positions of the corresponding impedance plots in B), C) and D). Open symbols indicate an early measurement and closed symbols indicate a measurement some hours later. The numbers in the spectra indicate frequencies.

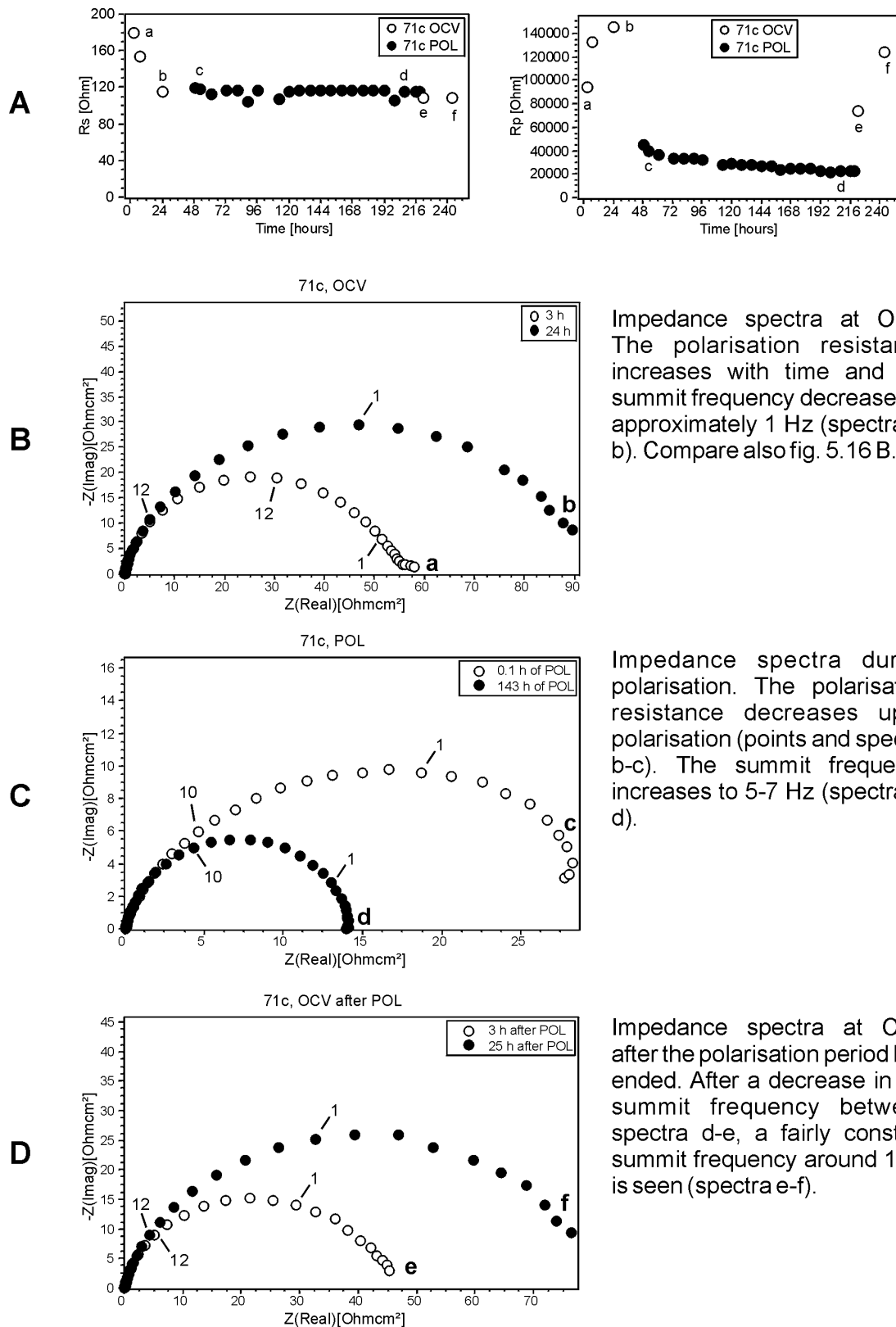


Impedance spectra at OCV. The polarisation resistance decreases with time. The summit frequency remains fairly constant (spectra a-b), but no general trend is found for samples with pure electrodes.

Impedance spectra during polarisation. The polarisation resistance decreases upon polarisation (points and spectra b-c). The summit frequency increases to 100-200 Hz. During polarisation the summit frequency stays approximately constant (spectra c-d).

Impedance spectra at OCV after the polarisation period had ended. After a decrease in the summit frequency between spectra d-e, a fairly constant summit frequency around 70-100 Hz is seen (spectra e-f).

Fig. 5.17. Impedance spectra for the sample 224a (pure electrode). A) R_s and R_p graphs. The points a-f show the positions of the corresponding impedance spectra in B), C) and D). Open symbols indicate an early measurement and closed symbols indicate a measurement some hours later. The numbers in the spectra indicate frequencies.



Impedance spectra at OCV. The polarisation resistance increases with time and the summit frequency decreases to approximately 1 Hz (spectra a-b). Compare also fig. 5.16 B.

Impedance spectra during polarisation. The polarisation resistance decreases upon polarisation (points and spectra b-c). The summit frequency increases to 5-7 Hz (spectra c-d).

Impedance spectra at OCV after the polarisation period had ended. After a decrease in the summit frequency between spectra d-e, a fairly constant summit frequency around 1 Hz is seen (spectra e-f).

Fig. 5.18. Impedance spectra for the sample 71c (impure electrode). A) R_s and R_p graphs. The points a-f show the positions of the corresponding impedance spectra in B), C) and D). Open symbols indicate an early measurement and closed symbols indicate a measurement some hours later. The numbers in the spectra indicate frequencies.

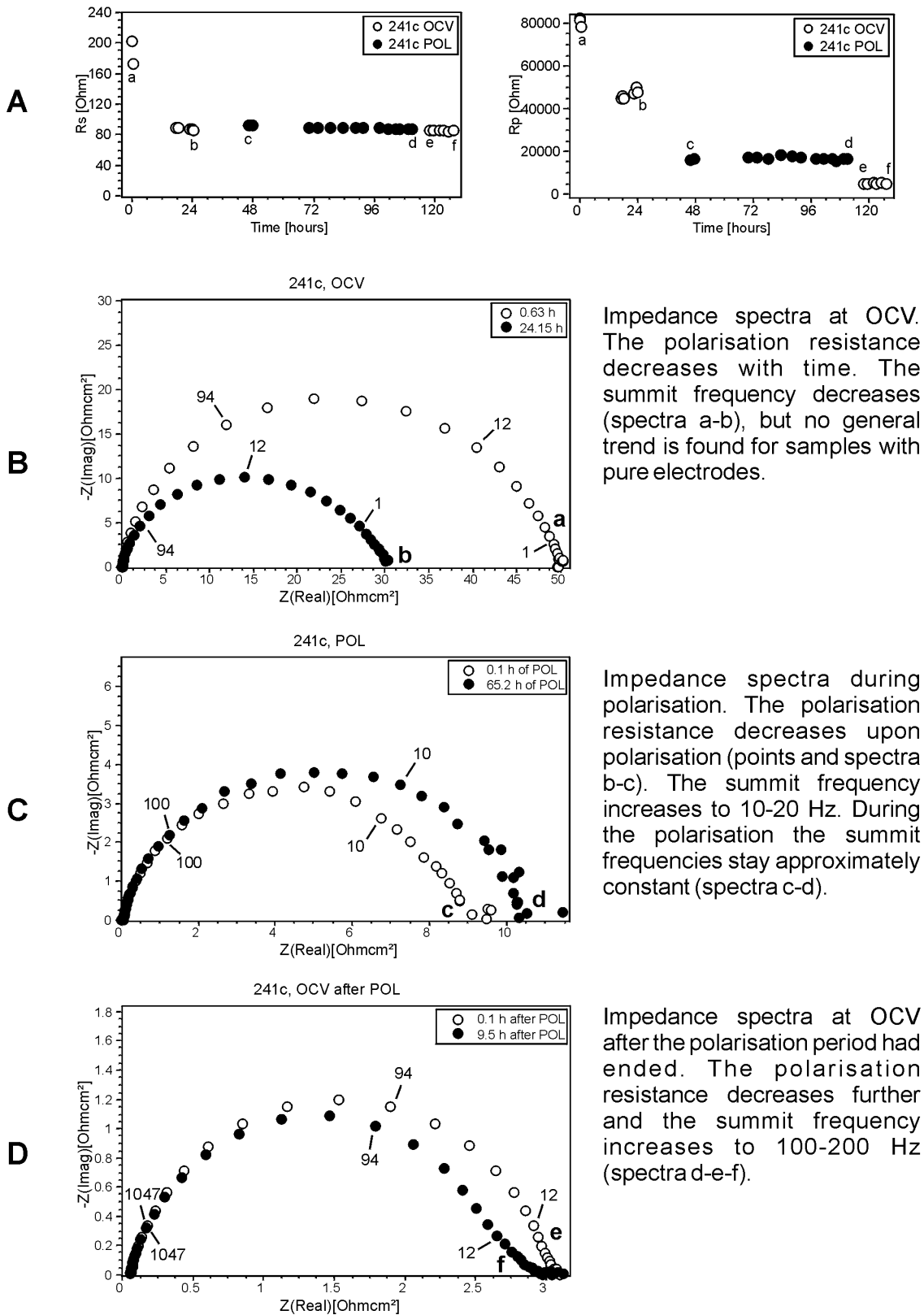


Fig. 5.19. Impedance spectra for the sample 241c (pure electrode). A) R_s and R_p graphs. The points a-f show the positions of the corresponding impedance spectra in B), C) and D). Open symbols indicate an early measurement and closed symbols indicate a measurement some hours later. The numbers in the spectra indicate frequencies.

5.4 Capacitance

An attempt to examine the electrode capacitance at high and low frequencies has been performed. The capacitance at high frequency may provide indications on the apparent thickness of an interfacial more or less blocking phase.

For estimating the thickness of the interfacial phase a fixed frequency of 23 kHz has been chosen as a high frequency just below the range where a large response from the equipment appears. As a low frequency the summit frequency was chosen as a characteristic frequency.

Capacitances at the given frequencies have been calculated [45]:

$$Z = Z_{re} + jZ_{im} \quad (5.3)$$

The admittance, Y, is the inverted impedance:

$$Y = \frac{1}{Z}, \quad (5.4)$$

and may be expressed as:

$$(Y_{re}, Y_{im}) = \left(\frac{Z_{re}}{Z_{re}^2 + Z_{im}^2}, -\frac{Z_{im}}{Z_{re}^2 + Z_{im}^2} \right). \quad (5.5)$$

For an RC-circuit (starting in 0,0) the frequency dependent capacitance may be found:

$$C(f) = \frac{Y_{im}(f)}{2\pi f}. \quad (5.6)$$

Even though the assumption of an ideal RC-circuit is far from the 1-4 more or less depressed semi-circles found during fitting, the 23 kHz point is positioned on the left side of the highest frequency arc and is thereby not greatly influenced by the other arcs.

Correcting for R_s being different from zero and for the area, the capacitances of the frequencies close to 23 kHz (22961 Hz for OCV measurements and 23552 Hz for polarisation measurements) were calculated (table 5.9). For all but one sample (111a, summit) the capacitance increase upon polarisation. All capacitances were in the range of 50 $\mu\text{F}/\text{cm}^2$ to 3 mF/cm^2 . Fig. 5.20 shows the average capacitances for pure and impure samples under OCV and polarisation conditions. Table 5.10 shows the average capacitances, which are used in fig. 5.20.

Table 5.9. Areas specific capacitances at approximately 23 kHz and at the summit frequency.

Impure samples		$C_{23\text{ kHz}}$ [F·10 ⁻⁴ /cm ²]	C_{summit} [F·10 ⁻⁴ /cm ²]	Pure samples		$C_{23\text{ kHz}}$ [F·10 ⁻⁴ /cm ²]	C_{summit} [F·10 ⁻⁴ /cm ²]
111a	OCV	2.1	6.5	213a	OCV	0.5	1.2
	POL	3.0	5.8		POL	5.0	62
112a	OCV	2.1	8.0	224a	OCV	0.5	1.1
	POL	7.0	62		POL	1.9	24
71c	OCV	0.8	1.8	241c	OCV	0.4	0.8
	POL	4.0	30		POL	2.6	5.6
52c	OCV	3.5	22	242c	OCV	0.2	0.5
	POL	6.5	31		POL	4.6	11

Table 5.10. Average capacitances for 23 kHz. A.P. = anodic polarisation, C.P. = cathodic polarisation. The capacitances are obtained by averaging the data in table 5.9.

	Relative time	No. of values	Average capacitance [F/cm ²]	
			Impure samples	Pure samples
OCV	early	4	1.65E-04	4.33E-05
	late	4	3.04E-04	2.13E-04
Anodic Pol.	early	2	4.97E-04	3.43E-04
	late	2	4.01E-04	2.04E-04
Cathodic Pol.	early	2	5.26E-04	3.60E-04
	late	2	5.61E-04	3.09E-04
OCV after A.P.	early	2	4.55E-04	1.11E-04
	late	2	4.27E-04	1.07E-04
OCV after C.P.	early	2	4.45E-04	1.82E-04
	late	2	4.49E-04	1.91E-04

A plot of log (C) versus log (R_p) (fig. 5.21) shows that the capacitance is not correlated with the polarisation resistance, except maybe for the pure electrodes for very small polarisation resistances. Here a trend of increasing capacitance with decreasing R_p is indicated. The same trend is seen for the capacities at 23 kHz.

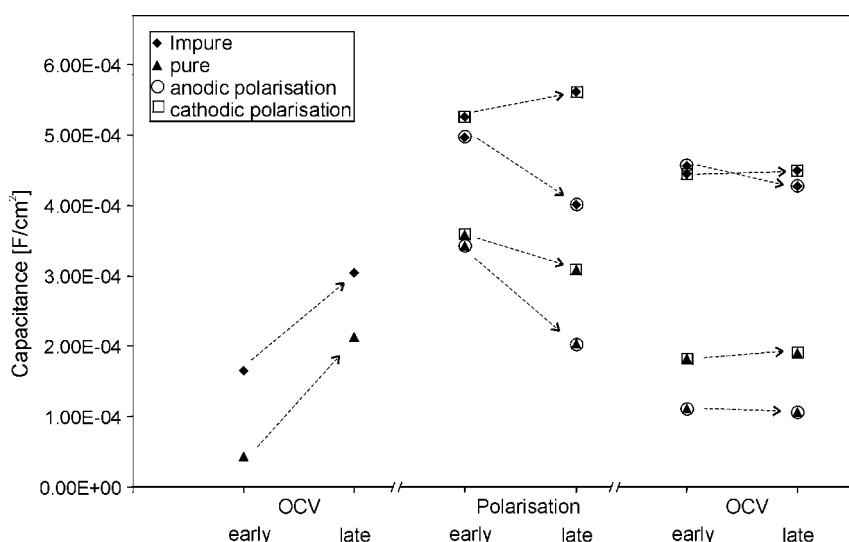


Fig. 5.20. Average capacitances at 23 kHz for the pure and impure samples shown in table 5.10. The first 2×2 points for each type are for early and late in the OCV period before polarisation. The capacitance is increasing for both samples with pure and impure electrodes and values for samples with impure electrodes are higher than for samples with pure electrodes. The next 2×4 points are from early and late in the polarisation period (two for anodically polarised samples Δ and two for cathodically polarised samples \square for samples with pure and impure electrodes, respectively). Again the samples with impure electrodes show larger values than the samples with pure electrodes and during the polarisation the capacitances seem to decrease, except for cathodically polarised samples with impure electrodes. The last 2×4 points are from the beginning of the OCV period after polarisation and after some time at OCV. In this period the capacitances are approximately constant.

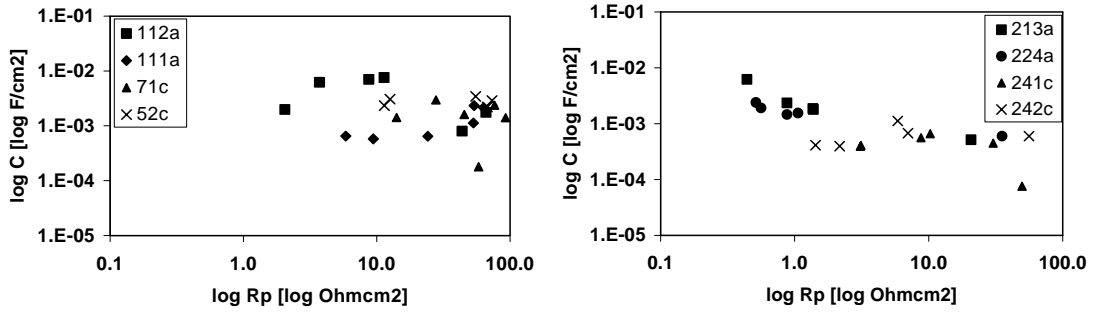


Fig. 5.21. Log (C) versus log (R_p) for capacitances calculated for the summit frequency. Left graph: impure samples; right graph: pure samples.

The general formula for a parallel plate capacitor (eq. 5.7) [45] has been used to calculate the thickness, d , of the interface layer:

$$d = \frac{A\epsilon\epsilon_0}{C}, \quad (5.7)$$

where ϵ_0 is the vacuum permittivity. A dielectric constant $\epsilon = 10$ is used. A is the area and C is the capacitance. At frequencies close to 23 kHz, the calculated thickness is in the order of 10^{-10} - 10^{-11} m. As this distance is equal to approximately 1/10 of an atom radius, the thickness has no physical meaning and other capacities in parallel are necessary to describe the measured capacitances.

If it is assumed that the capacitance originates from an electrochemical process, a rough estimation of the percentage, k , of converted electrons pr. ac cycle is possible from eq. 5.8 [7]:

$$k = \frac{CU}{zNF}, \quad (5.8)$$

where C is the capacitance, U is the applied perturbation voltage, z is the number of charges on the converted species, N is the number of mol Mn atoms covering the contact area, calculated for a Mn_3O_4 layer, with a Mn_3O_4 unit cell length 8.12 Å and half a unit cell high, and F is the Faraday constant. Mn is known to be present in both interfacial regions and is a species, which easily undergo redox processes. The resulting k -values are in the range of 0.3-4.0 %.

5.5 Chronoamperometry

The chronoamperometry measurements produced graphs with current as a function of time for a pure and impure anodically polarised sample (Fig. 5.22 and 5.23). Pure samples seem to develop a stable current faster than the impure samples. The current was typically measured every 600 s during the complete experiment for the samples with impure nickel electrodes, whereas it was measured every 10 s in intervals up to 16 h for samples with pure nickel electrodes.

For all samples (pure, impure, anodic and cathodic polarisation) peaks with a typical interval of 2-4 hours are seen (fig. 5.22 and 5.23). The current initially increases steeply and then decreases to the previous value within 0.5-2 hours. Some samples show irregularities in some intervals e.g. sample 241c in fig. 5.24. For some samples, peaks in both directions are seen and for some pure samples up to 7-hour intervals with no peaks have been observed.

Typical values of current densities are shown in table 5.11. The pure, anodically polarised samples clearly give the highest values.

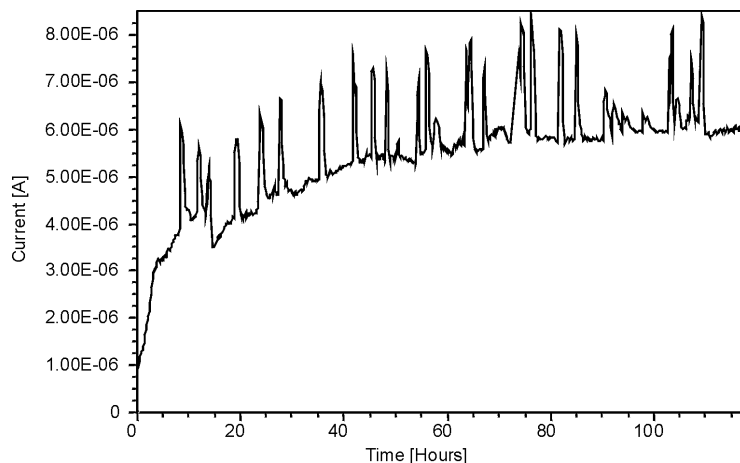


Fig. 5.22. Current as a function of time from the beginning to the end of the polarisation for sample 53a (impure). The highest peak corresponds to 9.2 mA/cm^2 , and between the peaks the current density is 6.5 mA/cm^2 . The measurements were performed every 600 s.

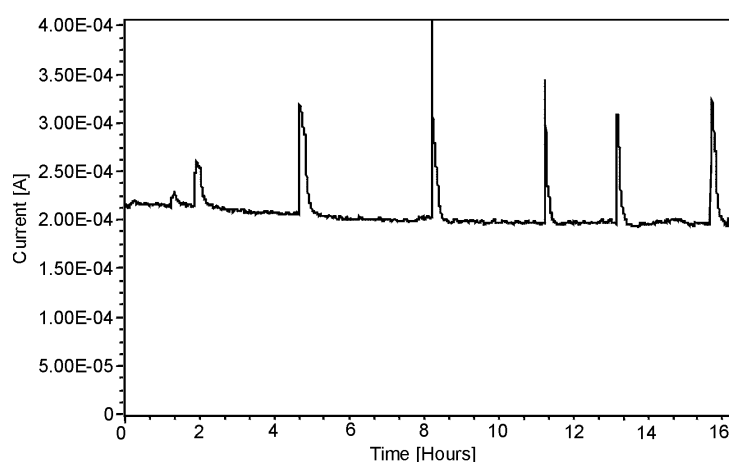


Fig. 5.23. Current as a function of time for sample 222a (pure) from 2 hours after polarisation start. The measurement lasted approximately 16 hours. The current peaks are seen regularly with intervals of 2 to 4 hours. The highest peak corresponds to a current density of 350 mA/cm^2 and between the peaks the current density is 200 mA/cm^2 . The current was measured every 10 s.

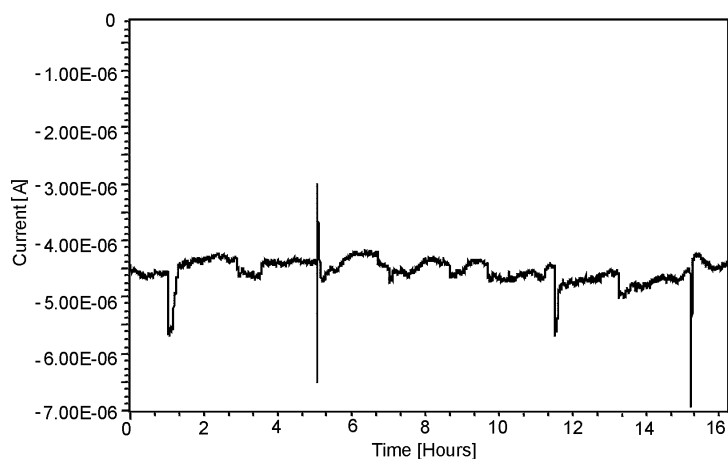


Fig. 5.24. Current as a function of time for sample 241c (pure) starting 2.5 hours after the polarisation start. The curve does not show peaks with regular intervals. The current was measured every 10 s.

Table 5.11. Typical values of current densities for pure and impure samples. Polarisation voltage was ± 100 mV.

	Polarisation	Current density [mA/cm ²]	
		Typical values	Max. peak
Pure	Anodic	130 to 170	390
	Cathodic	-7 to -22	-50
Impure	Anodic	3 to 20	30
	Cathodic	-3 to -7	-30

5.6 Potential sweeps

Potential sweeps (0 mV-100 mV- 0 mV) have been performed on samples with pure electrodes. Different sweep rates have been used, but only the 0.2 mV/s and 100 mV/s are shown. The reproducibility of the potential sweep measurements is poor and the position of the curves seems different from samples to sample. Due to an offset in the measuring equipment, the sweeps start at a few millivolts and reach a few millivolts over the desired 100 mV. All potential sweeps were performed at the end of the polarisation periods.

The anodically polarised samples show slightly curving trends, as shown in fig. 5.25 for sample 224a. Comparing the inverse slopes (and correcting for R_s) of the sweeps in fig. 5.25, a polarisation resistance of 721Ω is found at low potential, whereas 239Ω are found at high potentials. The 721Ω are comparable to an OCV situation and the 239Ω are comparable to a situation right after polarisation start. Comparing these values with the R_p before the change from OCV to polarised conditions and R_p right after polarisation start, it is found that whereas the values for R_p at polarisation were close to each other (252Ω vs. 239Ω), the values at OCV disagreed ($24 \text{ k}\Omega$ vs. 721Ω). It is, though, necessary to consider that the potential sweep was performed immediately after the polarisation period ended, which means that the sample was in an activated state with no time for stabilisation at OCV.

Two of the cathodically polarised samples show more linear trends and but are more noisy. The last one shows a jump in the current at -55 mV. Appendix D contains more potential sweeps, both for anodically and cathodically polarised samples.

The potential sweep data have not been explored further.

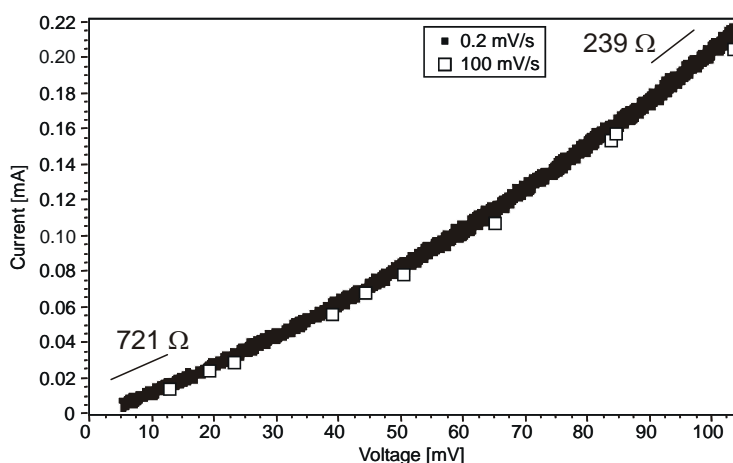


Fig. 5.25. Potential sweep curves for sample 224a. The inverse slopes, corrected for R_s , around 0 mV (721Ω) and 100 mV (239Ω) are displayed in the plot.

5.7 Discussion on electrical measurements

5.7.1 Series resistance

5.7.1.1 R_s values

Due to the load and temperature the nickel wire creeps during the experiments, increasing the contact area with time. The series resistance becomes almost constant after 24-72 hours, indicating that the creep rate of the nickel is low after this period and a final contact area size is reached. The series resistance curves flatten earlier for the pure wires than for the impure wires. This may be due to the hardening effect of the impurities.

The change in R_s upon polarisation is not understood but must be connected to a smaller electrical area (eq. 5.1). This smaller area, however, does not result in a higher polarisation resistance, indicating that changes in the chemical composition or physical distribution of the impurity phase in the interfacial region take place.

5.7.1.2 Electrical contact areas

Almost all the electrical contact areas for both the pure and impure electrodes are smaller than or very close to the area measured from SEM images. This implies that for some samples only part of the contact area was electrically in contact.

Sample 73o, which was pre-annealed, showed a large deviation between the physical and electrical contact area. One possibility is that unidentified parts of the contact area exist; another is that the conductivity was higher than the designated value of 0.15 Scm^{-1} . To achieve a deviation comparable to other samples, a conductivity of at least 0.25 S/cm is necessary. Sample 161a was also pre-annealed but shows a quite normal relationship between the contact area and the electrical area. Uncontrolled and unknown events have obviously played a role in the case of 73o.

5.7.2 Polarisation resistance trends

5.7.2.1 Trends for OCV conditions

A comparison of the development of the polarisation resistance with time for samples with impure and pure electrodes at open circuit voltage shows two very different trends. Impure electrodes display an initial increase in the polarisation resistance and a subsequent stabilisation at a high resistance after approximately 24-48 hours. The polarisation resistances for pure electrodes show an initial decrease and a subsequent stabilisation at a relatively low resistance after 24-48 hours.

As both R_p and R_s stabilise within equal time limits, the development of the R_p for pure samples may be ascribed to the expansion of the contact area and extension of the circumference of the contact area. A complete correlation does not exist, but the winding circumferences result in an increased TPB length-to-area relation, and as R_p is supposed to correlate with the TPB length, this is a possible explanation.

For samples with impure electrodes another explanation for the development of R_p must be considered and as the only difference is the purity of the nickel, it is likely that the formation of the rim ridge, the impurity film/particles and possibly the hill and valley structure is the main cause for the increase in R_p .

de Boer [17] shows graphs for R_p vs. time for both pattern, porous and cermet electrodes and all three graphs show initial increases in the polarisation resistances. For pattern electrodes a period of 100 hours is necessary for the electrodes to reach a steady performance. de Boer relates those changes to changes in the electrode microstructure. For porous electrodes this period is reduced to 30 h. Tosoh TZ-8Y powder was used for the electrolytes. No indication of the impurity content of the nickel was given.

5.7.2.2 Trends for polarised conditions

Upon polarisation, both the impure and pure samples without exception show a drop in R_p to relatively constant values. A subsequent increase in R_p after changing back to OCV conditions is seen for all impure samples and the anodically polarised pure samples.

During anodic and cathodic polarisation the electrochemical process occurs in different directions. This difference is only distinguishable in the trends of the polarisation resistances for samples with pure electrodes. Samples with impure electrodes show identical trends for both anodically and cathodically polarised samples and this may be ascribed to the larger amount of impurities, which through the development of the rim ridge and the hill and valley structures changes the determining properties.

It is observed by de Boer [17] that periods with anodic polarisation, I-V measurements and impedance measurements at different pH_2 and pH_2O have a large influence on the polarisation resistance value for all types of electrodes.

5.7.3 Polarisation resistance values

Impure electrodes clearly show larger polarisation resistances than pure electrodes, both at OCV and polarisation. Polarisation resistances for the anodically polarised samples seem to be lower than for samples subjected to cathodic polarisation. For the impure electrodes the R_p 's range from 6-21 k Ω at anodic polarisation and from 22-25 k Ω at cathodic polarisation. For the pure electrodes the resistances are 0.3-6.5 k Ω at anodic polarisation and 7-17 k Ω at cathodic polarisation. The variations within each group are probably due to differences in the exact morphology of the contact on each individual sample and the amount/distribution of impurities present.

The impure samples subjected to multiple anodic polarisations showed that for each polarisation the R_p became lower, thus giving rise to the overall lowest values for anodically polarised samples with impure electrodes, 2.5 k Ω and 4.5 k Ω . This type of experiment was not conducted with pure samples.

Area specific resistances or length specific resistances are better standards of reference. For the anodically polarised samples the pure electrodes show the absolutely lowest ASR values, 0.29-0.87 Ωcm^2 compared to 3.1-13 Ωcm^2 for impure electrodes. Similarly, the cathodically polarised samples with a pure nickel wire show ASR's from 5-17 Ωcm^2 and samples with impure electrodes show values around 12-14 Ωcm^2 . For samples at OCV, the values for impure electrodes are in the range 24-135 Ωcm^2 whereas for the pure samples the range is 10-62 Ωcm^2 . It is realised that there is a factor of 10 between the best, impure and the best, pure anodically polarised electrode.

The anodically polarised samples with impure electrodes showed length specific polarisation resistances of 679-2447 Ωcm and samples with pure electrodes gave values between 62 and 657 Ωcm . For cathodically polarised samples such a difference does not exist, for samples with pure and impure electrodes all LSR's were found in the range 2400-4350 Ωcm and the samples with pure electrodes showed some of the highest resistances.

In the literature only very few point electrodes are examined (section 1.5). Considering the fact that the Ni point electrodes in the present study show a large scattering in the data it seems that a number of electrodes have to be studied to determine average or typical values of polarisation resistances. In the literature only very little information is available with respect to the morphologies of the Ni and YSZ surfaces and the purity of the nickel. Furthermore, the literature data was obtained under different pH_2/pH_2O ratios and at different temperatures. Only a very few examinations of microstructural and chemical changes were presented. All those different or unknown conditions makes it difficult to compare results from the present study with literature data, especially regarding the impact of impurities on the development of the polarisation resistance with time. Length specific polarisation resistances for Ni point electrodes found in the literature are not very consistent. Values from ca. 200 Ωcm at 960°C [11] to $2 \cdot 10^4$ Ωcm at 960°C (extrapolated, [9]) are found. Values for pure, anodically polarised electrodes in the present work are generally lower than 200 Ωcm .

In the multiple polarisation experiment the polarisation resistance dropped in each polarisation period and thereby the lowest R_p values for impure electrodes and anodically polarised samples were achieved. The R_p during the intervening OCV periods were also successively lower, indicating that some irreversible processes were active.

The decrease/increase in R_p when polarisation starts/stops is likely to be related to changes in the interfacial region. Polarising impure samples causes a large drop in R_p , polarising pure samples causes a smaller drop in R_p but to even lower values than for the impure samples. Aaberg et al. [29] called this phenomenon electrode activation and considered the primary mechanism to be the nickel redistribution. This is obviously not the case in the present investigation whereas the impurities are likely to influence the activation.

5.7.4 Capacitance

The very large capacitances found for the Ni-YSZ interface are not uncommon. Kek et al. [13] and references therein state the typical double layer capacitance to be $10 \mu\text{F}/\text{cm}^2$, but find capacitances several times larger than this at 700 and 800°C. Kek et al. [13] calculated the parallel plate capacitor distance to be too small to have any physical relevance and concluded that the found capacitance is not representing the double layer, but that an adsorption capacitance may be responsible for the large values.

Fig. 5.21 showed that the capacitance is independent of the polarisation resistances, except maybe for the pure, anodically polarised samples. For those, the capacitance seems to increase with decreasing R_p .

5.8 Conclusion on electrical measurements

- No major differences between pure and impure electrodes were seen concerning R_s or electrical contact area.
- Of all samples the anodically polarised samples with pure electrodes show the absolute lowest R_p , ASR and LSR.
- Samples with pure, anodically polarised electrodes show about 10 times lower ASR than samples with impure electrodes.
- The development of the polarisation resistance with time is very different for samples with pure and impure electrodes. For samples with impure electrodes, R_p increase with time at OCV. For samples with pure electrodes, R_p decreases with time at OCV.
- The samples with impure electrodes where multiple anodic polarisations were applied showed lower R_p , ASR and LSR for each polarisation period.
- The interfacial capacitance is very high and the calculated thickness of the interface layer is too small to reflect any layer thickness of a parallel plate capacitor. It is therefore attributed to a redox capacitance, possibly Mn_3O_4 , in the interface impurity region.

6 Overall summary and discussion

The chapters 3, 4 and 5 discussed the individual results. In this chapter a connection between the results from the three chapters is attempted.

The evolution of nickel/YSZ interface with two different impurity contents of the nickel was examined structurally, chemically and electrically. It is possible to distinguish general trends for both types of interfaces, but the differences from sample to sample were noticeably. This applies to contact area geometry, details in microstructure, trends and values of polarisation resistance, the potential sweeps and irregularities in the current graphs.

It is suggested that all these individual features are controlled by the impurities both with respect to local distribution and chemical composition.

6.1 Impurities and structures

The Ni-YSZ interface was found to be dynamic at 1000°C in a hydrogen atmosphere. Both the nickel and the YSZ surfaces were subjected to comprehensive changes during heat treatment.

Most of the samples developed a hill and valley type structure at the Ni-YSZ interface with a topography and morphology depending on the impurity content in the nickel wire. The higher concentration of impurities promotes the development of a structure with a topography with amplitudes 3-5 times larger than the YSZ/pure nickel interface.

Impurities in the YSZ were found to have segregated to the YSZ surface during heat treatment.

The impurities in the impure nickel wire segregated to the nickel surface and the Ni-YSZ interface where they manifested themselves as particles, which were several microns in diameter.

Combined, the impurities from the nickel and the YSZ formed an interface film more or less covering the contact area. The same phenomenon was seen for samples with pure electrodes even though to a lesser extent.

A similar observation was, that the magnitude of the rim ridge was controlled by the impurity content of the nickel wire and even though the rim ridge for samples with pure nickel wires seems very small, it is readily recognised with the SEM and AFM. The impurities present in the starting materials thus end up at the three phase boundary even for small amounts of impurities.

The impurity phase is an alkali silicate glassy phase, possibly containing yttrium (and maybe zirconium). For polarised samples with pure nickel electrodes, the hill and valley structure was not the dominating structure. Instead an interface layer of redistributed YSZ and Ni was found. The impurity distribution in the interface layer has not been determined.

6.2 Impurities and resistance

The different concentrations of impurities in the nickel wires cause totally different trends of the polarisation resistance with time. For the samples with impure electrodes the polarisation resistance increases strongly during the first 24-48 hours whereas for the samples with pure electrodes it decreases strongly in the first 24 hours.

The decrease in R_p for samples with pure electrodes may be correlated with the expansion of the contact area. This effect is completely overridden for the samples with impure electrodes where the increase in R_p is ascribed to the development of the rim ridge at the three phase boundary and the formation of a (partly) blocking interface film, covering the contact area. This is so deteriorating for the electrode that the polarisation resistance increases and only reaches a stable value when the mobile impurity phase has reached a (quasi-?) stable distribution. The rim ridge

and impurity film on samples with pure electrodes do not affect the polarisation resistance to any obvious degree, but an influence cannot be excluded.

The rim ridge, the blocking film and possibly the hill and valley structure apparently evolve relatively fast and when the polarisation begins, the development is already advanced.

The anodic and cathodic polarisations influence the electrical properties of the interfacial region. The drop in R_p that both pure and impure samples experience is believed to be caused by the change in the electrical field in the interface region. This causes a redistribution of the interface film, such that larger unblocked areas become available to current passage.

The above-mentioned interpretation is supported by the fact that the polarisation resistances for samples with pure nickel wires generally are lower than for samples with impure nickel wires. The drop in polarisation resistance is not nearly as large for samples with pure electrodes as for samples with impure electrodes, indicating that, due to the smaller amount of impurity phase present, large, 'clean' electrical contact areas already exist.

The area and length specific polarisation resistance for anodically polarised samples with pure electrodes is generally a factor of 10 lower than for samples with impure electrodes.

Figure 6.1 is comparing LSR values at OCV from this study with literature values for different types of electrodes. Some overlap between the pure and impure electrodes exist, but the pure electrodes cover a range of values up to 5 orders of magnitude larger than the impure electrodes in the $\ln(1/LSR)$ vs. $1000/T$ plot. The point electrode from Guindet et al. [11] is the only one that comes close to the pure electrodes from the present study. The purity of their nickel ball electrode is not specifically mentioned, only that it is 'pure'. The electrolyte was polycrystalline 10 mol% YSZ.

Extrapolating the lines for the data from de Boer [17], Bieberle [14] and Yamamura [5] it is realised that the best, pure electrodes are at least two orders of magnitude above that. This also seems to be the case at lower temperatures, assuming an activation energy similar to that of the cermet electrodes from de Boer [17] and the pattern electrodes from Bieberle [14].

From the literature it is established that an impurity phase from the YSZ is present in the grain boundaries and at the surface of YSZ treated at elevated temperatures [30]. The impurity phase is a complicated system and its composition depends on a number of parameters such as the impurity content of the starting powder, sintering temperature and atmosphere and subsequent heat treatment [46].

The glassy impurity phases are known to contribute significantly to the total resistivity of the electrolyte material [2, 47]. Badwal [47] suggests that the oxygen ion transport across grain boundaries only takes place where the YSZ grains are in direct contact; impurity phases in YSZ appear to have low oxygen ion conductivity.

de Ridder et al. [48] probed the surface of 3 and 10 mol% YSZ samples by low energy ion scattering (LEIS). By a combination of annealing at 300°C and oxidation with atomic oxygen they achieve a clean YSZ surface before annealing at 300-1600°C for 5 hours in oxygen. The LEIS surface analysis revealed that below 900°C no impurities were detected on the surface but for temperatures above 1000°C the surface was completely covered by the impurities Si, Na and Ca. The impurities were restricted to one atomic layer. The bulk content of the impurities is stated to be less than 300 ppm. de Ridder et al. have found that the impurity layer practically prevents oxygen exchange at the surface and that it is believed to be responsible for the bad performance of SOFC.

Considering the results obtained with the nickel/YSZ interface in the present work, this may be a one-sided explanation for the bad performance. The impurities migrating out of the YSZ are important, but the nickel contributes with impurities and the three phase boundary zone is affected by the impurity phase. The XPS, which probes up to 30 monolayers, indicates that the impurity film in the contact areas on samples with both pure and impure nickel electrodes probably is thicker than one atomic monolayer. A similar problem with impurities may exist at the cathode/electrolyte interface with impurities from both the YSZ and the cathode material.

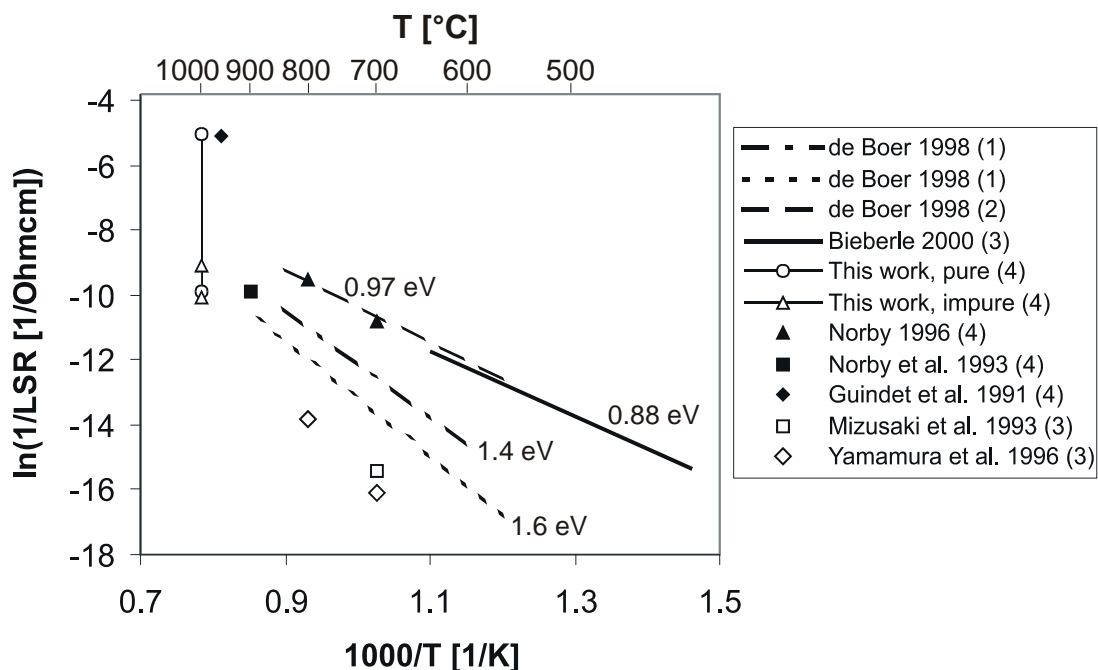


Fig. 6.1. $\ln(\text{LSR}^{-1})$ vs. $1000/T$. Data from the present study have been plotted along with data from [17] and [14]. Additionally LSR values from Ni/YSZ anodes from the literature listed in [49] and [5] have been used. The numbers behind the references indicate the type of electrode: (1) porous, (2) cermet, (3) pattern, (4) point. pH_2 - pH_2O values for the different data are listed in the table below.

Table 6.1. pH_2 - pH_2O values for the data plotted in fig. 6.1.

Reference	pH_2 [atm]	pH_2O [atm]
Guindet et al. (1991) [5]	0.2	0.0027
Norby et al. (1993) [49]	0.0012	0.006
Mizusaki et al. (1993) [49]	0.01-0.05	0.012-0.0165
Norby (1996) [5]	0.1-1.0	0.0085
Yamamura et al. (1996) [5]	0.01	0.0085
de Boer (1998)	0.905	0.021
Bieberle (2000)	0.136	0.0005
This work	0.97	0.03

Fig. 5.24 showed that the current is not stable with time. Intervals of quasi-stable current are followed by intervals where the current is suddenly increasing, and then decreasing again over a longer time span. This behaviour may be taken as an indication that the interface/impurity phase is not static during polarisation. The sharp peaks indicate that after some time a tension is build up. At a point this results in a complete instability and the system reacts, allowing the tension to be relieved. Assuming that the impurity phase in the interface is involved, it is clear that at the time of the peak, the resistance is lowered (and the current increases), and this points to a temporary redistribution of the impurity phase. A relatively slowly development towards the quasi-stable state signifies the gradual return to a situation where a new tension is building up.

Current vs. time graphs in Aaberg [50] does not show any peaks similar to the peaks in the present work, neither at anodic nor cathodic polarisations.

In the literature several suggestions of the scenario in the vicinity of the three phase boundary is presented. In Mogensen et al. [5] a possible reaction path is shown (fig. 6.2 A). Fig. 6.2 B shows the locations of the rim ridge, the partially blocking interface film between the YSZ and the impurity film on the YSZ surface. All three impurity elements may influence the reactions shown in fig. 6.2 A. The rim ridge is an obstacle for processes taking place at or close to (within 1-3 μm) from the three phase boundary. The partly blocking interface restricts any reactions at the Ni-YSZ interface and the impurity layer on the YSZ surface may impede the water formation reaction.

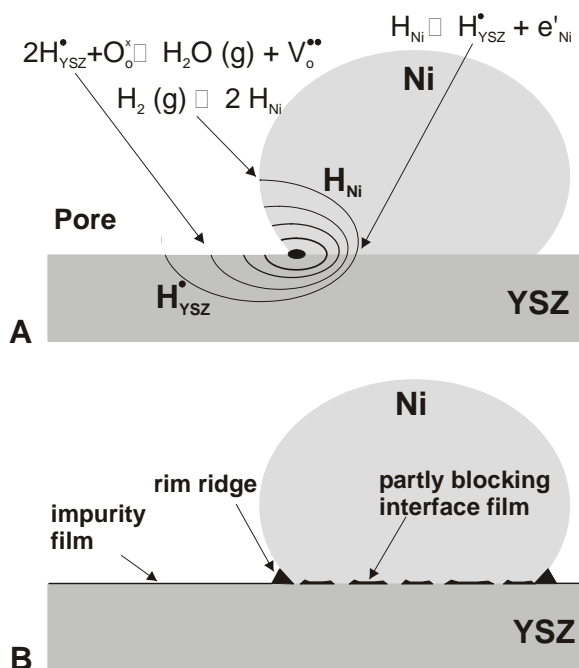


Fig. 6.2. A) A possible reaction path when a certain solubility of hydrogen is considered in both YSZ and Ni (from Mogensen et al. [5]). B) An illustration of the locations of the impurity elements, which are found in the present study. Comparing the two figures, it is clear that the impurities are bound to affect at least some of the reactions. The partially blocking film of impurities between the nickel and the YSZ may seriously restrict any charge transfer reaction taking place at the interface. Likewise, the rim ridge is an obstacle for reactions occurring at or near the three phase boundary. Finally the impurity layer on the YSZ may impede the water formation reaction.

The cermet structure of real Ni-YSZ anodes is, of course, different from the simplified interface used in the present study. The distribution of the impurities in cermet anodes has not been thoroughly examined but as the NiO used to produce cermet anodes at Risø National Laboratory has an impurity content, which lies somewhere between the two studied compositions, it is possible that some effect of impurities upon the performance exists, and indirect evidence for such impurity effects in Ni-YSZ cermets has been presented [18, 51].

6.3 Structures and polarisation

The interfacial electrode resistance is very much dependent upon microstructure, three phase boundary zone and porosity as shown by [2] and references therein. Decreasing electrode surface area and three phase boundary area result in increasing electrode resistance.

For the impure nickel electrodes no differences concerning structures were found on the different types of samples (non-polarised, anodically polarised and cathodically polarised). Possibly the large amount of impurities present here conceal any difference there might be. The samples with pure electrodes do show a difference in the type of structures, both from the structures on the impure samples but also dependent on the polarisation conditions.

For the anodically polarised samples it may further be speculated that the interface layer expands the three phase boundary and thereby improves the performance. The process of changing the interface morphology to nano-sized particles is driven by the passage of current.

7 Final Conclusions

- The Ni-YSZ interface is dynamic at 1000°C in a wet hydrogen atmosphere. A hill and valley structure was found on all samples with impure nickel electrodes and on non-polarised samples with pure nickel electrodes. By developing this structure, the system lowers its overall free energy.
- For both types of nickel electrodes (99.8% Ni and 99.995% Ni) impurities were found in the interfacial region, both as a rim ridge situated on the three phase boundary and as a film, which is more or less covering the contact area. Impurity particles were also found in the contact area. Impurities from the YSZ also contribute to the impurity phase.
- The impurity content in the nickel is determining for the morphology of the developed structures, for the amount of impurity particles in the interfacial region and for the size of the rim ridge of impurities surrounding the contact area.
- An electromigration process is active for anodically and cathodically polarised samples with pure nickel electrodes, resulting in an interface layer consisting of nano-sized particles. A granular structure is found on cathodically polarised samples.
- The development of the polarisation resistance with time is very different for samples with pure and impure electrodes. Samples with impure electrodes show an initially increasing R_p , which is related to the formation of the rim ridge and interfacial impurity film. Samples with pure electrodes show an initially decreasing R_p , which is related to the increase of the contact area.
- The impurity content in the nickel influences the area and length specific polarisation resistance. The lowest ASR for anodically polarised samples with pure nickel electrodes is a factor of 10 lower than for anodically polarised samples with impure nickel electrodes. For OCV samples, the $\ln(1/LSR)$ vs. $1000/T$ graph showed a differentiation between the samples with impure and pure electrodes. The data for impure electrodes were consistent with most literature data. The pure electrodes were up to a factor of 100 better than the impure electrodes.

8 Outlook

After three years of work with the Ni-YSZ interface and the influence of impurities, it is clear that there are still many areas to explore.

- Experiments to test, which influence impurities have on cermet anodes are essential.
- It would be valuable to examine the impact of the different elements or combinations of elements in the impurity phase.
- It would also be interesting to obtain knowledge on what effect lower temperatures would have on the impurity distribution and structure development.
- Regarding the impedance spectroscopy, a comparison of impedance spectra at lower temperatures and possibly at other polarisation voltages and in drier or wetter atmospheres would help shed some light on the factors contributing to the polarisation resistance and its behaviour.
- For the structures it would be especially interesting to follow the development both in a longer and shorter time perspective.
- To investigate how the distribution of impurities changes with polarisation. By keeping the potential during cooling, perhaps a different picture of the impurity distribution would emerge.
- An examination of SOFC cathodes may show a similar tendency with impurity segregation to the interface and a characterisation of the interfacial structures and impurity distribution would be valuable.
- Examining extremely pure Ni-YSZ interfaces would have little technological interest but would perhaps help gain basic knowledge on the interplay between interfaces and impurities.

All this, of course, leads to the final question: if the impurities constitute a serious problem for real anodes and cathodes, then how can it be dealt with?

References

- [1] Minh, N. Q. and Takahashi, T., Science and technology of ceramic fuel cells, Elsevier (1995).
- [2] Badwal, S.P.S., Drennan, J., Interfaces in zirconia based electrochemical systems and their influence on electrical properties, Science of Ceramic Interfaces II (1994) 71-111.
- [3] Kuzjukevics, A., Linderoth, S., Influence of NiO on phase stabilisation in 6 mol% yttria stabilized zirconia, Materials Science & Engineering A A232 (1997) 163-167.
- [4] Linderoth, S., Bonanos, N., Vels Jensen, K., Bilde-Sørensen, J.B., Effect of NiO-to-Ni transformation on conductivity and structure of yttria-stabilized ZrO₂, J. American Ceramic Society 84 (2001) 2652-2656.
- [5] Mogensen, M., Sunde, S., Primdahl, S., SOFC anode kinetics, Proc. of the 17th Risø International Symposium on Materials Science. Poulsen, F.W., Bonanos, N., Linderoth, S. Mogensen, M., Zachau-Christensen, B. (editors), Risø National Laboratory, Denmark (1996) 77-100.
- [6] Mogensen, M., Skaarup, S., Kinetic and geometric aspects of solid oxide fuel cell electrodes, Solid State Ionics 86-88 (1996) 1151-1160.
- [7] Primdahl, S., Nickel/yttria-stabilised zirconia cermet anodes for solid oxide fuel cells, Ph.D. Thesis, Risø-R-1137(EN), University of Twente and Risø National Laboratory, Denmark (1999).
- [8] Norby, T., Velle, O.J., Leth-Olsen, H., Tunold, R., Reaction resistance in relation to three phase boundary length of Ni-YSZ electrodes, Proc. of the 3rd International Symposium on SOFC, Singhal, S.C. & Iwahara, H. (editors), The Electrochemical Soc. 93-4, Pennington, NJ (1993) 473-478.
- [9] Norby, T., Electrochemical behaviour of Ni-YSZ electrodes, Proc. of the 2nd European Solid Oxide Fuel Cell Forum, Thorstensen, B (editor), Oslo, Norway (1996) 607-616.
- [10] Norby, T., Kofstad, P., Hydrogen isotope effects on Ni/YSZ electrodes, Proc. of the 17th Risø International Symposium on Materials Science. Poulsen, F.W., Bonanos, N., Linderoth, S. Mogensen, M., Zachau-Christensen, B. (editors), Risø National Laboratory, Denmark (1996) 381-386.
- [11] Guindet, J., Roux, C., Hammou, A., Hydrogen oxidation at the Ni/zirconia electrode, Proc. of the 2nd International Symposium on SOFC, Grosz, F. Zegers, P., Singhal, S.C., Yamamoto, O. (editors), Athens, Greece (1991) 553-559.
- [12] Mohamedi-Boulenouar, F.Z., Guindet, J., Hammou, A., Influence of water on electrochemical oxidation of H₂ at the nickel-YSZ interface, Proc. of the 5th International Symposium on SOFC (SOFC-V) 97-40, Stimming, U., Singhal, S.C., Tagawa, H., Lehnert, W. (editors), Pennington, NJ (1997) 441-450.

- [13] Kek, D., Mogensen, M., Pejovnik, S., A study of metal (Ni, Pt, Au)/yttria-stabilised zirconia interface in hydrogen atmosphere at elevated temperature, *J. Electrochem. Soc.* 148 (2001) A878-A886.
- [14] Bieberle, A., The electrochemistry of solid oxide fuel cell anodes: Experiments, modelling, and simulations, Ph.D. Thesis, Swiss Federal Institute of Technology, Switzerland (2000).
- [15] Bieberle, A., Meier, L.P., Gauckler, L.J., The electrochemistry of Ni pattern anodes used as solid oxide fuel cell model electrodes, *J. Electrochem. Soc.* 148 (2001) A646-A656.
- [16] Mizusaki, J., Tagawa, H., Saito, T., Kamitani, K., Yamamura, T., Hirano, K., Ehara, S., Takagi, T., Hikita, T., Ippommatsu, M., Nakagawa, S., Hashimoto, K., Preparation of nickel pattern electrodes on YSZ and their electrochemical properties in H₂-H₂O atmospheres, *J. Electrochem. Soc.* 141 (1994) 2129-2134.
- [17] de Boer, A., SOFC Anode. Hydrogen oxidation at porous nickel and nickel/yttria-stabilised zirconia cermet electrodes, Ph.D. Thesis, University of Twente, The Netherlands (1998).
- [18] Mogensen, M., Vels Jensen, K., Jørgensen, M.J., Primdahl, S., Progress in understanding SOFC electrodes, in press, *Solid State Ionics* 150 (2002) 123-129.
- [19] Hansen, B.M., FCL electrochemical cont. program V. 3.1-3.2 (1992).
- [20] Boukamp, B. A., Equivalent Circuit Users Manual, University of Twente, The Netherlands (1989).
- [21] Howe, J. M., Interfaces in Materials, John Wiley and Sons, Inc. (1997).
- [22] Heffelfinger, J.R., Bench, M.W., Carter, C.B., On the faceting of ceramic surfaces, *Surface Science* 343 (1995) L1161-L1166.
- [23] Heffelfinger, J.R., Carter, C.B., Mechanisms of surface faceting and coarsening, *Surface Science* 389 (1997) 188-200.
- [24] De Souza, R.A., Kilner, J.A., Oxygen transport in La_{1-x}Sr_xMn_{1-y}Co_yO_{3±δ}, *Solid State Ionics* 126 (1999) 153-161.
- [25] Giese, D.R., Lamelas, F.J., Owen, H.A., Plass, R., Gajdardziska-Josifovska, M., Atomic force microscopy and scanning electron microscopy study of MgO (110) surface faceting, *Surface Science* 457 (2000) 326-336.
- [26] Chan, C.T., Che, J.G., Leung, T.C., First principles studies of overlayer induced faceting, *Progress in Surface Science* 59 (1998) 1-11.
- [27] Ghetta, V., Chatain, D., Morphologies adopted by Al₂O₃ single-crystal surfaces in contact with Cu droplets, *J. American Ceramic Society* 85 (2002) 961-964.
- [28] Yasunaga, H., Natori, A., Electromigration on semiconductor surfaces, *Surface Science Reports* 15 (1992) 205-280.
- [29] Aaberg, R.J., Tunold, R., Mogensen, M., Berg, R.W., Ødegård, R., Morphological changes at the interface of the nickel-yttria stabilized zirconia point electrode, *J. Electrochem. Soc.* 145 (1998) 2244-2252.

- [30] Badwal, S.P.S., Hughes, A.E., Modification of cell characteristics by segregated impurities, Proc. of the 2nd. International Symposium on SOFC, Grosz, F. Zegers, P., Singhal, S.C., Yamamoto, O. (editors), Athens, Greece (1991) 445-454.
- [31] Hughes, A.E., Interfacial phenomena in Y_2O_3 - ZrO_2 -based ceramics: A surface science perspective, Science of Ceramic Interfaces II (1994) 183-238.
- [32] Wagner, C.D., Davis, L.E., Zeller, M.V., Taylor, J.A., Raymond, R.H., Gale, L.H., Empirical atomic sensitivity factors for quantitative-analysis by electron spectroscopy for chemical analysis, Surf. Interface Anal. 3 (1981) 211-225.
- [33] Hughes, A.E., Badwal, S.P.S., Impurity and yttrium segregation in yttria tetragonal zirconia, Solid State Ionics 46 (1991) 265-274.
- [34] Hughes, A.E., Segregation in single crystal fully stabilized yttria-zirconia, J. American Ceramic Society 78 (1995) 369-378.
- [35] Chorkendorff, I., (2002).
- [36] Koch, S., Contact resistance of ceramic materials used for solid oxide fuel cell applications, Ph.D. Thesis, Risø National Laboratory, Denmark (2002).
- [37] Howe, J.M., Bonding, structure and properties of metal/ceramic bonding: Part 1: Chemical bonding, chemical reaction and interfacial structure. Part 2: Interface fracture behaviour and property measurement, International Materials Review 38 (1993) 233-255.
- [38] Ranløv, J., Bilde-Sørensen, J.B., Solid state wetting of YSZ with NiO and dewetting of Ni-metal on YSZ, ASOF-Risø-8 BC-54 (1991) 1-4.
- [39] Newman, J., Resistance for flow of current to a disk, J. Electrochem. Soc. 113 (1966) 501-503.
- [40] Holm, R., Electric contacts, Chapter 1, Springer-Verlag, Berlin (1967).
- [41] Gibson, I.R., Dransfield, G.P., Irvine, J.T.S., Influence of yttria concentration upon electrical properties and susceptibility to ageing of yttria-stabilised zirconias, J. European Ceramic Society 18 (1998) 661-667.
- [42] Badwal, S.P.S., Zirconia-based solid electrolytes: microstructure, stability and ionic conductivity, Solid State Ionics 52 (1992) 23-32.
- [43] Appel, C.C., Bonanos, N., Horsewell, A., Linderoth, S., Ageing behaviour of zirconia stabilised by yttria and manganese oxide, J. Mat. Sci. 36 (2000) 4493-4501.
- [44] Mogensen, M., Primdahl, S., Juhl, M., Revealing the mechanisms of SOFC electrodes using a combination of AC and DC methods, Proc. 5th International symposium on SOFC (SOFC-V) 97-40 (1997) 385-393.
- [45] Elbek, B., Elektromagnetisme, Niels Bohr Instituttet, Copenhagen (1995).
- [46] Badwal, S.P.S., Hughes, A.E., The effects of sintering atmospheres on impurity phase formation and grain boundary resistivity in Y_2O_3 -fully stabilised ZrO_2 , J. European Ceramic Society 10 (1992) 115-122.

- [47] Badwal, S.P.S., Grain boundary resistivity in zirconia-based materials: effect of sintering temperatures and impurities, *Solid State Ionics* 76 (1995) 67-80.
- [48] de Ridder, M., van Welzenis, R.G., Brongersma, H.H., Wulff, S., Chu, W.-F., Weppner, W., Discovery of the rate limiting step in solid oxide fuel cells by LEIS, *Nuclear Instruments and Methods in Physics Research B* 190 (2002) 732-735.
- [49] Mogensen, M., Electrode kinetics of SOFC anodes and cathodes, 14th Risø International Symposium on Materials Science: High temperature electrochemical behaviour of fast ion and mixed conductors, Poulsen, F.W., Bentzen, J.J., Jacobsen, T., Skou, E. Østergård, M.J.L. (editors) (1993) 117-135.
- [50] Aaberg, R. J., Morphology and electrochemistry of metal/yttria stabilised zirconia electrodes in H₂-H₂O atmospheres, Ph.D. Thesis, NTNU, Norway (1998).
- [51] Mogensen, M., Primdahl, S., Vels Jensen, K., Jørgensen, M.J., Bagger, C., Foreign phases and SOFC electrode kinetics, Proc. of the 7th International Symposium on SOFC (SOFC-VII), June 3-8, Tsukuba, Japan, Yokokawa, H., Singhal, S.C., (editors), Pennington, NJ, (2001) 521-528.

List of publications

1. Studies of the Ni-YSZ interface in solid oxide fuel cell anodes, K. Vels Jensen, S. Primdahl, M. Mogensen, Mass and charge transport in inorganic materials: fundamentals to devices, P. Vincenzini, V. Buscagli (editors), Techna, Faenza. (2000) 1443-1449.
2. Microstructural and chemical changes at the Ni-YSZ interface, K. Vels Jensen, S. Primdahl, I. Chorkendorff and M. Mogensen. Solid State Ionics, Vol. 144, 3-4 (2001) 197-209.
3. Effect of impurities on structural and electrochemical properties of the Ni-YSZ interface, K. Vels Jensen, R. Wallenberg, I. Chorkendorff and M. Mogensen. Submitted
4. Foreign phases and SOFC electrode kinetics, M. Mogensen, S. Primdahl, K. Vels Jensen, M. J. Jørgensen, C. Bagger, Proc. of the 7th International Symposium on SOFC (SOFC-VII), June 3-8, Tsukuba, Japan, Yokokawa, H., Singhal, S.C., (editors), Pennington, NJ, (2001) 521-528.
5. Progress in understanding SOFC electrodes, M. Mogensen, K. Vels Jensen, M.J. Jørgensen, S. Primdahl, Solid State Ionics (2002), in press.

Appendices A-E

Appendix A

List of experiments

A comprehensive amount of work has been done to achieve the results presented in this thesis. A large number of samples have been examined amongst which some has later been discarded, either due to equipment errors or irreproducible results. A short description of all the performed experiments is given.

KV01

The first experiment included three YSZ pellets, two with anodic and cathodic overvoltages respectively, and one at OCV. The surfaces of the pellets were raw from the mechanical working. The nickel wires were used without any preparation. The experiment lasted three days. No extra load was applied, just the weight (ca. 6 g) of the alumina rod were present. The following SEM examinations of the specimens did not show any contact areas at all. The YSZ surfaces were very rough and showed clear markings of mechanical working. The series resistance (R_s) was much higher than in the following experiments, implying a poor contact between the nickel and the YSZ.

KV02

Three polished YSZ pellets and electropolished nickel wires were used to produce well defined contact areas. An extra load of 76 g was applied, resulting in a total load of 82 g corresponding to a pressure of >10 MPa. The experiment lasted 6 days. Impedance measurements were performed continuously for the specimen at OCV. No measurements were done on the other specimens while they were polarised.

The pellet left at OCV and the one with anodic polarisation showed contact areas with a hill and valley structure. A piece of YSZ was missing from the pellets and a fracture was seen. The pellet with cathodic overvoltage was discarded due to a very large fracture.

KV03

Three of the samples (anodic, cathodic and OCV) were treated as in the previous experiment (KV02). The experiment lasted for 8 days (the polarisation for 5 days). Continuous impedance measurements were performed on all samples. All measurements (anodically polarised specimen) with the EG&G were discarded due to instability of the current during chronoamperometry.

All the samples except the one with cathodic polarisation were reproducing earlier results; the structures of the specimen with cathodic polarisation were different and interesting (but not reproducible).

The polished surfaces were examined in AFM before the experiment and showed irregularities in the order of 5-10 nm, mainly scratches due to the polishing. Particles lying on the surface were also seen. All parts and specimens were cleaned in an ultra-sound bath and with pressurised air before mounting.

KV04

This was the first pellet, which was not connected and where no impedance measurements were done. A tiny area showed the hill and valley structures, a fracture occupied the rest of the contact area.

KV05

A full series of samples (OCV, not-connected, anodic and cathodic polarisation) were analysed. All parts were carefully cleaned before mounting. The experiment lasted for 11 days,

polarisation for 6 days. Continuous impedance measurements were performed on the polarised samples.

The OCV and anodically polarised sample were reproducing earlier results; all samples showed the same type of hill and valley structures.

KV07

One sample was cathodically polarised to find out if the structures from KV05 were reproducible, one sample had an extra load of 15 g (~1/5 of the normal load) only, to see if this would affect the morphology. The other two samples were annealed to eliminate the possibility that recrystallisation of an amorphous surface layer (from polishing) was responsible for the structure formation. One of them was a normal pellet (left at OCV); the other was a single crystal of 10YSZ (not-connected). The experiment lasted for 12 days, polarisation for 7 days.

The experiment showed reproducibility of the structures of the cathodic polarised sample and similar structures on the rest of the specimens.

KV08

To examine the effect of heat and pressure only, none of the samples were connected, so no impedance data result from this experiment. Two samples had an extra load of 76 g and they both showed the usual structures. The third sample did not have the extra load, just the alumina rod (ca. 6 g) were pushing the nickel wire toward the YSZ surface. Hill-and-valley structures and a fracture were found.

The design of the fourth sample was different from the others. The nickel wire (0.078 g) was bent into the usual tip but with a coil attached. The coil was wrapped around the upper part of the pellet and kept the wire positioned on the surface. This configuration is considered a no-load set-up. No fracture and consequently no bonding were observed but a hill-and-valley structure was found.

KV09

Three of the electrodes here were made of the 0.25 mm 99.99% nickel wire. All samples were loaded with extra 76 g. This experiment only lasted 12 hours due to breakdown of the furnace. However it was seen that distinct structures had developed on the anodically polarised sample (92a). No other contact areas were found.

KV11

This was an experiment where continuous impedance measurements were performed on 111a and 112a (both impure nickel electrodes) and an occasional OCV-measurement was done on 113a (pure nickel electrode). The electrode on 114n was made of platinum. No structures were seen on 114n but bonding had occurred. Pt-drops were seen on the pellet in one end of the elliptical fracture.

111a and 112a were alternately anodically polarised and left at OCV to verify the decrease/increase in R_p upon polarising/changing back to OCV. When one was polarised, the other was at OCV. Measurements were done approximately every 15 minutes. The experiment lasted for 7 days.

Contact areas with hill and valley structures were found on 111a, 112a and 113o.

KV12

The pure nickel wire was used on all samples. Two samples were measured at OCV; the two others were not connected. The experiment lasted for 8 days.

Contact areas were found on 121, 122 and 124 and on all the nickel wires.

KV13

This experiment was performed to test if the thin, pure nickel wire/YSZ contact was good enough. The nickel wires were not put in the alumina support but directly in the alumina rod with the load on top. The experiment lasted for 7 days.

Contact areas were found on 132n, 133n and 134n on pellets and all contacts on the wires were found.

KV15

A YSZ pellet was annealed for 3 weeks at 1200°C in air. Changes in the surface morphology were obvious.

KV16

A pre-annealed and an anodically polarised sample both with impure nickel wires, a sample with a pure nickel wire and a single crystal with an impure wire were examined.

Only the first 120 hours of data for the anodically polarised sample are usable and microstructurally this sample is discarded. It was decided to polarise the pre-annealed sample instead. The experiment lasted for 13 days, polarisation lasted for 4 days.

The pre-annealed sample showed a normal sized contact area. No fracture was found. Hill and valley structure and rim ridge were well developed. The single crystal showed well developed structures and a small fracture.

KV18

Four samples all with a pure nickel wire as electrode were polarised successively, three days each. Three anodically polarised samples and one cathodically polarised sample were produced. The whole experiment lasted 18 days.

Two of the samples had a very high R_s . When the samples were dismantled the 183a pellet and nickel wire stuck together and the sample showed deviating electrochemical properties. Contact areas were found on all pellets. 182a did not show a real contact area, merely some scattered points of contact.

KV19

During the experiment there was some problems with the potentiostat. Furthermore, the set-up was probably affected by movements related to the change of measuring cables from one sample to another. The series resistance for 193a makes a sudden jump. All samples were discarded.

KV20

Four samples with thin, pure nickel wires were measured. The R_p -values were very unstable. The chronoamperometry curves were useless due to a too low measuring resistor. Contact areas were found on three samples, one was very different from two others. As the measurements were not performed satisfactory, these samples were disregarded.

Finally it was decided that the thin wires were too difficult to use.

KV21

A thicker pure nickel wire was used for the following experiments. Two samples were anodically polarised. The other two samples were meant for TOF-SIMS measurements but did not turn well out. The polarised samples showed consistent results. Contact areas were found on them both. For 213 a large fracture was found.

KV22

Four samples were anodically polarised. Three of them showed results and microstructures consistent with KV21-results. The fourth showed structures more like those found on non-polarised samples and the impedance measurements were in agreement with this. The experiment lasted for 17 days. Polarisations lasted 2-3 days.

KV23

Two samples for TOF-SIMS were prepared, one with a pure electrode and one with an impure electrode. The last sample had a not-connected, pure nickel wire. Contact areas were found on all samples, all were typical for their type. The experiment lasted for 10 days.

KV24

Three samples with pure nickel electrodes were cathodically polarised. All contact areas were found. The reproducibility of the microstructures and impedance spectroscopy was satisfactory. The experiment lasted for 10 days. Polarisation lasted for 2-4 days.

Appendix B

The user interface of EasyPlot.

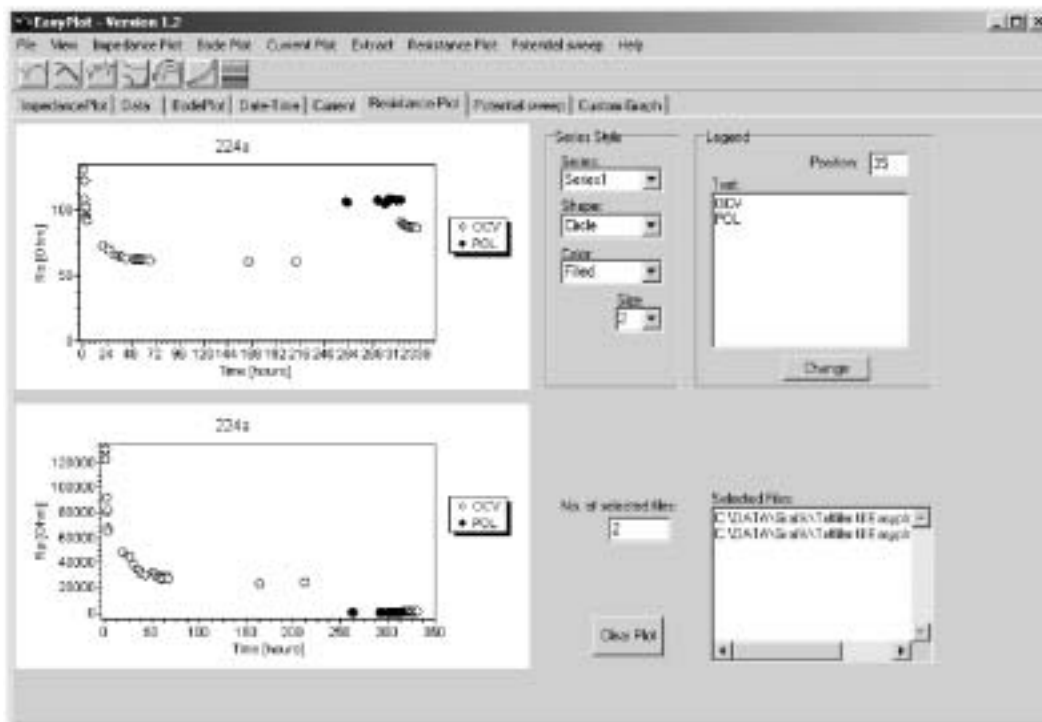


Fig. B.1. The feature for plotting both R_s and R_e vs. time.

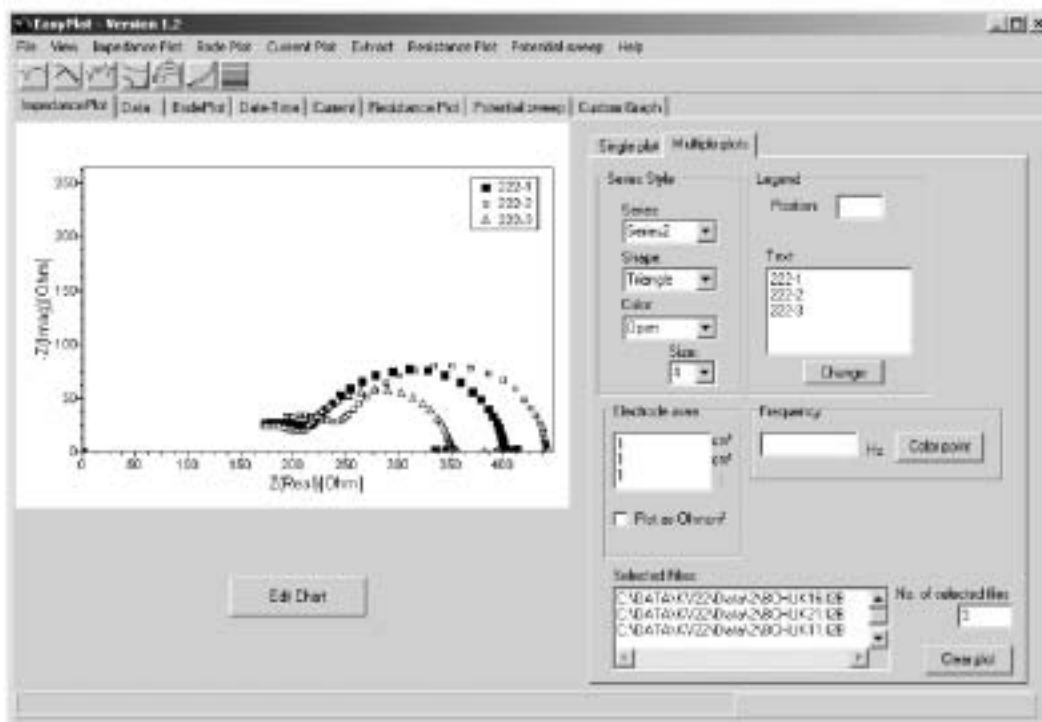


Fig. B.2. The feature for plotting multiple impedance plots.

Appendix C

Additional impedance plots

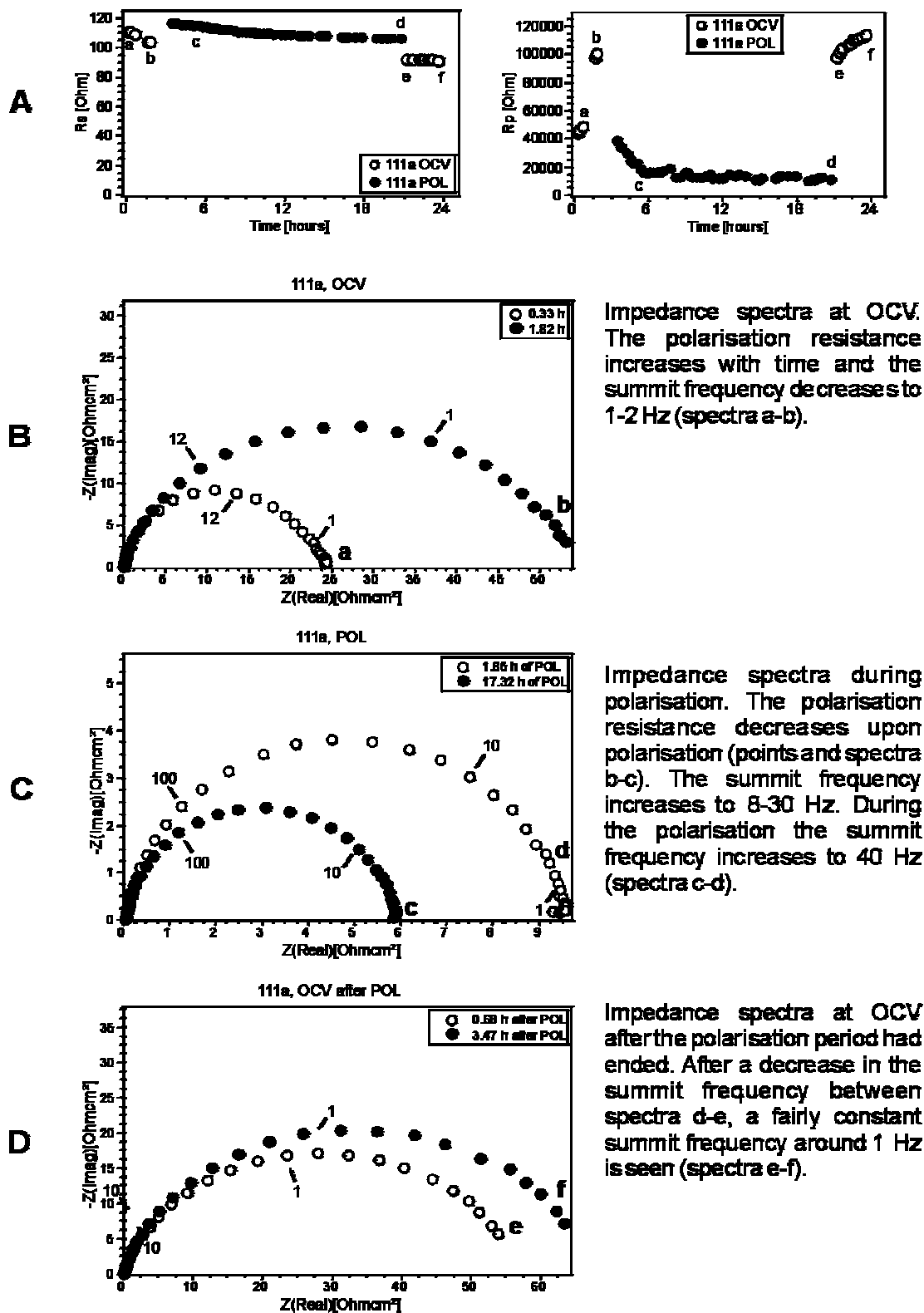


Fig. C.1. Impedance spectra for the sample 111a (impure electrode). A) R_s and R_p graphs. The letters a-f show the positions of the impedance spectra in B), C) and D).

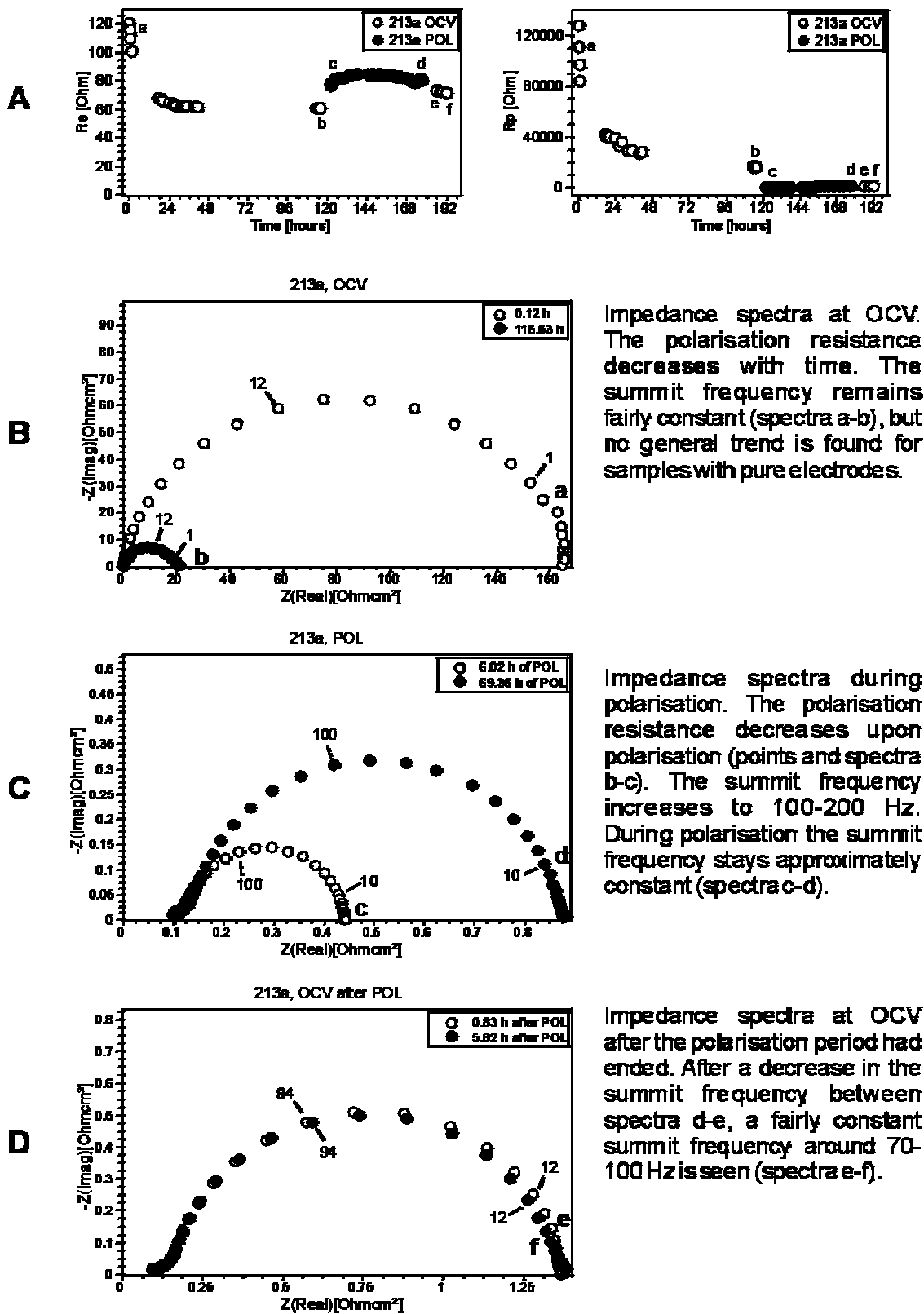


Fig. C.2 Impedance spectra for the sample 213a (pure electrode). A) R_e and R_p graphs. The letters a-f show the positions of the impedance spectra in B), C) and D).

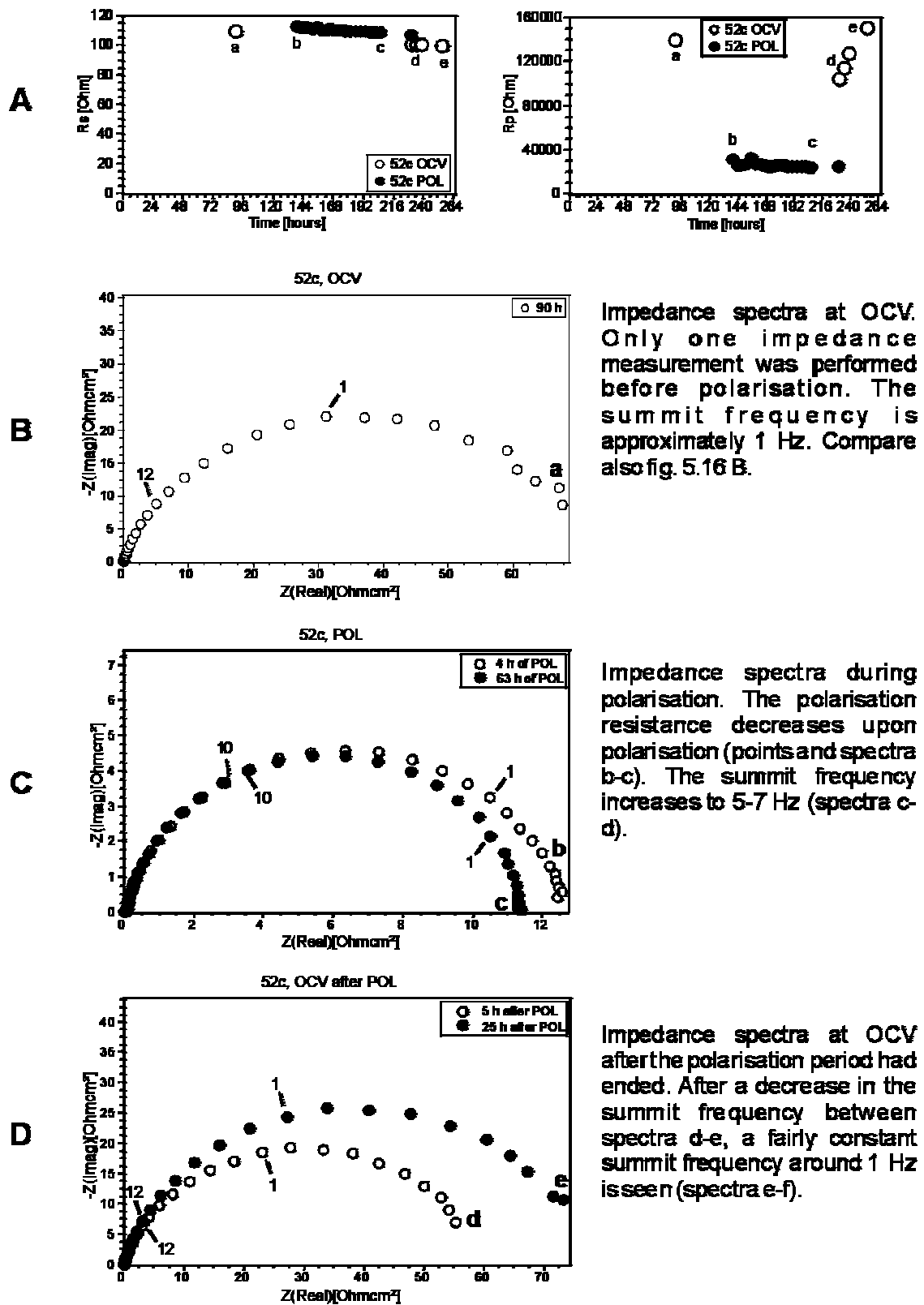


Fig. C.3. Impedance spectra for the sample 52c (impure electrode). A) R_e and R_p graphs. The points a-f show the positions of the impedance spectra in B), C) and D).

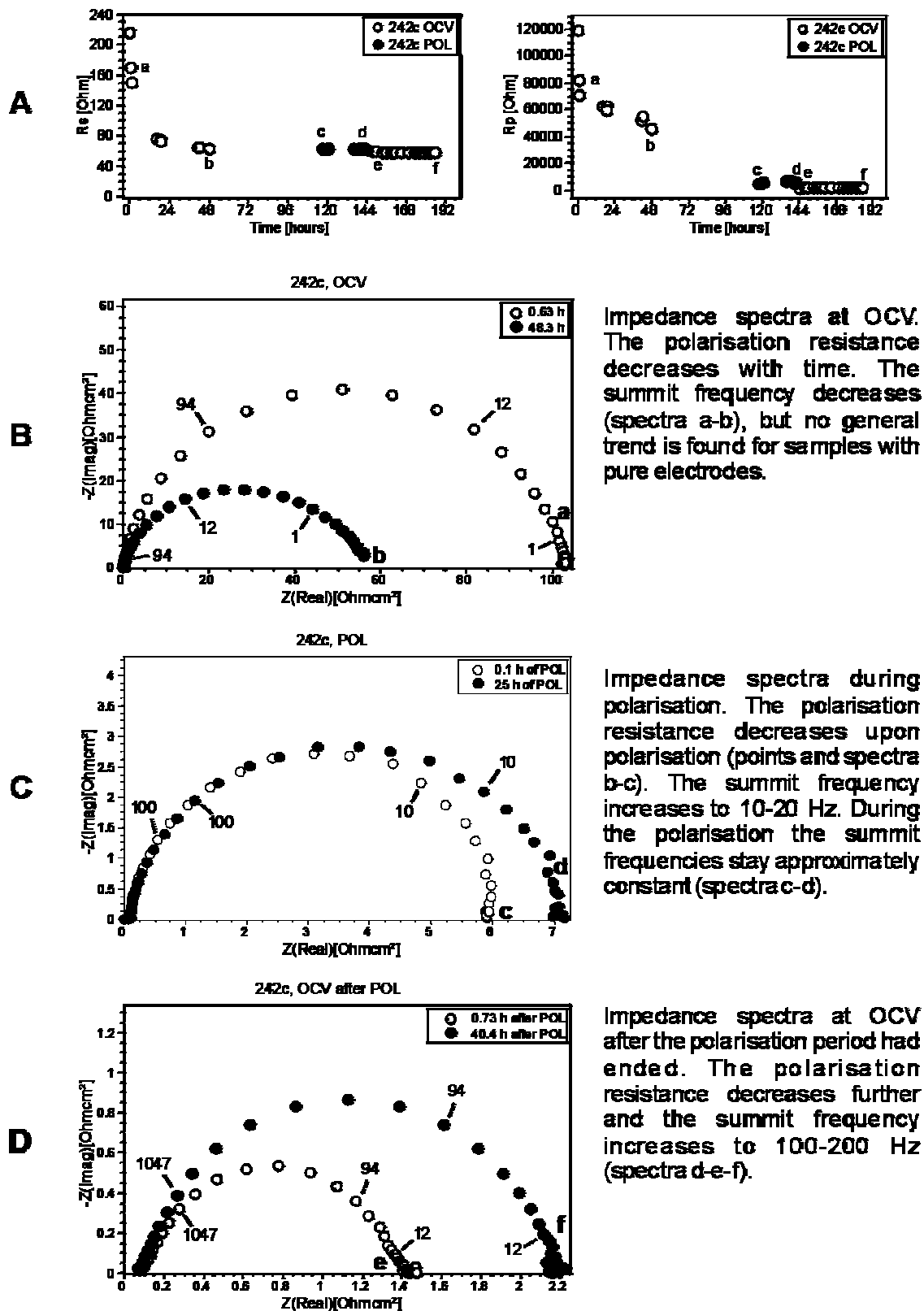


Fig. C.4. Impedance spectra for the sample 241c (pure electrode). A) R_e and R_p graphs. The points a-f show the positions of the impedance spectra in B), C) and D).

Appendix D Potential sweep curves

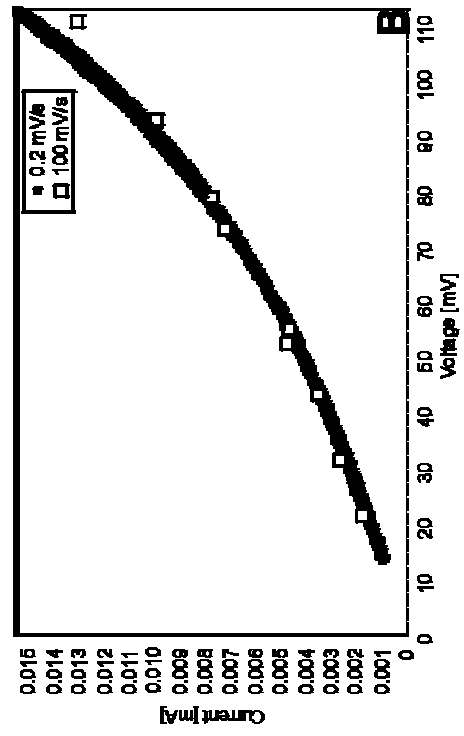
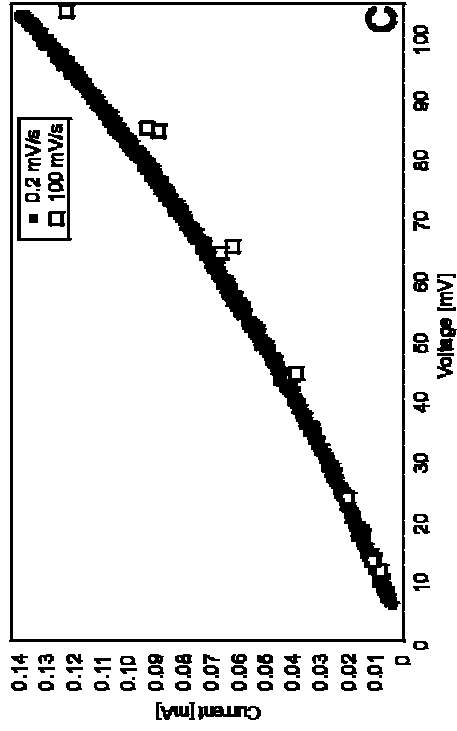
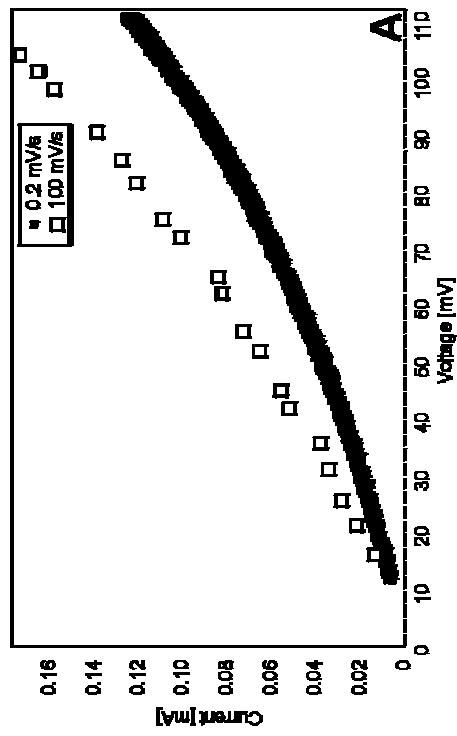


Fig. D.1. Potential sweeps for anodically polarised samples 213a (A), 212a (B) and 221 (C).

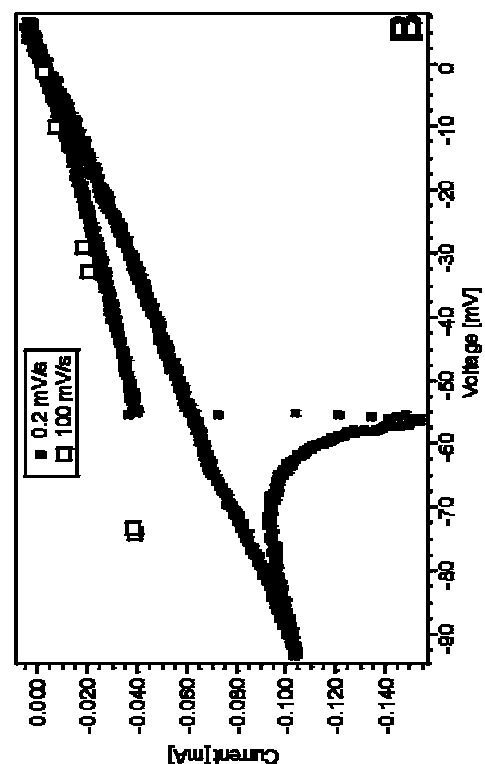
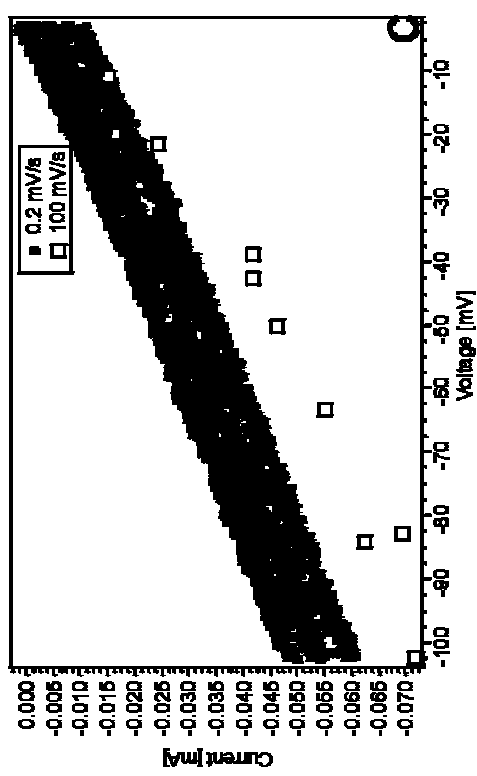
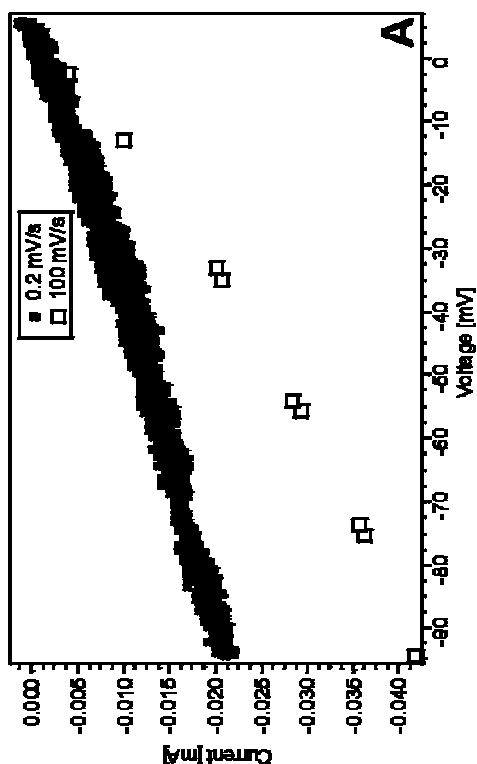


Fig. D.2. Potential sweep for the cathodically polarised samples 241c (A), 242c (B) and 243c (C).

Appendix E

Publications

- 1. Studies of the Ni-YSZ interface in solid oxide fuel cell anodesPage 103**
K. Vels Jensen, S. Primdahl, M. Mogensen
- 2. Microstructural and chemical changes at the Ni/YSZ interface.....Page 110**
K. Vels Jensen, S. Primdahl, I. Chorkendorff, M. Mogensen
- 3. Effect of impurities on structural and electrochemical properties
of the Ni-YSZ interfacePage 127**
K. Vels Jensen, R. Wallenberg, I. Chorkendorff and M. Mogensen
- 4. Foreign phases and SOFC electrode kinetics.....Page 146**
M. Mogensen, S. Primdahl, K. Vels Jensen, M.J. Jørgensen, C. Bagger
- 5. Progress in understanding SOFC electrodesPage 155**
M. Mogensen, K. Vels Jensen, M.J. Jørgensen, S. Primdahl

Article 1

”Studies of the Ni-YSZ interface in solid oxide fuel cell anodes”

K. Vels Jensen, S. Primdahl, M. Mogensen

published in:

**Mass and charge transport in inorganic materials:
fundamentals to devices,**

P. Vincenzini, V. Buscagli (editors), Techna, Faenza. (2000) 1443-1449

Article 2

”Microstructural and chemical changes at the Ni/YSZ interface”

K. Vels Jensen, S. Primdahl, I. Chorkendorff and M. Mogensen

published in:

Solid State Ionics 144 (2001) 197-209

Article 3

**”Effect of impurities on structural and electrochemical properties
of the Ni-YSZ interface”**

K. Vels Jensen, R. Wallenberg, I. Chorkendorff and M. Mogensen

submitted to

Solid State Ionics, June 2002

Article 4

”Foreign phases and SOFC electrode kinetics”

M. Mogensen, S. Primdahl, K. Vels Jensen, M.J. Jørgensen, C. Bagger

published in:

Proc. of the 7th International Symposium on SOFC, June 3-8, Tsukuba, Japan, Yokokawa, H., Singhal, S.C., (editors), Pennington, NJ, (2001) 521-528

Article 5

”Progress in understanding SOFC electrodes”

M. Mogensen, K. Vels Jensen, M.J. Jørgensen, S. Primdahl

published in:

Solid State Ionics 150 (2002) 123-129.

Title and authors

The Ni-YSZ interface: Structure, composition and electrochemical properties at 1000°C

Karin Vels Jensen

ISBN	ISSN
87-550-3042-4, 87-550-3043-2(Internet)	0106-2840
Department or group	Date
Materials Research Department	04-06-2002
Groups own reg. number(s)	Project/contract No(s)

Pages	Tables	Illustrations	References
111	26	75	51

Abstract (max. 2000 characters)

Geometrically simple Ni/yttria-stabilised zirconia (YSZ) interfaces were examined to gain information on the structural and chemical changes occurring during experiments at 1000°C in an atmosphere of 97% H₂/3% H₂O. Electrochemical impedance spectroscopy at open circuit voltage (OCV) and at anodic and cathodic polarisations (100 mV) was performed. Nickel wires with different impurity content (99.8% Ni and 99.995% Ni) were used to examine the impact of impurities on the polarisation resistance and contact area morphology. Extensive structural changes were found to occur in the contact area with the impure nickel wire, and a ridge of impurities was built along the rim of the contact area. Impurity particles in the interfacial region were also observed. No differences were found between polarised and non-polarised samples. With pure nickel wires, however, the microstructures depended on the polarisation/non-polarisation conditions. At non-polarised conditions a hill and valley type structure was found. Anodic polarisation produced an up to 1 µm thick interface layer. At cathodic polarisation both a granulated structure and a hill and valley structure were found. Small impurity ridges were surrounding the contact areas on non-polarised and cathodically polarised samples. TOF-SIMS and XPS analyses showed the presence of impurities in both contact areas. The impedance spectroscopy revealed different trends of the polarisation resistance with time depending on the impurity content of the nickel. At OCV the samples with impure nickel electrodes showed an initial increase toward a high constant polarisation resistance, whereas the samples with pure nickel electrodes showed a considerable decrease to a low constant polarisation resistance with time. For both types of nickel the polarisation resistance dropped upon polarisation. The ASR for the samples with pure electrodes were approximately 10 times lower than for samples with impure electrodes. This was mainly ascribed to the impurity content and distribution, both in the three phase boundary zone and as a more or less continuous film covering the interfacial region.

Descriptors INIS/EDB

SOFC, YSZ, Nickel, Interface, Impurities, Impedance spectroscopy, Polarisation resistance, TOF-SIMS, Hill and valley structure

Available on request from Information Service Department, Risø National Laboratory,
(Afdelingen for Informationsservice, Forskningscenter Risø), P.O.Box 49, DK-4000 Roskilde, Denmark.
Telephone (+45) 4677 4004, Telefax (+45) 4677 4013